



universität
wien

DISSERTATION

Titel der Dissertation

Anisotropic atomic motion in FePt thin films

Verfasser

Mag. Friedrich Gröstlinger

angestrebter akademischer Grad

Doktor der Naturwissenschaften (Dr. rer. nat.)

Wien, April 2012

Studienkennzahl lt. Studienblatt: A 091 411

Dissertationsgebiet lt. Studienblatt: Physik

Betreuer: Ao. Univ. Prof. Dr. Bogdan Sepiol

Abstract

Die Dynamik von Atomen zeigt die thermodynamischen und mechanischen Eigenschaften von Festkörpern in ihrer fundamentalen Form. Die Festkörperphysik teilt die Bewegung der Atome in Schwingungen und absolute Bewegung im Raum ein. In dieser Arbeit wird ein komplettes Bild anisotroper Dynamik in epitaktischen FePt-Nanoschichten präsentiert. Diese spezielle Phase ist ein vielversprechender Kandidat für Festplatten der nächsten Generation.

Untersuchungen anisotroper Eigenschaften in der L1₀-Struktur sind generell selten, da die tetragonale Symmetrie sogar in Einkristallen unterschiedliche Orientierungen zulässt. Werden jedoch Schichten epitaktisch auf geeigneten Substraten aufgewachsen, so lassen sich Proben mit einer definierten Gitterorientierung erzeugen. Als Methode wählen wir kernresonante Röntgenstreuung, die uns bestimmte Schichten von Atomen über die Verwendung spezieller Isotope markieren lässt.

Der erste Teil behandelt Fe-Selbstdiffusion in epitaktischen L1₀-geordneten FePt-Nanoschichten. Ein isotopisches Vielschichtensystem aus [⁵⁷FePt/^{nat}FePt]₁₀ auf MgO-(110) wurde bei Temperaturen von 653 K bis 743 K ausgeheizt. Mittels kernresonanter Streuung kann hier die Abnahme der isotopischen Überstruktur durch Diffusion beobachtet werden. Die gut definierte Orientierung der Struktur in den Schichten erlaubt es die Anisotropie zu bestimmen. Die Diffusion entlang der *a*-Richtung der L1₀-Struktur ist um zwei Größenordnungen schneller als in der *c*-Richtung. Dieser gravierende Unterschied stimmt qualitativ mit dem erwarteten Diffusionsmechanismus überein, ist aber bedeutend höher als in vergleichbaren Strukturen wie TiAl. Ein wichtiger Punkt war dabei der Vergleich der Auswertung mit kinematischer bzw. dynamischer Streutheorie, in der auch die Hyperfein-Wechselwirkung berücksichtigt wird.

Im zweiten Teil wird die Anisotropie der Zustandsdichte der Gitterschwingungen mit inelastischer kernresonanter Streuung untersucht. Die Orientierung der Struktur in den Proben entspricht jener im ersten Teil, wobei hier die gesamte Probe mit ⁵⁷Fe angereichert ist. Die gemessene Anisotropie stimmt gut mit ab-initio Berechnungen überein und lässt auf anisotrope elastische Eigenschaften schließen. Durch die Oberflächensensitivität der Methode und die Tiefenabhängigkeit der Zustandsdichte aus den ab-initio Rechnungen können wir die letzte Schicht vor der Oberfläche als Pt identifizieren.

Die anisotropen dynamischen Eigenschaften der L1₀-Struktur am Beispiel FePt wurden ausführlich untersucht. Die ungewöhnlich starke Anisotropie der Diffusionskonstante und der Zustandsdichte regt zu weiteren Untersuchungen sowohl bei vergleichbaren Temperaturen als auch in ähnlichen Systemen an.

Abstract

Atomic dynamics contain the thermodynamic and mechanical properties of solids in its fundamental form. Solid state physics separates atomic motion into atomic vibrations (phonons) and spatial net motion (diffusion). In this thesis a complete picture of anisotropic atomic motion in epitaxial L1₀-ordered FePt thin films is presented. This specific phase is one of the most promising candidates for next-generation hard drives for its large magnetocrystalline uniaxial anisotropy and excellent thermal stability.

In general anisotropic studies in the L1₀-structure are scarce due to its tetragonal nature permitting different orientations even in single crystals. However, by growing films epitaxially on suitable substrates, samples with a consistent lattice orientation can be produced. The method of choice is nuclear resonant scattering for its ability to see only the atoms marked by using a special isotope.

The first and major part deals with Fe self-diffusion in epitaxial L1₀-ordered FePt thin films. Isotopic multilayers of [⁵⁷FePt/^{nat}FePt]₁₀ on MgO(110) were annealed at temperatures between 653 K and 743 K. Nuclear resonant scattering reveals the decay of the isotopic superstructure due to diffusion. The well-defined orientation of the lattice in FePt-thin films allows to resolve the strong anisotropy of diffusion in the tetragonal structure. The diffusion along the *a*-axes of the L1₀ structure is up to two orders of magnitude faster than along the *c*-axis, which is in line with the commonly assumed diffusion mechanism in this structure, but the anisotropy is much higher than in comparable structures such as TiAl. An essential subtopic of this study was to compare the classical kinematical evaluation to an analysis employing the full dynamical scattering theory including the hyperfine parameters of the nuclear resonances.

In the second part the anisotropy of the phonon density of states is investigated by inelastic nuclear resonant scattering. The orientation of the structure in the sample is the same as above, in this case however the whole sample is enriched with ⁵⁷Fe. The measured anisotropy is in good agreement with ab-initio calculations, and suggests significant anisotropy in the elastic properties of FePt in particular, but L1₀-phases in general. Additionally depth-dependent ab-initio calculations show significant differences in the density of states. The strong surface sensitivity of the grazing incidence geometry of the experiment enabled us to identify the top atomic layer made up of Pt.

Overall the anisotropic dynamic properties of the L1₀-structure, on FePt as the model system, are thoroughly investigated. The strong anisotropy in the diffusion constant and the phonon density of state encourages further studies at comparable thermal energies as well as on different systems.

CONTENTS

I. Diffusion	1
1. Introduction	2
1.1. FePt	2
1.2. Diffusion in solids	5
1.3. Mössbauer effect	6
2. Theory	9
2.1. Diffusion in thin films	9
2.1.1. Solution by convolution via Fourier transform	9
2.1.2. Solution via finite differences	13
2.1.3. Diffusion in anisotropic media	15
2.2. Structure function	18
2.3. Kinematical approximation	19
2.4. Mössbauer effect	23
2.4.1. Electrostatic interaction	23
2.4.2. Magnetic interaction	24
2.4.3. Mössbauer line shape	25
2.5. The dynamical scattering theory	27
2.5.1. Propagation equation	28
2.5.2. Scattering amplitude	32
3. Experiment	35
3.1. Samples	35
3.1.1. General	35
3.1.2. Sample preparation	36
3.1.3. Rutherford backscattering	37

3.1.4.	X-ray diffraction	37
3.1.5.	Conversion electron Mössbauer spectroscopy	39
3.1.6.	Transmission electron microscopy	43
3.2.	Nuclear resonant experiment	44
3.2.1.	Thermal treatment	44
3.2.2.	Electronic reflectivity	45
3.2.3.	Nuclear reflectivity	46
4.	Results	51
4.1.	Reflectivity fits	51
4.2.	Diffusion coefficients	61
4.3.	Activation energy	64
5.	Discussion	66
5.1.	Effective formation energy	66
5.2.	Energetics	68
5.3.	Anisotropy	69
5.4.	Conclusion	72
II.	Atomic vibrations	73
6.	Introduction	74
6.1.	Phonons	74
6.2.	Nuclear inelastic resonant absorption	75
7.	Theory	77
7.1.	Nuclear inelastic scattering theory	77
7.2.	Phonon density from experiment	79
7.3.	Anisotropic density of states	81
8.	Experiment	82
8.1.	Samples	82
8.2.	Nuclear resonant experiment	83
9.	Results	86
9.1.	Phonon density of states	86
9.2.	Ab-initio calculations	88
9.3.	Surface modes	88
10.	Conclusion	90

A. Nuclear resonant scattering	91
A.1. Lippmann-Schwinger equation and Born approximation	91
A.2. Algebraic structure of dynamical scattering	92
A.3. Matrix exponential	96
B. Code examples	98
B.1. Symmetry considerations	98
B.2. Convolution via Fourier transform	100
B.3. Simplex minimization	100
B.4. Clebsch-Gordan coefficients	103
B.5. Nuclear resonant reflectivity	104
Acknowledgements	110
Bibliography	112

Part I.

Diffusion

INTRODUCTION

1.1. FePt

In our information society stable high density data storage is of great importance. Various materials are being investigated as storage media for such devices. Up to now the digital information is stored in domains with a magnetizations parallel to the surface. For this technique, however, the physical limit for spontaneous magnetization flips is reached. Two promising approaches for next generation storage devices have been identified:

Perpendicular data recording Magnetization perpendicular to the film surface permits a drastic decrease of the domain size for magnetic domains that are thermally stable [Yan et al., 2006; Suess et al., 2007].

Patterned media of monodisperse nanoparticles Decoupling of the magnetic interaction by spatially separated domains is another way to decrease the size of stable magnetic domains [Sun et al., 2000; Takahashi et al., 2003; Terris and Thomson, 2005].

In both cases FePt is one of the most promising candidates, because of the large magnetocrystalline uniaxial anisotropy ($\sim 7 \text{ J cm}^{-3}$) of the $L1_0$ phase in general [Staunton et al., 2004], and the thermal stability of this material in particular [Weller et al., 2000].

Although experimentally achieving only about $\rho \sim 1.5 \text{ Pb m}^{-2}$, where 1 b is one bit of digital information, i.e. 0 or 1, for a combination of thermally assisted writing on

patterned media, Stipe et al. [2010] considers storage densities of $\rho \sim 150 \text{ Pb m}^{-2} \sim 15 \text{ Tb cm}^{-2}$ theoretically possible for high-anisotropy materials such as FePt, corresponding to a bit area of $A \sim \rho^{-1} \sim 6.5 \text{ nm}^2 \text{ b}^{-1}$ and thus a bit length of approximately $a \sim A^{1/2} \sim 2.6 \text{ nm b}^{-1}$, possibly enabling 3 orders of magnitude higher storage density than today's hard drives with a maximum capacity of 3 TB (1 B = 8 b).

As early as the classical greek philosophy, humanity understood "Everything is in motion" (Heraklitus, Plato) as a fundamental property of nature. Through atomic dynamics the thermodynamic and mechanical properties can be observed in its fundamental form. Solid state physics separates atomic motion into atomic vibrations (phonons) and spatial net motion (diffusion). In this thesis a complete picture of anisotropic atomic motion in epitaxial L1₀-ordered FePt thin films is presented.

Information about atomic motion in thin films is crucial for their synthesis and stability. This calls for a detailed investigation of the fundamental mechanism of diffusion at temperatures as close as possible to typical operating temperatures of such storage devices.

The tetragonal L1₀ phase of FePt exists over a wide compositional range from 0.45 to 0.65 atomic fraction of Fe and remains ordered up to 1553 K (Fig. 1.1). The FePt phase diagram from the phase diagram collection of Massalski [1986], shown in Fig. 1.1, originates from Kubaschewski [1982]. The phase diagram shows a number of similarities to the FeNi and FePd systems. The solidification areas appear to be rather narrow, the center is made up of an continuous solid solution fcc phase ($\gamma\text{Fe, Pt}$), spanning the whole composition range, and confined within it we find three superstructures, namely L1₂ (Fe₃Pt), L1₀ (FePt) and L1₂ (FePt₃). By cooling down on the iron-rich side, passing the melting point of Fe at 1811 K, the melt stabilises in bcc as its first solid structure (δFe). As is well known from pure iron from 1667 K down fcc becomes the ground state of the solid, followed again by an bcc structure (αFe) with the widest of the transition areas, differing from the higher temperature bcc in its magnetic structure. This phase also incorporates the magnetic ordering transition marked by the dashed line indicating the Curie temperature of 1043 K. Additionally, alloys with atomic fraction between 0.22 and 0.35 of Pt show almost no thermal expansion [Sumiyama et al., 1979], which is referred to as the Invar effect. Furthermore martensitic transformations from fcc austenite to bcc martensite have been observed in alloys near the Fe₃Pt composition [Dunne and Wayman, 1973a,b], drawing attention as a shape-memory material. Our

interest is focused on the range of approximately 0.35 to 0.55 atomic fraction of Pt of the $L1_0$ -FePt phase bearing the large uniaxial magnetic anisotropy interesting for novel high density magnetic recording media.

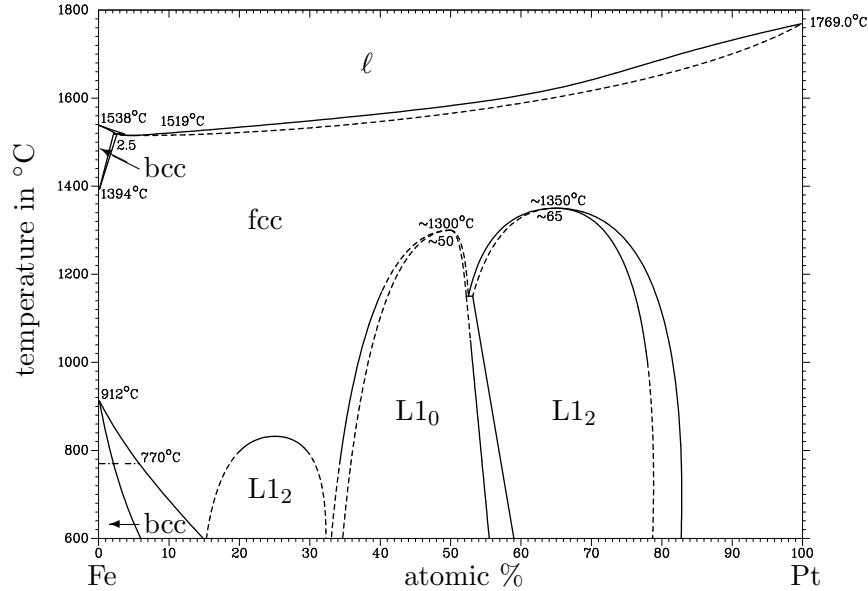


Figure 1.1.: Binary phase diagram of FePt. On the iron-rich side on cooling down the first stable state is a bcc followed by a intermediate large span of fcc solid solution and again the bcc structure as the ground state. With increasing Pt content there exist 3 superstructure phases derived from the fcc solid solution, namely $L1_2$ (Fe_3Pt), $L1_0$ ($FePt$) and $L1_2$ ($FePt_3$). The tetragonal $L1_0$ exhibits the large uniaxial magnetic anisotropy interesting for novel high density magnetic recording media.

A recent study of flash-lamp annealed FePt films of a thickness of 20 nm found the highest magnetic coercivity of $8.3 \times 10^5 \text{ A m}^{-1}$ for $Fe_{53}Pt_{47}$, a composition very close to the here investigated samples [Brombacher et al., 2012]. Although the overall magnetization is isotropic the coercivity measurements suggest the formation of a polycrystalline solid with large crystallites of high magnetic anisotropy. This method could prove viable as a tool to magnetize nano-particles with high magnetic stability.

Stable perpendicular magnetization was recently also observed for FePt surface alloys on Pt (997) substrates [Honolka et al., 2009]. The maximum magnetic anisotropy was achieved at an Fe concentration between 0.5 and 0.6. Although this could render to be

a viable alternative to FePt films for data storage devices, it confirms FePt close to stoichiometry as a material with astounding magnetic properties.

1.2. Diffusion in solids

The standard method for determining macroscopic diffusion coefficients in solids is the tracer technique [Gróh and von Hevesy, 1921; Philibert, 1991; Mehrer, 2007]. Here a radioactive or otherwise detectable, e.g. via fluorescence, element is introduced into the investigated solid. For self-diffusion the tracer is preferably an isotope of the investigated chemical element or at least of similar chemical properties. Thermal treatments at different temperatures set the diffusion rate of the tracer in the sample. Subsequently the diffusive spread of the tracer (in most cases 1-dimensional) is measured throughout the solid and compared to the solution of the diffusion equation. Here the resolution of the concentration measurement is the limiting factor, as it involves either cutting the sample into sections, which additionally makes this method destructive, or limiting the detection of the isotropic nuclear decay of the tracer to a small angular sector reducing the number of events, thus increasing the relative standard deviation of the experiment.

To make this method applicable for slower diffusivities (e.g. at lower temperatures) one would need to resolve smaller length scales in the sample. X-ray diffraction comes to mind if the resolution of the smallest structures in solids is necessary as the wavelength of the photons is even smaller than the typical atomic distance. Thus this method is capable of resolving superstructures down to a few lattice constants. Although it would be possible to extract the full information from scattering on a single interface, multilayers are used to amplify the essential parts of the scattering experiment by superposition, thus increasing the contrast of the experiment. So analogous to Bragg scattering the layered superstructure generates intensity maxima at rather low angles corresponding to the large superstructure period in the film. Depending on the x-ray energy the positions can be close to the total reflection angle. Additionally for an approximately periodic structure a simple expression for the evaluation in terms of diffusion can be found in Eq. (2.43). This concept was first proven valid for interdiffusion in chemically inhomogeneous multilayers [DuMond and Youtz, 1940].

Note that for conventional electronic scattering the intensity maxima reflect the periodic variations in the electronic density. Then again this does not come without the

disadvantage of inherent concentration, or in other words density, dependent diffusion constants.

This may be acceptable for interdiffusion studies, but for pure self-diffusion studies chemical, and thus electronic, homogeneity is a major requirement. Therefore nuclear sensitive methods have to be introduced. Besides neutron reflectometry [Gupta et al., 2004] it is possible to utilize the well-known nuclear transition of 14.4 keV of the Mössbauer isotope ^{57}Fe for nuclear resonant scattering [Rüffer and Chumakov, 1996; Gupta et al., 2005; Rennhofer et al., 2006], requiring samples with a one-dimensional superstructure, preferably of a period just about one order of magnitude above the lattice constant. These features are best achieved by films with a changing isotope concentration over the individual layers. In addition a preferred orientation of the lattice can be chosen by a suitable substrate, thus enabling the measurement of diffusion in different directions and furthermore resolving its anisotropy.

Assuming the kinematical approximation for the scattering process one can derive a simple relation between the decay of the super-structure Bragg peak intensity of a multilayer and the diffusion constant [DuMond and Youtz, 1940]. In this thesis, however, the full dynamical scattering theory including non-periodic boundary conditions, the distinct hyperfine parameters and the time integration window of the detector is applied.

A new method referred to as x-ray photon correlation spectroscopy (XPCS) to measure even atomic diffusion for similarly small diffusion lengths was developed in our group recently [Leitner et al., 2009]. It should provide complementary data for comparison. State of the art synchrotron sources with a sufficiently large portion of coherent photons should even be able to illuminate the atomic jumps in thin film samples, which can preserve anisotropy macroscopically.

1.3. Mössbauer effect

The nuclear resonant transition mentioned above is the foundation for the Mössbauer spectroscopy, one of the most successful spectroscopy methods with a wide range of applications from physics, metallurgy, biophysics up to archaeology and geology. Especially the transition from the ground state to the first excited state in ^{57}Fe found wide application due to its very sharp resonance lines. Basically the Mössbauer effect describes resonant absorption and subsequent recoil-free emission of a photon by an

atomic nucleus. In the particle representation the vanishing recoil can be explained by a lack of phonon states within the typical recoil energy scope. The momentum transfer, however, is non zero and hence temperature dependent. The main ideas of this section are taken from Wegener [1965].

For an intuitive access to the main features of this effect I introduce a ground $|\psi_g\rangle \propto e^{-iE_g t}$ and an excited state $|\psi_e\rangle \propto e^{-i(E_e - i\Gamma/2)t}$ of a nucleus. The temporal evolution of the emitted electric field (photon) is expected to be similar to the one of the nuclear density ρ at its deexcitation

$$E(t) \propto \rho(t) = \langle \psi_g | \psi_e \rangle \propto e^{-i\omega_0 t} e^{-\Gamma t/2}, \quad (1.1)$$

with the resonance at $\omega_0 \equiv E_e - E_g$. The first exponential of the electric field describes the temporal periodicity, whereas the second one holds the decay of the field amplitude in time. A simple Fourier transform \mathcal{F} yields

$$F(\omega) = \mathcal{F}E(t) \propto \frac{\Gamma/2 - i(\omega - \omega_0)}{(\omega - \omega_0)^2 + (\Gamma/2)^2} \quad (1.2)$$

and for the intensity the typical Lorentz shape of the resonance line in the energy domain

$$I(\omega) \propto |F(\omega)|^2 \propto \frac{1}{(\omega - \omega_0)^2 + (\Gamma/2)^2}. \quad (1.3)$$

The probability to find a nucleus still excited at a time t is then given by

$$p_e(t) \propto \langle \psi_e | \psi_e \rangle = |\psi_e|^2 \propto e^{-\Gamma t}, \quad (1.4)$$

which identifies $\tau \equiv 1/\Gamma$ as the mean life time of the excited state $|\psi_e\rangle$. For ^{57}Fe the natural life time of the first excited state is $\tau = 141.11$ ns corresponding to a natural line width of $\hbar\Gamma = 4.66$ neV. For a transition energy of 14.4125 keV [Röhlsberger, 2004] this equates to a extremely low relative line width in the order of 10^{-13} . From this fact alone one can see the magnificence of this method able to resolve the smallest perturbations of an atomic nucleus. Experimental data of standard Mössbauer experiments (transmission or CEMS) shows twice the spectral width due to the distribution of source and sample ~ 10 neV, e.g., see Fig. 3.3. Nevertheless the energy splittings that can be resolved in real samples can be scanned by tuning the resonance energy by just moving the photon source.

Of course the standard source for x-rays with a suitable energy for the transition of ^{57}Fe has to be an already excited ^{57}Fe nucleus, due to the very narrow bandwidth shown in Fig. 1.2. The Co isotope ^{57}Co with a half-life of $T_{1/2} = 271.8$ d decays by electron-capture into a higher excited state of ^{57}Fe , further proceeding into the required excited state by a probability of 0.88, whereas the rest decays directly to the ground state. This final excited nucleus decays into the ground state by emitting a photon (0.10) or a conversion electron (0.90). While the majority of the experiments detect the transmitted photons, thin film samples are usually investigated by collecting the reflected conversion electrons (CEMS) with a penetration depth of roughly 100 nm.

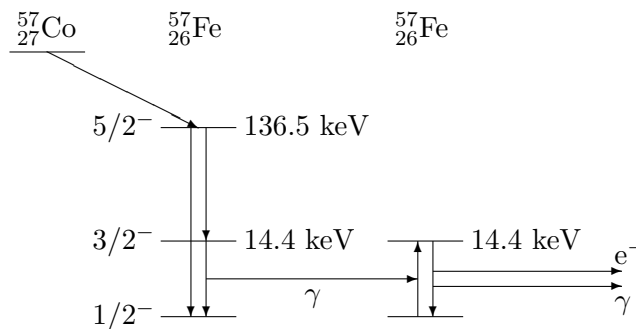


Figure 1.2.: Standard source: ^{57}Co isotope with a half-life of 271.8 d decays via electron-capture to a highly excited state. Further de-excitation leads to the desired first excited state of 14.4 keV. Excited nuclei decay into the ground state by emitting a photon γ or a conversion electron e^- . The source energy is tuned by moving the source thus scanning the energy of absorption of perturbed nuclei in the sample.

Modern day synchrotron sources, however, can produce hard x-rays of high brilliance and intensity in the essential energy regime. State of the art monochromators allow to extract a relatively small energy bandwidth for nuclear sensitive methods. Although not narrow enough for energy-resolved experiments, the time resolution of such a source, given by the time between electron bunches, is predestined to expand the method from the energy into the time domain. On the one hand coherent scattering may give additional structural information about the investigated matter. On the other hand the nearly perfect polarization is also sensitive to the direction and polarization of source x-rays.

CHAPTER 2

THEORY

2.1. Diffusion in thin films

The outline of this section is the description of diffusion in an in-plane homogeneous but in depth isotopically varying, otherwise chemically homogeneous thin film. The appropriate theoretical framework for describing the temporal evolution of a sample with a concentration profile c is simply the one-dimensional diffusion equation with constant coefficients D

$$(\partial_t - D\partial_z^2) c(t, z) = 0. \quad (2.1)$$

Note that in contrast to diffusion in chemically inhomogeneous systems here the chemical composition is uniform everywhere, therefore no concentration dependence of D complicates the picture. Before the scattered intensity of the sample can be calculated, the diffusion equation has to be solved with suitable boundary conditions, which in our case is an initial concentration profile $c(0, z) = g(z)$ and Neumann type boundary conditions at the film surface $z = 0$ and the substrate interface $z = d$, in other words $\partial_z c(t, 0) = \partial_z c(t, d) = 0$.

2.1.1. Solution by convolution via Fourier transform

In the Fourier space the spatial derivative of the concentration function translates to a multiplication with iq . Thus assuming a sufficiently rapid decreasing concentration

function c we find for the diffusion equation

$$\begin{aligned} \partial_t (\mathcal{F}c)(t, q) &= \partial_t \int dz e^{-iqz} c(t, z) = \int dz e^{-iqz} \partial_t c(t, z) \\ &= \int dz e^{-iqz} D \partial_z^2 c(t, z) = D \int dz (\partial_z^2 e^{-iqz}) c(t, z) = -q^2 D \int dz e^{-iqz} c(t, z) \\ &= -q^2 D (\mathcal{F}c)(t, q). \end{aligned} \quad (2.2)$$

These equations hold because both the concentration and its derivative is vanishing far outside of the investigated region. Integration of this relation is

$$\begin{aligned} (\mathcal{F}c)(t, q) &= e^{-q^2 Dt} (\mathcal{F}c)(0, q) \\ &= e^{-q^2 Dt} (\mathcal{F}g)(q) \end{aligned} \quad (2.3)$$

and using $(\mathcal{F}c)(0, q) = (\mathcal{F}g)(q)$ with the initial concentration g reveals that the Fourier transform of the latter decreases exponentially with time t . On the other hand this exponential is a normal distribution over q and we know that the Fourier transform of a normal distribution with width σ_q is again a normal distribution with inverse width $\sigma_z = 1/\sigma_q = 2Dt$. Therefore the exponential can be represented by the Fourier transform of a normal distribution and further manipulation leads to

$$\begin{aligned} (\mathcal{F}c)(t, q) &= (\mathcal{F}f)(t, q) (\mathcal{F}g)(q) \\ &= (\mathcal{F}(f * g))(t, q), \end{aligned} \quad (2.4)$$

where the latter is the Fourier transform of a convolution of the initial concentration with the so called fundamental solution

$$f(t, z) = (4\pi Dt)^{-1/2} e^{-z^2/4Dt}. \quad (2.5)$$

A simple inverse Fourier transform yields the concentration in real space

$$c(t, z) = (f * g)(t, z) = \int d\xi f(t, z - \xi) g(\xi), \quad (2.6)$$

which in the end is the convolution of the initial composition g with the fundamental solution f in form of a normal distribution. So to say the width of the normal distribution increases with time t , therefore the initial composition variation is smeared

out. A detailed proof that this is a unique solution for the diffusion equation can be found in Fischer and Kaul [2007, p. 402].

The solution could therefore be calculated in the reciprocal domain, as the convolution reduces to a simple multiplication

$$c(t, z) = (f * g)(t, z) = \mathcal{F}^{-1}((\mathcal{F}f)(\mathcal{F}g))(t, q), \quad (2.7)$$

called the convolution theorem.

However, considering Neumann boundary conditions the presumptions for the concentration function may not be met. An intuitive way to have vanishing concentration flux on both ends of the film is to mirror the concentration profile on one and assume further periodic boundary conditions. In this case I utilize the periodicity of the concentration profile c by expanding it into a Fourier series with period X as

$$c(t, x) = \sum_n e^{-iq_n x} C_n(t), \quad C_n(t) = \frac{1}{X} \int_{x_0}^{x_0+X} dx e^{iq_n x} c(t, x) \quad (2.8)$$

with the time dependent Fourier coefficients $C_n(t)$, limited to an arbitrary interval $[x_0, x_0 + X)$, which we may choose to be the concentration profile of the sample mirrored at the interface to the surface. Inserting the latter into the diffusion equation of Eq. (2.1) we get

$$\sum_n e^{-iq_n x} \partial_t C_n(t) = D \sum_n e^{-iq_n x} q_n^2 C_n(t) \quad (2.9)$$

and further the actual time dependence of the Fourier coefficients

$$C_n(t) = e^{-q_n^2 D t} C_n(0). \quad (2.10)$$

The Fourier transform of this normal distribution can again be expressed as a Fourier transform of the fundamental solution. After rearranging and substituting $x + x' \rightarrow x$ as shown in the following few lines for a certain $q_n = q$

$$(\mathcal{F}c)(t, q) = \frac{1}{X} \int_{x_0}^{x_0+X} dx e^{iqx} c(t, x)$$

$$\begin{aligned}
&= \frac{1}{X} e^{-q^2 Dt} \int_{x_0}^{x_0+X} dx e^{iqx} c_0(x) \\
&= \frac{1}{X} \int_{-\infty}^{+\infty} dx' e^{iqx'} g(t, x') \int_{x_0}^{x_0+X} dx c_0(x) e^{iqx} \\
&= \frac{1}{X} \int_{-\infty}^{+\infty} dx' g(t, x') \int_{x_0}^{x_0+X} dx c_0(x) e^{iq(x+x')} \\
&= \frac{1}{X} \int_{-\infty}^{+\infty} dx' g(t, x') \int_{x_0}^{x_0+X} dx c_0(x-x') e^{iqx} \\
&= \frac{1}{X} \int_{x_0}^{x_0+X} dx e^{iqx} \int_{-\infty}^{+\infty} dx' g(t, x') c_0(x-x') \\
&= (\mathcal{F}(g * c_0))(t, q), \tag{2.11}
\end{aligned}$$

where I denoted $c_0(x) = c(0, x)$ and $g(t, x) \equiv e^{-x^2/4Dt}$, we arrive at a similar solution for the diffusion equation, except in this version the Fourier transform is to be taken only on a single period of the concentration function. Because of the efficiency of Fast Fourier transforms (FFT), solving this equation, employing the convolution theorem of Eq. (2.7), is significantly faster than computing the actual convolution.

For different orientations in various domains we get different fundamental solutions with their specific diffusion constants D_j . The diffusion equation has to hold for each individual domain, thus the solution is the sum of the individual convolutions. However for the fundamental solutions g_j and weights w_j

$$\begin{aligned}
c(t, z) &= \sum_j w_j \mathcal{F}^{-1} \mathcal{F}(f * g_j) = \mathcal{F}^{-1} \sum_j w_j \mathcal{F}(f * g_j) \\
&= \mathcal{F}^{-1} \mathcal{F} \sum_j w_j (f * g_j) = \mathcal{F}^{-1} \mathcal{F} \sum_j f * w_j g_j \\
&= \mathcal{F}^{-1} \mathcal{F} f * \sum_j w_j g_j = \mathcal{F}^{-1} \left((\mathcal{F} f) (\mathcal{F} \sum_j w_j g_j) \right) \tag{2.12}
\end{aligned}$$

is valid, therefore it is equivalent to do the convolution of the weighted sum of the individual fundamental solutions. The relevant code is presented in Sec. B.2.

2.1.2. Solution via finite differences

Alternatively the partial differential equation may be approximated by finite differences. This way one may also introduce a concentration dependence of the diffusion constant. For example the diffusion equation for a diffusion parameter with linear concentration dependence $D(c) = D_0 + D_1c$ is

$$\begin{aligned}\partial_t c(t, z) &= \partial_z (D(c) \partial_z c(t, z)) \\ &= \partial_z D(c) \partial_z c(t, z) + D(c) \partial_z^2 c(t, z) \\ &= D_1 (\partial_z c(t, z))^2 + (D_0 + D_1 c(t, z)) \partial_z^2 c(t, z).\end{aligned}\quad (2.13)$$

The finite central difference may be approximated by

$$\delta f_n = f_{n+1/2} - f_{n-1/2} \approx \frac{1}{2} (f_{n+1} - f_{n-1}) \quad (2.14)$$

and the second order central difference is

$$\delta^2 f_n = f_{n+1} - 2f_n + f_{n-1}. \quad (2.15)$$

Therefore, applying the forward difference in time

$$\Delta f^t = f^{t+1} - f^t, \quad (2.16)$$

we get for the diffusion equation in this numerical approximation

$$\frac{c_n^{t+1} - c_n^t}{\Delta t} = D_1 \left(\frac{c_{n+1}^t - c_{n-1}^t}{2\Delta z} \right)^2 + (D_0 + D_1 c_n^t) \left(\frac{c_{n+1}^t - 2c_n^t + c_{n-1}^t}{(\Delta z)^2} \right). \quad (2.17)$$

The Neumann boundary condition is met by mirroring the concentration at both the surface of the film and the interface to the substrate. If I denote the concentration right inside the film as c_1 then the concentration right outside is $c_0 = c_1$. For the concentration gradient and the curvature applies $\delta c_0 = -\delta c_1 = 0$ and $\delta^2 c_0 = \delta^2 c_1$, respectively.

This approximation is however unstable as we can see by employing von Neumann stability analysis. So if I expand the numerical error and assume exponential behaviour

over time as

$$\epsilon(z) = \sum_m A_m e^{ik_m z} = \sum_m e^{at} e^{ik_m z} \quad (2.18)$$

and neglect second order terms of the error I arrive at the inequality for the error amplification factor $G \equiv \epsilon_n^{t+1}/\epsilon_n^t$

$$|G| = \left| 1 + \frac{\Delta t}{(\Delta z)^2} \left(\frac{1}{2} D_1 \cos(k\Delta z) - 4D_0 \sin^2(k\Delta z) \right) \right| \leq 1. \quad (2.19)$$

This reveals that the error is growing in every case and it has to be tested if this deviation is affecting the result to a problematic extent. Therefore the discretization grid has to be chosen with care. It should be mentioned, that for non-linear equations like this one, even a positive result from this kind of stability analysis is indeed necessary, but not sufficient for a bounded solution. For diffusion constants with no concentration dependence $D_1 = 0$ the condition reduces to

$$\Delta t \leq \frac{(\Delta z)^2}{2D_0} \quad (2.20)$$

and is sufficient to guarantee a stable solution. On the other hand a more complex implicit finite difference equations with unconditional stability at least for constant diffusion coefficient exists, i.e. the Crank-Nicholson scheme [Crank and Nicholson, 1947; Press et al., 1992]

$$\frac{c_n^{t+1} - c_n^t}{\Delta t} = \frac{D}{2} \frac{(c_{n+1}^{t+1} - 2c_n^{t+1} + c_{n-1}^{t+1}) + (c_{n+1}^t - 2c_n^t + c_{n-1}^t)}{(\Delta z)^2}. \quad (2.21)$$

Another way would be to consider mainly Fick's first law

$$J(t, z) = -D(t, z) \partial_z c(t, z) \quad (2.22)$$

and therefore calculate the concentration fluxes between the discrete concentrations c_i for $i = 0, \dots, N$ as

$$J_n^t = -D \frac{c_n^t - c_{n-1}^t}{\Delta z}, \quad n = 1, \dots, N \quad (2.23)$$

and assume no flux out of the surface and into the substrate $J_0 = J_{N+1} = 0$. From the

flux difference

$$\Delta J_n^t = J_n^t - J_{n+1}^t, \quad n = 0, \dots, N \quad (2.24)$$

we can calculate the concentration of the next time step by

$$c_n^{t+1} = c_n^t + \Delta t \frac{\Delta J_n}{\Delta z}. \quad (2.25)$$

This seems a very natural picture because the new concentration has to be the old concentration and the net flux out of or into a small volume. The advantage of this approach is the intrinsic mass conservation by reducing the diffusion to concentration exchange between small volumes.

2.1.3. Diffusion in anisotropic media

What can we say about the relation of the crystal symmetries to the symmetries of the physical properties? The answer is Neumann's principle which can be quoted as follows:

The symmetry elements of any physical property of a crystal must include the symmetry elements of the point group of the crystal.

Incidentally this fundamental principle is named after the father of the mathematician who introduced the Neumann boundary condition mentioned above. Fick's law for anisotropic diffusion can be written as a matrix equation with the diffusivity matrix \mathbf{D}

$$\mathbf{J} = -\mathbf{D}\mathbf{C}, \quad (2.26)$$

where \mathbf{J} is the diffusion flux and $\mathbf{C} \equiv \nabla C$ is the concentration gradient. For this illustration I already assume the symmetries of an orthorhombic lattice for our diffusion matrix \mathbf{D} in a Cartesian coordinate system with the orthonormal basis $\{\mathbf{e}_1, \mathbf{e}_2, \mathbf{e}_3\}$ coinciding with the lattice vectors $\mathbf{a} = a\mathbf{e}_1$, $\mathbf{b} = b\mathbf{e}_2$ and $\mathbf{c} = c\mathbf{e}_3$ as

$$\mathbf{D} = \begin{bmatrix} D_1 & 0 & 0 \\ 0 & D_2 & 0 \\ 0 & 0 & D_3 \end{bmatrix}. \quad (2.27)$$

In a tetragonal structure the measurement of the diffusion flux in an arbitrary direction represented by a normalized vector $\mathbf{N} = [n_1 \ n_2 \ n_3]^T$ has to be invariant to rotations \mathbf{R}

$$\mathbf{R}(\alpha) = \begin{bmatrix} \cos \alpha & -\sin \alpha & 0 \\ \sin \alpha & \cos \alpha & 0 \\ 0 & 0 & 1 \end{bmatrix} \quad (2.28)$$

about $\alpha = \pi/2$ around the distinguished c -axis of L1₀ (Fig. 3.1(a)) denoted by \mathbf{c} or \mathbf{e}_3 parallel to it. Therefore the relations

$$\mathbf{N}^T \mathbf{D} \mathbf{C} = (\mathbf{R} \mathbf{N})^T \mathbf{D} (\mathbf{R} \mathbf{C}) = \mathbf{N}^T (\mathbf{R}^T \mathbf{D} \mathbf{R}) \mathbf{C} \quad (2.29)$$

must hold. Naturally it does not matter if the symmetry operation acts on the crystal or the measured quantities [Nye, 1957], meaning that for rotational symmetry it does not matter if we rotate the crystal or the experiment. Note that an isotopic concentration gradient introduced into the solid reduces the symmetry of the overall sample therefore it is considered part of the experiment and in the latter case also has to be rotated. The equations above are fulfilled only for $D_1 = D_2$ (see Sec. B.1). In fact in that case they hold for arbitrary angles, which demonstrates that physical properties may be of higher symmetry than the underlying crystal structure, but not the other way around.

In general it is sufficient to only test the symmetry operation on the tensor of the physical properties as it holds all the information of the material, i.e. the results of an investigation. Thus for a general symmetric diffusion matrix \mathbf{D} with the rotation matrix \mathbf{R} for rotation about $\pi/2$ around the \mathbf{e}_3 axis Neumann's principle requires

$$\mathbf{D} = \mathbf{R}^T \mathbf{D} \mathbf{R} \quad (2.30)$$

and directly provides us with the distinct form of the diffusivity matrix

$$\mathbf{D} = \begin{bmatrix} D_1 & 0 & 0 \\ 0 & D_1 & 0 \\ 0 & 0 & D_3 \end{bmatrix}. \quad (2.31)$$

For the problem at hand I want to calculate the diffusivity for a 45° rotated structure on substrate displayed in Fig. 2.1. For the diffusivity matrix \mathbf{D} to be diagonal I choose the coordinate system to coincide with the rotated crystal as stated above. The

concentration gradient ∇c is obviously in film growth direction, therefore perpendicular to the substrate surface shown as red arrow in mentioned figure. So far I may write

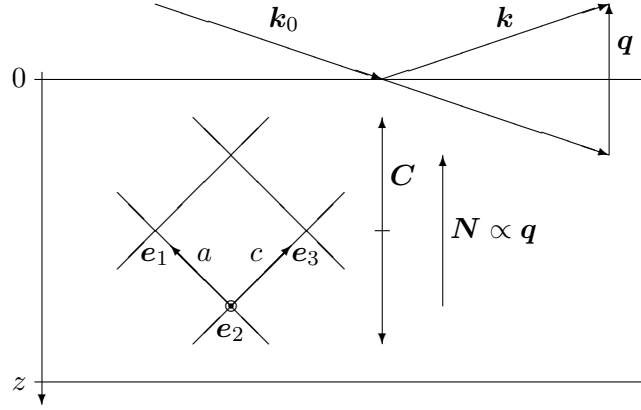


Figure 2.1.: Sketch of the orientation of the canted samples with respect to the scattering vector \mathbf{q} and the concentration gradient \mathbf{C} . For the derivation of the diffusion constants a Cartesian coordinate system denoted by $\{\mathbf{e}_i\}$ is used, which coincides with the lattice vectors.

$$\mathbf{D} = \begin{bmatrix} D_a & 0 & 0 \\ 0 & D_a & 0 \\ 0 & 0 & D_c \end{bmatrix}, \quad \nabla c = \frac{c'}{\sqrt{2}} \begin{bmatrix} 1 \\ 0 \\ 1 \end{bmatrix}. \quad (2.32)$$

The diffusion flux results therefore in

$$\mathbf{J} = -\mathbf{D}\nabla c = -\frac{c'}{\sqrt{2}} \begin{bmatrix} D_a \\ 0 \\ D_c \end{bmatrix}. \quad (2.33)$$

Employing nuclear resonant scattering at a scattering vector \mathbf{q} perpendicular to the sample surface, as I will explain in detail later, only the diffusion components parallel to the scattering vector under consideration can be measured. Thus the inner product

of the measurement direction vector denoted by \mathbf{N}

$$\mathbf{N} = \frac{1}{\sqrt{2}} \begin{bmatrix} 1 \\ 0 \\ 1 \end{bmatrix} \quad (2.34)$$

and the earlier expressed diffusion flux yields the actual diffusion constant $D_{[101]}$

$$D_{[101]} = -\frac{1}{c'} \mathbf{N} \cdot \mathbf{J} = \frac{1}{2}(D_a + D_c) \quad (2.35)$$

consisting of the fundamental tetragonal diffusion constants D_a and D_c . Of course the modulus of the concentration gradient c' has to be accounted for. Knowing the diffusion constant in c -direction from previous measurements in pure c -variant FePt films (Fig. 3.1(a)) I can deduce the diffusion constant in a -direction from this by

$$D_a = 2D_{[101]} - D_c. \quad (2.36)$$

Actually in our case D_c is roughly two orders of magnitude lower than D_a so I will neglect this term later, when fitting the kinematical approximation.

2.2. Structure function

The kinematical scattering theory employs the single scattering approximation, therefore the scattered intensity is proportional to the square of the Fourier transform of the atomic density ρ . The resulting function of the Fourier transform in the reciprocal space of the scattering vector $\mathbf{q} \equiv \mathbf{k} - \mathbf{k}_0$, where \mathbf{k}_0 and \mathbf{k} are the wave vectors of the incident and outgoing wave, respectively, is called structure function. This entity contains all information about the arrangement of the atoms. For a target with continuously distributed atoms (disordered sample) the structure function is

$$S(\mathbf{q}) = \int_V dx^3 e^{i\mathbf{q} \cdot \mathbf{x}} \rho(\mathbf{x}). \quad (2.37)$$

Employing some simple manipulations and partial integration with $\rho(\mathbf{x}) = 0$ for \mathbf{x} outside of V we get

$$\begin{aligned} S(\mathbf{q}) &= \frac{\mathbf{q}}{iq^2} \cdot \int_V dx^3 i\mathbf{q}e^{i\mathbf{q}\cdot\mathbf{x}}\rho(\mathbf{x}) = \frac{\mathbf{n}}{iq} \cdot \int_V dx^3 \nabla e^{i\mathbf{q}\cdot\mathbf{x}}\rho(\mathbf{x}) \\ &= -\frac{\mathbf{n}}{iq} \cdot \int_V dx^3 e^{i\mathbf{q}\cdot\mathbf{x}}\nabla\rho(\mathbf{x}), \end{aligned} \quad (2.38)$$

with the modulus of the scattering vector $q \equiv |\mathbf{q}|$ and a normalized scattering vector $\mathbf{n} = \mathbf{q}/q$. Therefore the largest contributions to the structure factor result from density gradients parallel to the scattering vector \mathbf{q} . Furthermore the $1/q$ dependence implies that the scattered field becomes comparable to the incident field at low angles of incidence θ , related to the scattering vector by $q = 2k_0 \sin \theta \approx 2k_0\theta$, where multiple scattering can no longer be neglected.

In our case of layers of different isotopic enrichment the concentration gradient with respect to the whole film clearly stands perpendicular to the film surface. For the scattering vector \mathbf{q} to be parallel to the latter the scattering geometry has to be simply the ordinary specular reflection.

Analogous to Bragg scattering a layered superstructure generates intensity maxima at rather low angles corresponding to the large superstructure period in the film. The Laue condition in combination with the definition of the reciprocal lattice $\mathbf{q} \cdot \mathbf{x} = 2\pi m$ for a scattering vector \mathbf{q} yields for the first order maximum $m = 1$ in the small angle approximation a scattering angle of $\theta \approx \pi\hbar c/E_0x$. For an x-ray energy of $E_0 = 14.4$ keV and a superstructure period of $x = 4$ nm I obtain $\theta \approx 11.2$ mrad, so the interesting part of the reflectivity is located close to the critical angle θ_c , below which there is total reflection. This angle can be estimated using Snell's law $\cos \theta_c \approx (1 - \delta) \cos \phi$ with $\phi = 0$ to about $\theta_c \approx \sqrt{2\delta} = 4.7$ mrad.

2.3. Kinematical approximation

The standard approach to find the effective diffusivity in a layered structure from a scattering experiment was developed by DuMond and Youtz [1940]. The kinematical scattering approximation is used to relate the decrease of the superstructure peak intensity to the diffusion parameter. The theoretical background is outlined in this

section.

For the Fourier series expansion of the concentration c with the time dependent Fourier component C_m and the corresponding momentum vector q_m we have

$$c(t, z) = \sum_m C_m(t) e^{iq_m z}. \quad (2.39)$$

The expansion is inserted into the diffusion equation (2.1) as

$$\sum_m e^{iq_m z} (\partial_t C_m(t) + q_m^2 D C_m(t)) = 0, \quad (2.40)$$

and one finds the exponential decay of the spatial Fourier coefficients as a function of time t similar to a continuous description employing the Fourier transform in Sec 2.1

$$C_m(t) = C_m(0) e^{-q_m^2 D t}. \quad (2.41)$$

Furthermore we know that the scattered intensity I of a density variation in the kinematical approximation is

$$\begin{aligned} I(t, q) &\propto |A(t, q)|^2 \propto \left| \int dz e^{iqz} c(t, z) \right|^2 \\ &= \left| \int dz e^{-iqz} \sum_m C_m(0) e^{-q_m^2 D t} e^{iq_m z} \right|^2 \\ &= \left| \sum_m C_m(0) e^{-q_m^2 D t} \int dz e^{-i(q-q_m)z} \right|^2 \\ &= \left| \sum_m C_m(0) e^{-q_m^2 D t} \delta(q - q_m) \right|^2 \\ &= \left| C_q(0) e^{-q^2 D t} \right|^2. \end{aligned} \quad (2.42)$$

Thus for a certain scattering vector the intensity is just $I(t, q) \propto |C_q(t)|^2$. The logarithmic relative intensity linearly decreases with annealing time t as

$$\ln \frac{I(t, q)}{I(0, q)} \propto \ln \frac{|C_q(t)|^2}{|C_q(0)|^2} = -2q^2 D t, \quad (2.43)$$

allowing for an easy access to the diffusion constant D .

Various aspects of this approach were recently criticized in connection with this type of experiment [Andreeva et al., 2008; Merkel et al., 2010]. In particular the kinematical approximation ceases to hold (i) in the vicinity of the critical angle and (ii) for nuclear resonant scattering. In particular the hyperfine parameters (e.g. the resonance line width, the magnetic field and its distribution) and mainly the limited detection window may influence the evolution of the superstructure intensity. The full dynamical treatment of the scattering is therefore necessary, considering all the hyperfine parameters and respective distributions as well as the detection time window.

Even in single crystals of a tetragonal structure one often finds domains with the 3 possible orientations of the distinguished axis. In that case, if I want to incorporate multiple domains with known fractions, the equations above have to be modified. Approximately equally distributed domains of concentrations c_i and sizes below the transversal coherence length may be weighted by their fraction w_i and summed over coherently as follows

$$I(t, q) \propto \left| \int dz e^{-iqz} \sum_i w_i c_i(t, z) \right|^2. \quad (2.44)$$

Inserting Eq. (2.39) I may proceed to

$$\begin{aligned} I(t, q) &= \left| \int dz e^{-iqz} \sum_i w_i \sum_m C_m(0) e^{iq_m z} e^{-q_m^2 D_i t} \right|^2 \\ &= \left| \sum_i w_i \sum_m C_m(0) e^{-q_m^2 D_i t} \int dz e^{-i(q-q_m)z} \right|^2 \\ &= \left| \sum_i w_i \sum_m C_m(0) e^{-q_m^2 D_i t} \delta(q - q_m) \right|^2 \\ &= |C_q(0)|^2 \left| \sum_i w_i e^{-q^2 D_i t} \right|^2. \end{aligned} \quad (2.45)$$

For a certain scattering vector q , typically the first Bragg peak, and the abundance normalization $\sum_i w_i = 1$ in an analogous manner to above I get for the logarithmic

intensity ratio

$$\begin{aligned} \ln \frac{I(t, q)}{I(0, q)} &= \ln \frac{|C_q(0)|^2 \left| \sum_i w_i e^{-q^2 D_i t} \right|^2}{|C_q(0)|^2 \sum_i w_i} \\ &= 2 \ln \sum_i w_i e^{-q^2 D_i t} \end{aligned} \quad (2.46)$$

If, however, the domains are large and thus the coherent fraction is small, I would arrive at slightly different expression

$$\begin{aligned} I(t, q) &= \sum_i w_i \left| \int dz e^{-iqz} c_i(t, z) \right|^2 \\ &= \sum_i w_i \left| \int dz e^{-iqz} \sum_m C_m(0) e^{iq_m z} e^{-q_m^2 D_i t} \right|^2 \\ &= \sum_i w_i \left| \sum_m C_m(0) e^{-q_m^2 D_i t} \int dz e^{-i(q-q_m)z} \right|^2 \\ &= \sum_i w_i \left| \sum_m C_m(0) e^{-q_m^2 D_i t} \delta(q - q_m) \right|^2 \\ &= \sum_i w_i \left| C_q(0) e^{-q^2 D_i t} \right|^2 \\ &= |C_q(0)|^2 \sum_i w_i e^{-2q^2 D_i t} . \end{aligned} \quad (2.47)$$

Again for the intensity ratios I would have

$$\begin{aligned} \ln \frac{I(t, q)}{I(0, q)} &= \ln \frac{|C_q(0)|^2 \sum_i w_i e^{-2q D_i t}}{|C_q(0)|^2 \sum_i w_i} \\ &= \ln \sum_i w_i e^{-2q^2 D_i t} . \end{aligned} \quad (2.48)$$

Unfortunately compared with Eq. (2.43) in this case there is no longer a strict linear dependence on t , so non-linear fitting algorithms, i.e. Levenberg-Marquardt, have to be applied to extract the diffusion constants D_i . However, if the orientation of the domains and their corresponding fractions are known, the effective diffusion in the measured direction can be deduced from this equation.

2.4. Mössbauer effect

2.4.1. Electrostatic interaction

An electrostatic potential $\Phi(\mathbf{x})$ interacts with the charge density of a nucleus $\rho(\mathbf{x})$, thus lifting the degeneracy of the eigenstates by modifying the energies. The interaction energy V of the electrostatic potentials of the surrounding atoms and the charge density of the nucleus is

$$V = \int dx^3 \rho(\mathbf{x})\Phi(\mathbf{x}). \quad (2.49)$$

Expanding the potential Φ around the equilibrium position \mathbf{x}_0 and defining the modulus of the position vector $x^2 \equiv |\mathbf{x}|^2 = \sum_i x_i^2$, the potential at its equilibrium position $\Phi_0 \equiv \Phi(\mathbf{x})|_{\mathbf{x}_0}$ and its derivatives $q_i \equiv \partial_i \Phi(\mathbf{x})|_{\mathbf{x}_0}$ and $q_{ij} \equiv \partial_{x_i} \partial_{x_j} \Phi(\mathbf{x})|_{\mathbf{x}_0}$ yield

$$\begin{aligned} V &= \Phi_0 \int dx^3 \rho(\mathbf{x}) + \sum_i q_i \int dx^3 \rho(\mathbf{x})x_i + \frac{1}{2} \sum_{i,j} \int dx^3 \rho(\mathbf{x})x_i x_j \\ &= \frac{1}{2} \sum_i q_{ii} \int dx^3 \rho x_i^2 \\ &= \frac{1}{6} \sum_i q_{ii} \int dx^3 \rho(\mathbf{x})x^2 + \frac{1}{2} \sum_i q_{ii} \int dx^3 \rho (x_i^2 - x^2/3), \end{aligned} \quad (2.50)$$

where the first term of the expansion is inconsequential and the second one vanishes due to symmetry against inversion. Furthermore for every symmetric matrix a diagonal representation q_{ii} exists. Omitting a rather long deduction involving the expansion of the nuclear charge density into the eigenstates of the nucleus, transforming into spherical coordinates and employing the Wigner-Eckart theorem, one arrives at the final form of the two terms as

$$\begin{aligned} V &\approx \frac{2\pi Z e^2}{3} |\psi(0)|^2 \langle x^2 \rangle + \frac{eQV_{33}}{4} \frac{3m^2 - j(j+1)}{3j^2 - j(j+1)} \\ &= V_I + V_Q, \end{aligned} \quad (2.51)$$

identified as the isomer shift V_I and the quadrupole splitting V_Q . A detailed discussion of the individual parameters is given below.

Isomer shift For the isomer shift the mean quadratic nuclear radius was defined as $\int dx^3 \rho x^2 \equiv Ze \langle x^2 \rangle$, including normalization to the nuclear charge $Ze = \int dx^3 \rho$. Additionally $-e|\psi(0)|^2$ is the charge density at the nucleus.

$$V_I = \frac{2\pi Ze^2}{3} |\psi(0)|^2 \langle x^2 \rangle \quad (2.52)$$

With these definitions in mind the main variable is the mean quadratic nuclear radius. For one, the cores form of the excited state differs from the one of the ground state. The interesting part, however, is the influence of changes in the surrounding chemical composition, thus the electronic structure, to the nucleus. The result is an overall shift of the nuclear resonance in the energy domain.

Quadrupole splitting The equation for the quadrupole splitting again is

$$V_Q = \frac{eQV_{33}}{4} \frac{3m^2 - j(j+1)}{3j^2 - j(j+1)}, \quad (2.53)$$

where V_{33} is identified as the electric field gradient at the nucleus without the portion resulting from the s -electrons. Q can be conceived as the quadrupole moment of the nucleus with $Q > 0$ and $Q < 0$ for the nuclear charge density extended in or perpendicular to the field gradient direction. For the ground state of the ^{57}Fe atom with $j_g = 1/2$ the quadrupole splitting vanishes. For the excited state with $j_e = 3/2$ on the contrary the degeneracy is partially lifted into two states with $V_Q = \pm eQV_{33}/4$ for $m = \pm 3/2, \pm 1/2$. Thus there are two possible transitions from the excited to the ground state, which results in two distinct resonance lines, in other words the nuclear resonance is splitted.

2.4.2. Magnetic interaction

The difference in the interaction energies of the magnetic moment of the nucleus with the magnetic field established by the surrounding electrons is

$$\begin{aligned} V_M &= -(\boldsymbol{\mu}_e \cdot \mathbf{H} - \boldsymbol{\mu}_g \cdot \mathbf{H}) \\ &= -\left(\frac{\mu_e m_e}{j_e} - \frac{\mu_g m_g}{j_g} \right) H \end{aligned} \quad (2.54)$$

with the nuclear magnetic moments μ_g and μ_e , the spin and spin projection quantum numbers j and m , respectively, and the magnetic field at the nucleus H . Magnetic dipole transition are constrained by $|m_e - m_g| \leq 1$. That leaves 6 possible transitions shown in Fig. 2.2 translating to a sextet of resonance lines.

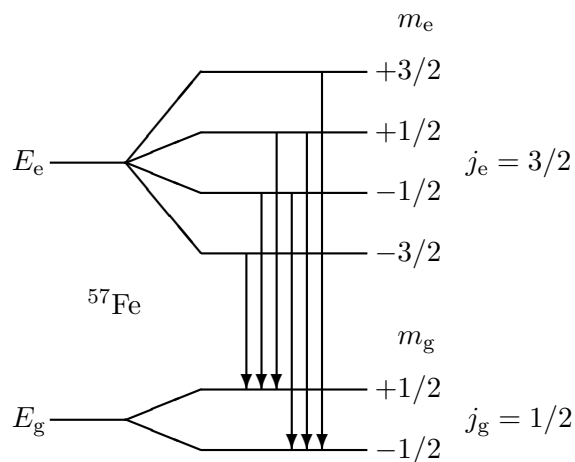


Figure 2.2.: Allowed transitions of the nuclear ground and first excited state separated by magnetic hyperfine interaction. The energy difference of the ground and excited state is about 10^{11} times larger than the resonance-line width.

2.4.3. Mössbauer line shape

For a consistent evaluation of the conversion electron Mössbauer spectra (CEMS) it was necessary to simultaneously fit the data of several samples. Otherwise the very small fraction of sites in some samples could not be included to yield a stable solution. The line shape was calculated employing an approximation outlined in Rancourt and Ping [1991], capable of incorporating arbitrary distribution of hyperfine fields with linear couplings to center shifts and quadrupole splittings. The approximation is valid if the quadrupole splitting is much smaller than the Zeeman splitting z , i.e. $e^2qQ/2 \ll g_e\mu_N H \equiv z$, with the quadrupole moment Q , the nuclear g -factor of the excited state g_e , the nuclear magnetic moment μ_N and the magnetic hyperfine field H .

The hyperfine field is assumed to consist of N normal distributions G

$$G(z_0, \sigma, z) = \frac{1}{\sqrt{2\pi}\sigma} e^{-(z-z_0)^2/2\sigma^2}, \quad (2.55)$$

with standard deviations σ_i , distribution centers δ_i and weights p_i

$$H(z) = \sum_{i=1}^N p_i G(z_{0i}, \sigma_i, z). \quad (2.56)$$

Assuming the transition lines to be of conventional Lorentzian shape

$$L(\omega, \gamma, \nu) = \frac{\gamma^2/4}{(\nu - \omega)^2 + \gamma^2/4} \quad (2.57)$$

then the elemental sextet of Mössbauer transition is given by

$$S(\nu) = \sum_{k=1}^6 h_k L(\omega_k, \gamma, \nu), \quad (2.58)$$

with the resonances at the energies ω_k as

$$\begin{aligned} \omega_1 &= \delta + \epsilon - (Z + 3)z/2 & \omega_4 &= \delta - \epsilon + (Z - 3)z/2 \\ \omega_2 &= \delta - \epsilon - (Z + 3)z/2 & \omega_5 &= \delta - \epsilon + (Z + 3)z/2 \\ \omega_3 &= \delta - \epsilon - (Z - 3)z/2 & \omega_6 &= \delta + \epsilon + (Z + 3)z/2. \end{aligned} \quad (2.59)$$

Therefore, the total intensity of the transitions of single site would be the convolution of the Lorentzian sextet S and the normal distributions of the magnetic hyperfine field H

$$I(\nu) = \int_{-\infty}^{\infty} dz H(z) S(\nu) \quad (2.60)$$

where ω_k of S depends on the Zeeman splitting z as we can see in Eq. (2.59). Inserting the individual distributions above results in a sum of $6N$ Voigt lines V

$$I(\nu) = \sum_{i=1}^N p_i \sum_{k=1}^6 h_k V(A_k + B_k z_{0i}, |B_k| \sigma_i, \gamma, \nu) \quad (2.61)$$

of the form

$$V(\delta, \sigma, \gamma, \nu) = \int_{-\infty}^{\infty} dz L(z, \gamma, \nu) G(\delta, \sigma, z). \quad (2.62)$$

In my case I assume only one magnetic field distribution per site so I have $p_1 = 1$ and $p_i = 0$ for all $i > 1$, thus Eq. (2.61) reduces to

$$I(\nu) = \sum_{k=1}^6 h_k V(A_k + B_k z_0, |B_k| \sigma, \gamma, \nu). \quad (2.63)$$

The formulas to calculate the individual coefficients A_k , B_k and δ_i from the isomer shift, the quadrupole and the Zeeman splitting can be found in Rancourt and Ping [1991] and are listed in Tab. 2.1. An analytical solution for the Voigt profile does not

Table 2.1.: Mössbauer parameters: number of resonance line k , spin quantum number of the ground m and excited state $m + M$, resonance line intensity h_k and corresponding parameters A_k and B_k

k	m	$m + M$	h_k	A_k	B_k
1	-1/2	-3/2	$3h_3$	$\delta_0 + \epsilon_0$	$\delta_1 + \epsilon_1 - (Z + 3)/2$
2	-1/2	-1/2	$f(\theta)h_3$	$\delta_0 - \epsilon_0$	$\delta_1 - \epsilon_1 - (Z + 1)/2$
3	-1/2	+1/2	h_3	$\delta_0 - \epsilon_0$	$\delta_1 - \epsilon_1 - (Z - 1)/2$
4	+1/2	-1/2	h_3	$\delta_0 - \epsilon_0$	$\delta_1 - \epsilon_1 + (Z - 1)/2$
5	+1/2	+1/2	$f(\theta)h_3$	$\delta_0 - \epsilon_0$	$\delta_1 - \epsilon_1 + (Z + 1)/2$
6	+1/2	+3/2	$3h_3$	$\delta_0 + \epsilon_0$	$\delta_1 + \epsilon_1 + (Z + 3)/2$

exist, but it can be expressed using the real part of the complex error function, also known as the Faddeeva function w by

$$V(\delta, \sigma, \gamma, \nu) = \frac{\Re(w((\nu - \delta + i\gamma)/\sqrt{2}\sigma))}{\sqrt{2\pi}\sigma} \quad (2.64)$$

which is commonly implemented in a sufficiently good approximation in numerical mathematics packages.

2.5. The dynamical scattering theory

Contrary to the kinematical scattering approximation, which only considers one scattering event per photon, in the dynamical scattering theory all orders of multiple scattering are inherently accounted for. The foundation of the dynamical scattering theory is owed to Darwin [1914a,b]; Ewald [1916a,b, 1917]; von Laue [1960] reviewed

in Batterman and Cole [1964]. The basic nuclear quantum theory of x-ray optics was developed in Blume and Kistner [1968]; Hannon and Trammell [1968] and generalized to dynamical scattering theory in Hannon and Trammell [1969]. It was further extended in Hannon et al. [1985a,b] for grazing-incidence antireflection films used as extremely narrow bandpass filters. These films would then remove the non-resonant electronic response in the reflection channel to allow for pure nuclear coherent X-ray scattering. The main difference with respect to conventional dynamical scattering theory is the heavy influence of polarization intermixing, present when the degeneracy of the nuclear states is lifted by interaction with external fields [Blume and Kistner, 1968; Hannon and Trammell, 1969]. Sturhahn and Gerdaun [1994] give a complete, numerically efficient, method to derive the nuclear reflection, including the calculations of the energy eigenstates from the hyperfine parameters of the nuclei. The resulting program package CONUSS was later extended for reflection gratings and arbitrary surface roughness [Röhlsberger, 1999]. The following framework of the dynamical scattering theory for nuclear resonant scattering (NRS) follows mainly Röhlsberger [1999, 2004] for its clear presentation of the subject.

2.5.1. Propagation equation

In general every mathematical approach for this problem may be transformed into a set of coupled linear differential equations with constant coefficients [Batterman and Cole, 1964]. The wave field \mathbf{A} varied by the propagation matrix \mathbf{F} over the depth of the sample z may then be written in the form

$$\partial_z \mathbf{A}(z) = i\mathbf{F}(z)\mathbf{A}(z), \quad (2.65)$$

where the scattering target is assumed homogeneous in the (x, y) -plane. A detailed calculation of this relation is given in A.2. There we also find the appropriate form of the propagation matrix \mathbf{F} as

$$\mathbf{F} \equiv \begin{bmatrix} \mathbf{f}_{++} + \mathbf{k}_{+z} & \mathbf{f}_{+-} \\ \mathbf{f}_{-+} & \mathbf{f}_{--} + \mathbf{k}_{-z} \end{bmatrix}, \quad (2.66)$$

with the components

$$\mathbf{f}_{++} \equiv \frac{1}{k_{+z}} \sum_j \rho_j \mathbf{M}_j(\mathbf{k}_+, \mathbf{k}_+), \quad (2.67)$$

and

$$\mathbf{f}_{-+} \equiv \frac{1}{k_{-z}} \frac{e^{2ik_{-z}d} - 1}{2ik_{-z}d} \sum_j \rho_j \mathbf{M}_j(\mathbf{k}_-, \mathbf{k}_+) \quad (2.68)$$

with the scattering vectors of transmission $\mathbf{k}_+ = [k_{0x}, k_{0y}, k_{0z}]^T$ and reflection $\mathbf{k}_- = [k_{0x}, k_{0y}, -k_{0z}]^T$ and their respective z -components $k_{\pm z} = \pm k_{0z}$. At this point I may note that for grazing incidence scattering geometry $|k_{\pm z}d| \ll 1$ the scattering channel transition amplitudes, more precisely the off-diagonal matrices, approach their diagonal counterparts

$$\begin{aligned} \mathbf{f}_{-+} &\approx \frac{1}{k_{-z}} \frac{1 + 2ik_{-z}d - 1}{2ik_{-z}d} \sum_j \rho_j \mathbf{M}_j(\mathbf{k}_-, \mathbf{k}_+) \\ &= \frac{1}{k_{-z}} \sum_j \rho_j \mathbf{M}_j(\mathbf{k}_-, \mathbf{k}_+) \\ &\approx \mathbf{f}_{--} \approx -\mathbf{f}_{+-} \approx -\mathbf{f}_{++}. \end{aligned} \quad (2.69)$$

where the amplitudes for transmission and reflection only differ in the sign. Due to the small scattering vector the scattered field does not depend on the internal structure of the sample, thus in specular reflection the atomic scattering amplitudes are only varying with the modulus of the wave vectors.

For the general form of Eq. (2.65) I previously assumed the solid to be infinite and homogeneous in the plane perpendicular to the scattering vector. If one assumes the layer additionally homogeneous in parallel to it, in other words \mathbf{F} does not depend on z , the solution for the electric field amplitude \mathbf{A} is very similar to the standard forward scattering amplitude

$$\mathbf{A}(z) = e^{i\mathbf{F}z} \mathbf{A}(0). \quad (2.70)$$

In the case of simultaneous dynamical scattering in transmission and reflection direction, however, \mathbf{F} is of the form in Eq. (2.66). Therefore the propagation operator is identified as a matrix exponential.

The problem is now to find a matrix \mathbf{S} that diagonalizes \mathbf{F} . Of course the columns of this matrix \mathbf{S} are the eigenvectors of \mathbf{F} and I may write

$$\mathbf{F}_D = \mathbf{S}^{-1} \mathbf{F} \mathbf{S}, \quad (2.71)$$

with the diagonal matrix \mathbf{F}_D . In this form it is possible to simply calculate the exponential of the eigenvalues and employ back transformation to the original basis as

$$e^{i\mathbf{F}z} = \mathbf{S}e^{i\mathbf{F}_D z}\mathbf{S}^{-1}, \quad (2.72)$$

explained in detail in Sec. A.3.

One way to calculate the dynamic reflectivity from a slowly varying inhomogeneous layer would be to split it in a sufficiently large number N of homogeneous sublayers with possibly different propagation matrices \mathbf{F}_j and thicknesses d_j as seen in Fig. 2.3. Now the solution for the inhomogeneous problem is just a matter of repeated matrix multiplication of the individual matrix exponentials

$$\mathbf{A}(d_1 + \dots + d_N) = e^{i\mathbf{F}_N d_N} \dots e^{i\mathbf{F}_1 d_1} \mathbf{A}(0) = \mathbf{L}(D)\mathbf{A}(0), \quad (2.73)$$

with the overall propagation matrix \mathbf{L} for the inhomogeneous layer with thickness D . If we recollect the structure of the individual propagation matrices and the field amplitude vector we can rewrite this as a matrix equation

$$\begin{bmatrix} \mathbf{A}_+(D) \\ \mathbf{A}_-(D) \end{bmatrix} = \begin{bmatrix} \mathbf{L}_{++}(D) & \mathbf{L}_{+-}(D) \\ \mathbf{L}_{-+}(D) & \mathbf{L}_{--}(D) \end{bmatrix} \begin{bmatrix} \mathbf{A}_+(0) \\ \mathbf{A}_-(0) \end{bmatrix}. \quad (2.74)$$

The incoming field is known $\mathbf{A}_+(0) = \mathbf{A}_0$ and the back traveling field from the substrate is taken to be neglectable $\mathbf{A}_-(D) = 0$, thus the solution for the reflected field at the surface and the transmitted field can be deduced from the equations

$$\begin{aligned} \mathbf{A}_+(D) &= \mathbf{L}_{++}\mathbf{A}_0 + \mathbf{L}_{+-}\mathbf{A}_-(0) \\ 0 &= \mathbf{L}_{-+}\mathbf{A}_0 + \mathbf{L}_{--}\mathbf{A}_-(0). \end{aligned} \quad (2.75)$$

The reflected field can be directly calculated from

$$\mathbf{A}_-(0) = -\mathbf{L}_{--}^{-1}\mathbf{L}_{-+}\mathbf{A}_0 \equiv \mathbf{R}\mathbf{A}_0 \quad (2.76)$$

and this result can be used to express the transmitted field as

$$\mathbf{A}_+(D) = (\mathbf{L}_{++} - \mathbf{L}_{+-}\mathbf{L}_{--}^{-1}\mathbf{L}_{-+})\mathbf{A}_0 \equiv \mathbf{T}\mathbf{A}_0, \quad (2.77)$$

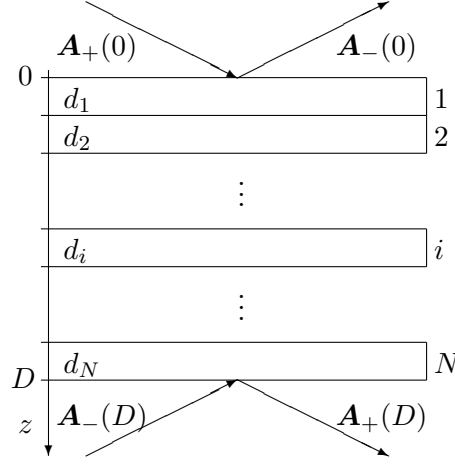


Figure 2.3.: Sketch of $N - 1$ stacked layers on top of a substrate. At the surface $z = 0$ the incoming and outgoing fields are denoted by $\mathbf{A}_+(0)$ and $\mathbf{A}_-(0)$ and the corresponding fields at the substrate are $\mathbf{A}_+(D)$ and $\mathbf{A}_-(D)$.

where the total scattering matrices for reflection and transmission are denoted by \mathbf{R} and \mathbf{T} , respectively. To recollect the $\mathbf{L}_{\pm\pm}$ are themselves matrices to account for the polarization dependence. The scattering properties of the individual layer j are included in the respective propagation matrix \mathbf{F}_j , consisting of separate electronic and nuclear resonant atomic scattering amplitudes. The nuclear resonant scattering amplitudes holds all the hyperfine parameters and are weighted by the enrichment of the resonant nuclei in the individual layer.

Finally the intensity for arbitrary polarization of the incoming beam and polarization analysis of the detector can be expressed using density matrix formalism for the polarization states. As commonly established the intensity will be the weighted sum over all possible paths from the initial polarization to the final polarization state

$$\begin{aligned}
 I &= \sum_{m,n} \alpha_m \beta_n |\langle n | \mathbf{R} | m \rangle|^2 = \sum_{m,n} \alpha_m \beta_n \langle n | \mathbf{R} | m \rangle \langle m | \mathbf{R}^\dagger | n \rangle \\
 &= \sum_n \beta_n \langle n | \mathbf{R} \boldsymbol{\rho}_i \mathbf{R}^\dagger | n \rangle = \text{tr} \left(\boldsymbol{\rho}_f \mathbf{R} \boldsymbol{\rho}_i \mathbf{R}^\dagger \right)
 \end{aligned} \tag{2.78}$$

where the polarization density for the initial and final polarization state matrices, $\boldsymbol{\rho}_i = \sum_m \alpha_m |m\rangle \langle m|$ and $\boldsymbol{\rho}_f = \sum_n \beta_n |n\rangle \langle n|$, respectively, can be conveniently decomposed into the identity and the Pauli matrices, as these matrices span the full vector space of

Hermitian (2×2)-matrices

$$\rho_{i,f} = \frac{1}{2} \begin{bmatrix} 1 + \xi_1 & \xi_2 + i\xi_3 \\ \xi_2 - i\xi_3 & 1 - \xi_1 \end{bmatrix} = \frac{1}{2} (\mathbf{1} + \xi_1 \boldsymbol{\sigma}_3 + \xi_2 \boldsymbol{\sigma}_1 + \xi_3 \boldsymbol{\sigma}_2), \quad (2.79)$$

and the polarization factors ξ_i fulfill $|\xi_i| \leq 1$. In this representation ξ_1 is a linear polarized part in a orthogonal basis, ξ_2 a linear polarized as well, but with the basis $\pi/4$ rotated and finally ξ_3 a circular polarized part.

For our case of an approximately fully σ -polarized incoming beam (normal to the incident plane) of $\xi_1 = 1$ and $\xi_2 = \xi_3 = 0$ and no polarization analysis in the detector $\xi_1 = \xi_2 = \xi_3 = 0$ I can express the resulting intensity in terms of the reflectivity matrix components as follows

$$I = \frac{1}{2} \left(|R_{11}|^2 + |R_{21}|^2 \right). \quad (2.80)$$

2.5.2. Scattering amplitude

Up to this point the scattering theory was kept very general when it comes to the actual scattering mechanism. In this section I want to discuss the characteristics of nuclear resonant scattering in particular as described in Hannon and Trammell [1969]; Sturhahn and Gerdau [1994]; Röhlberger [1999]. Due to small interaction between electronic and nuclear currents in the atom the atomic scattering amplitude can be separated into an electronic and a nuclear part $\mathbf{M}_{\mu\nu} = \mathbf{E}_{\mu\nu} + \mathbf{N}_{\mu\nu}$. The electronic part conserves the polarization and is therefore diagonal

$$\mathbf{E}_{\mu\nu}(\omega) = (\mathbf{e}_\mu \cdot \mathbf{e}_\nu) \left(-Zr_0 + i \frac{k_0}{4\pi} \sigma(\omega) \right) \quad (2.81)$$

with the atomic number Z , the classical electron radius r_0 and the total absorption cross section σ . For the small energy range of nuclear resonant scattering this relation can be associated with the more common complex refraction index $n = 1 - \delta + i\beta$ as

$$\mathbf{E}_{\mu\nu}(\omega) = (\mathbf{e}_\mu \cdot \mathbf{e}_\nu) \frac{k_0^2}{2\pi\rho} (-\delta + i\beta). \quad (2.82)$$

The nuclear resonant scattering is specified by

$$\mathbf{N}_{\mu\nu}(\omega) = \sum_{M=-L}^L (\mathbf{Y}_{LM}^*(\mathbf{k}_0) \cdot \mathbf{e}_\mu) (\mathbf{e}_\nu \cdot \mathbf{Y}_{LM}(\mathbf{k}_0)) F_{LM}(\omega) \quad (2.83)$$

for a 2^L -pole resonance with the vector spherical harmonics \mathbf{Y}_{LM} . These contain the anisotropy of the photon absorption and reemission. The function F_{LM} contains the energy dependence

$$F_{LM}(\omega) \equiv \frac{2\pi f_{\text{LM}}\Gamma_0}{k_0(2j+1)(1+\alpha)} \sum_{m=-j}^j \frac{C(j, L, J, M, m)^2}{E_{J, m+M} - E_{j, m} - \hbar\omega - i\Gamma_0/2} \quad (2.84)$$

with the sum over all ground states m and the energy difference between the ground state $|j, m\rangle$ and the photon energy ω on the one hand and the excited state $|J, m+M\rangle$ on the other and the natural line width Γ_0 . The Clebsch-Gordan coefficients C result from the angular momentum coupling. A numerical recipe to calculate these coefficients is lined out at Sec. B.4. Additional probability factors are the Lamb-Mössbauer f_{LM} and a factor considering internal conversion probability α .

The directional part of the nuclear scattering length $\mathbf{N}_{\mu\nu}$ may be expanded in terms of the magnetic quantization axis \mathbf{m} of the atoms. So for the typical electric dipole transition ($L = 1$), where I denote $F_{1M} \equiv F_M$ and subsequently $F_+ \equiv F_{+1} + F_{-1}$, $F_- \equiv F_{+1} - F_{-1}$ and $F \equiv 2F_0 - F_{+1} - F_{-1}$, we get

$$\mathbf{N}_{\mu\nu}(\omega) = \frac{3}{16\pi} \left((\mathbf{e}_\mu \cdot \mathbf{e}_\nu) F_+ - i(\mathbf{e}_\mu \times \mathbf{e}_\nu) \cdot \mathbf{m} F_- + (\mathbf{e}_\mu \cdot \mathbf{m})(\mathbf{e}_\nu \cdot \mathbf{m}) F \right). \quad (2.85)$$

In the most intuitive representation of a linear polarization basis with the basis vectors perpendicular to the wave vector in general, and parallel \mathbf{s} and perpendicular \mathbf{p} to the scattering plane in particular, this matrix can be expressed as

$$\mathbf{N} = \frac{3}{16\pi} \begin{bmatrix} F_+ + (\mathbf{p} \cdot \mathbf{m})^2 F & -i(\mathbf{k}_0 \cdot \mathbf{m}) F_- - (\mathbf{s} \cdot \mathbf{m})(\mathbf{p} \cdot \mathbf{m}) F \\ i(\mathbf{k}_0 \cdot \mathbf{m}) F_- - (\mathbf{s} \cdot \mathbf{m})(\mathbf{p} \cdot \mathbf{m}) F & F_+ + (\mathbf{s} \cdot \mathbf{m})^2 F \end{bmatrix} \quad (2.86)$$

This form is ideal to immediately see the symmetries of a specific scattering experiment determined by the direction of the incoming beam, its polarization and the orientation of the magnetic field inside the sample. Additionally the off-diagonal elements show

the strong polarization mixing of nuclear resonant scattering.

EXPERIMENT

3.1. Samples

3.1.1. General

In general anisotropic studies in the $L1_0$ -structure are scarce due to its tetragonal nature. Even single crystalline samples always feature domains with the 3 possible orientation of the distinguished axis. The bulk lattice constants for the intermetallic tetragonal $L1_0$ -phase of FePt are $a_1 = a_2 = a = 0.38504(8)$ nm and $a_3 = c = 0.37212(3)$ nm [Kudielka and Runow, 1976], respectively, resulting in a lattice misfit of 9% on a MgO(001) surface (0.421 nm). The induced strain is often reduced by various buffer layers (i.e. Pt). For low deposition temperatures, however, large lattice misfit may enhance the long-range order [Seki et al., 2004]. To avoid island growth [Kim et al., 2002] and guarantee a flat film surface the FePt films for this study are directly grown on MgO under well tested conditions [Laenens et al., 2009]. Unfortunately it is not possible to prepare a film with the magnetic main axis, which is along the c lattice direction, purely parallel to the film surface (a -variant) on MgO(001) like in Fig. 3.1(c) at low enough temperatures to avoid dilution of the isotopic multilayers, as it is for the c -variant (perpendicular as shown in Fig. 3.1(a)) [Rennhofer et al., 2006]. On MgO(110), however, Laenens et al. found a way to prepare FePt films with the (100)-plane rotated by 45° to the surface [Laenens et al., 2007]. From this orientation shown in Fig. 3.1(b) and the results on diffusion in c -direction of Rennhofer et al. [2006] I can deduce the diffusion constant in the a -direction and complete the picture of Fe self diffusion in

FePt.

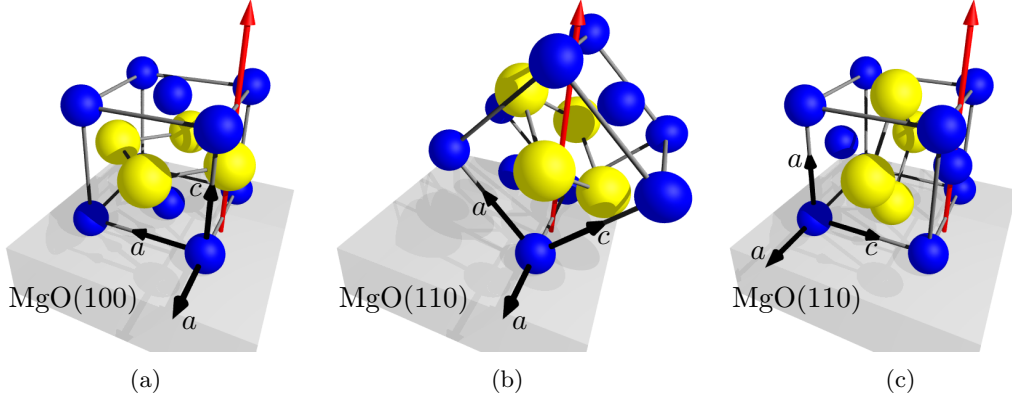


Figure 3.1.: $L1_0$ -FePt on MgO. (a) c -variant on (100)-plane of the previous study of Rennhofer et al. [2006]. (b) 45° rotated structure on (110)-plane. (c) a -variant on (110)-plane. The red arrow visualizes the measured diffusion projection.

3.1.2. Sample preparation

The samples have been prepared by our collaborators in Leuven¹. The nominal composition was intended to be $[^{57}\text{FePt}(2\text{ nm})/^{nat}\text{FePt}(3\text{ nm})]_{10}/\text{MgO}(110)$. The method of choice to prepare films with thicknesses of a few nanometers is molecular beam epitaxy (MBE). In fact this method is capable of sub-mono layer films. The samples have been prepared at a substrate temperature of 623 K and a pressure $p < 10^{-10}$ mbar. The substrate was annealed previous to film growth to clean its surface.

A quartz micro balance basically translates a shift of the vibrational resonance frequency to the deposited mass per unit area m_A according to the Sauerbrey equation [Sauerbrey, 1959]

$$\frac{\Delta f}{f_f} \approx \frac{2f}{Z} m_A \quad (3.1)$$

with the frequency of the fundamental f_f and the acoustic impedance Z , which for a quartz crystal is $8.8 \times 10^6 \text{ kg m}^{-2} \text{ s}^{-1}$. The frequency is recorded over time, therefore

¹B. Laenens, K.U. Leuven, Nuclear and radiation physics

also the mass m_A should be seen as a mass per unit area and time.

If one wants to grow a film with 2 components on a substrate the ratio of the number of particles per unit area has to be the ratio of the desired atomic composition of the material. To convert the mass area density to a number area density I divide by the atomic masses of Fe $m_{\text{Fe}} = 55.845$ u and Pt $m_{\text{Pt}} = 195.1$ u with the atomic mass unit $1 \text{ u} = 1.661 \times 10^{-27}$ kg. For convenience the mass gain can be translated to a thickness gain d , when the density ρ of the material is known. Thus for the relevant number area density we have

$$n_A = \frac{m_A}{m_{\text{atom}}} = \frac{\rho d}{m_{\text{atom}}}. \quad (3.2)$$

The growth rates measured by quartz-crystal microbalance have been $d_{\text{Fe}} = 2.7 \times 10^{-3} \text{ nm s}^{-1}$ for ^{57}Fe and $^{\text{nat}}\text{Fe}$ and $d_{\text{Pt}} = 3.4 \times 10^{-3} \text{ nm s}^{-1}$ for Pt. If I insert these into the equation above I get for the number area densities $n_{\text{Fe}} = 0.229 \text{ nm}^{-2} \text{ s}^{-1}$ and $n_{\text{Pt}} = 0.225 \text{ nm}^{-2} \text{ s}^{-1}$, respectively. This relates to a nominal concentration ratio of $\text{Fe}/\text{Pt} = 1.02$ suggesting a fairly stoichiometric film.

3.1.3. Rutherford backscattering

A Rutherford backscattering experiment (RBS) on the as-prepared samples revealed a slight off-stoichiometric composition with $\text{Fe}_{56}\text{Pt}_{44}$. This slightly Fe-rich chemical composition is still well in the center of the L1_0 -phase shown in Fig. 1.1. However comparisons with literature have to be made with care, because the resulting structural antisites and lattice distortions may significantly influence the parameters.

3.1.4. X-ray diffraction

The pseudo-cubic unit cell of the L1_0 -lattice consists of 2 atoms of one sort at $\mathbf{r}_1 = [0, 0, 0]$ and $\mathbf{r}_2 = [1/2, 1/2, 0]$ and 2 atoms of an other sort at $\mathbf{r}_3 = [1/2, 0, 1/2]$ and $\mathbf{r}_4 = [0, 1/2, 1/2]$ described by the atomic form factors of f_1 and f_2 , respectively. The structure factor of the Miller plane (hkl) can be calculated by

$$\begin{aligned} S_{hkl} &= \sum_i f_i e^{-i\mathbf{G}_{hkl} \cdot \mathbf{r}_i} \\ &= \sum_i f_i e^{-2\pi i(hx_i + ky_i + lz_i)} \\ &= f_1 \left(1 + e^{-\pi i(h+k)} \right) + f_2 \left(e^{-\pi i(h+l)} + e^{-\pi i(k+l)} \right) \end{aligned} \quad (3.3)$$

for the real space and reciprocal lattice vectors $\mathbf{r}_i = x_i \mathbf{a}_1 + y_i \mathbf{a}_2 + z_i \mathbf{a}_3$ and $\mathbf{G}_{hkl} = h\mathbf{b}_1 + k\mathbf{b}_2 + l\mathbf{b}_3$, respectively, and applying the relation defining the reciprocal lattice $\mathbf{a}_i \cdot \mathbf{b}_j = 2\pi\delta_{ij}$. Therefore we have two different expressions for the structure factor, to be specific $2(f_1 + f_2)$ and $2(f_1 - f_2)$, for all the Miller planes. The structure factor basically gives the relative refraction peak intensity besides the intensity decrease for increasing refraction angle. For a pure fcc structure we would have $f_1 = f_2 \equiv f$, thus

Table 3.1.: Table of expected diffraction peaks for Miller planes (hkl) of the L1₀-lattice at diffraction angles θ . The rightmost column of diffraction peaks would vanish for a pure fcc-crystal or a solid solution.

S_{hkl}		$2(f_1 + f_2)$	$2(f_1 - f_2)$
$h^2 + k^2 + l^2$	θ (°)		
1	11.95		(001)
2	16.43		(110)
3	20.52	(111)	
4	23.58, 24.46	(200) (020), (002)	
5	26.77		(201) (021)
6	30.09		(112)
8	34.45, 35.15	(220), (202) (022)	
9	37.04		(221)
12	44.51	(222)	

the familiar $2(f_1 + f_2) = 4f$ and $2(f_1 - f_2) = 0$. This means that the refraction peaks for the planes in the rightmost column of Tab. 3.1 would be non-existent. Due to the lower symmetry of L1₀ additional refraction maxima appear, where only h and k are even or odd simultaneously but l is the opposite.

The angles of the refraction peaks can be calculated from the Laue condition

$$\mathbf{q} = \mathbf{G}_{hkl}, \quad (3.4)$$

where the reciprocal lattice vector \mathbf{G}_{hkl} is perpendicular to the (hkl)-planes, and thus the modulus of the scattering vector \mathbf{q} for specular reflection is related to the wave vector of the photon \mathbf{k} and subsequently its wavelength λ by $|\mathbf{q}| = 2|\mathbf{k}|\sin\theta = 4\pi\sin\theta/\lambda$. The reciprocal lattice vector on the other hand is defined above, where the basis of the

reciprocal lattice can be expressed by the basis in the real space as

$$\mathbf{b}_1 = 2\pi \frac{\mathbf{a}_2 \times \mathbf{a}_3}{\mathbf{a}_1 \cdot (\mathbf{a}_2 \times \mathbf{a}_3)} \quad (3.5)$$

with cyclic permutations of the indices. Furthermore the orthogonal basis of the tetragonal lattice transforms to an orthogonal basis in the reciprocal space, thus the modulus of the reciprocal vector is simply $|\mathbf{G}_{hkl}| = \sqrt{(h\mathbf{b}_1)^2 + (k\mathbf{b}_2)^2 + (l\mathbf{b}_3)^2}$, and for the individual reciprocal basis vectors I get $|\mathbf{b}_i| = 2\pi/|\mathbf{a}_i|$. The moduli of the real space basis vectors are denoted by $|\mathbf{a}_1| = |\mathbf{a}_2| = a$ and $|\mathbf{a}_3| = c$. Finally I can put all this together and get from the Laue condition in Eq. (3.4) for the Bragg angle

$$\theta = \arcsin\left(\frac{\lambda |\mathbf{G}_{hkl}|}{4\pi}\right) = \arcsin\left(\frac{\lambda}{2} \sqrt{(h/a)^2 + (k/a)^2 + (l/c)^2}\right). \quad (3.6)$$

So for a Cu- K_α source of wavelength $\lambda = 0.154$ nm the corresponding Bragg angles are given in the second column of Tab. 3.1.

An X-ray diffraction scan on the as prepared samples with the scattering vector perpendicular to the surface reveals intensity maxima at Bragg angles of 16.48° and 34.77° for FePt (110) and {220} as shown in Fig. 3.2, respectively, besides the MgO {220} peak at 31.15° . On the one hand, from the FePt(220) diffraction I can conclude that the (220) planes are in fact grown parallel to the surface. On the other hand, however, the sheer existence of the (110) peak also implies that in part of the film the c -axis is oriented parallel to the surface, which translates to a domain with diffusion purely in a -direction. On closer examination of the {220} peak, the width and asymmetry of the latter also suggests the presence of all three orientations. In a second polar scan with the scattering vector rotated 45° to the surface normal and the sample rotated around its surface normal one finds MgO(200) at $2\theta = 42.9^\circ$ and FePt(200) at $2\theta = 47.5^\circ$ at polar angles of 90° and 270° , respectively, which suggests an orientation as shown in Fig. 3.1 and confirms the epitaxial growth on the substrate.

3.1.5. Conversion electron Mössbauer spectroscopy

These results are also confirmed by conversion electron Mössbauer spectroscopy measurements (CEMS) analogous to Laenens et al. [2007]. In the L1₀ lattice of FePt the main axis of the magnetic hyperfine field is always parallel to the c -axis [Shinjo and

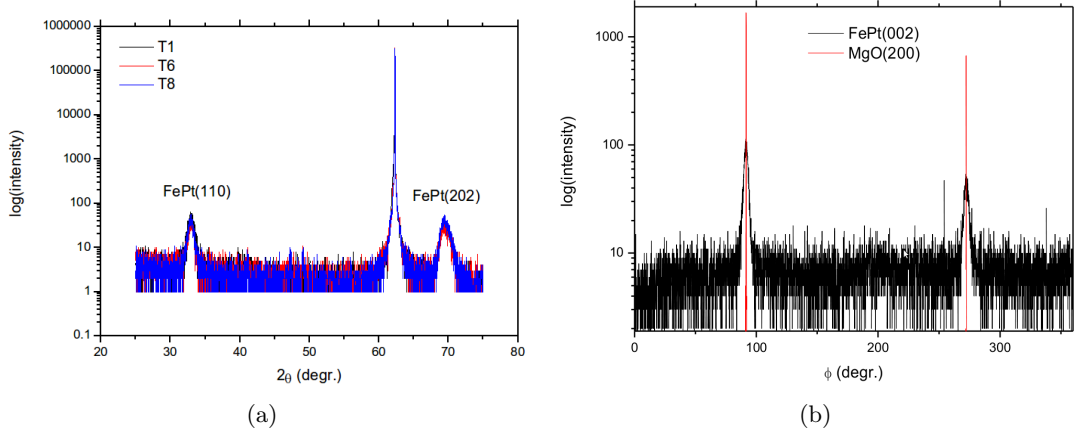


Figure 3.2.: XRD scan on the as-prepared samples with $\text{Cu-}K_\alpha$ source. (a) The $\text{MgO}\{220\}$ peak is located in the center. The less intense $\text{FePt}\{110\}$ and $\{220\}$ peaks can be found on either side of the substrate reflex. (b) Scan over rotation angle for planes rotated 45° to the surface show $\text{MgO}(200)$ ($2\theta = 42.9^\circ$) and $\text{FePt}(002)$ ($2\theta = 47.5^\circ$) at the angles 90° and 270° .

Keune, 1999]. The relative intensity of the second and fifth to the inner resonances $3h : f(\theta)h : h : h : f(\theta)h : 3h$, compare to Tab. 2.1, is directly related to the angle θ between the wave vector of the incoming photon and the direction of the magnetic hyperfine field, which is the c -direction in the tetragonal structure, by

$$f(\theta) = \frac{4 \sin^2 \theta}{1 + \cos^2 \theta}. \quad (3.7)$$

The acquired spectra are fitted using 3 independent sites by a Voigt-based method for arbitrary distribution of magnetic hyperfine fields described in Sec. 2.4.3. The resulting fits are displayed in Fig. 3.3. The hyperfine parameters are simultaneously fitted for all samples, as they are parts of one large, homogeneously prepared sample. Only the standard deviation of the normal distribution of the magnetic hyperfine field of site 3 of the as prepared sample T1 was decoupled from the one of the same site in the other samples to account for higher disorder and resulted in $\sigma_B = 1.11$ T. It is assumed that this disorder is vanishing during annealing. The other parameters are listed in Tab. 3.2. Besides the as-prepared one, the samples show a majority, in average $w = 0.72$, of domains with a 45° canted structure (see site 1) as intended for

the experiment. The other sites, denoted as site 2 and site 3 in Fig. 3.3 and Tab. 3.2, suggest so called a -variant domains with the magnetic axis parallel to the surface. In this fraction the diffusion constant is thus purely measured in a -direction. The majority, however, contributes with a reduced diffusion constant, discussed in more detail below. The resulting hyperfine parameters are subsequently used in the calculation of the nuclear resonant reflectivity.

Table 3.2.: CEMS parameters for the 3 different sites. All the hyperfine parameters, i.e. the isomer shift (IS), the quadrupole splitting (QS) and the magnetic hyperfine field B and its distribution σ_B , have been simultaneously fitted for all the samples, except the magnetic field distribution of the first sample was decoupled to account for higher disorder. The weights of the respective sites are listed in the rightmost columns.

site	IS (mm/s)	QS (mm/s)	B (T)	σ_B (T)	θ ($^\circ$)	fraction of sites by sample					
						T1	T2	T3	T4	T6	T8
1	0.277	0.207	28.36	0.68	45	0.28	0.65	0.84	0.69	0.77	0.68
2	0.269	0.000	30.97	2.13	90	0.52	0.25	0.12	0.23	0.18	0.26
3	0.321	0.207	27.76	0.20	90	0.20	0.10	0.04	0.08	0.05	0.06

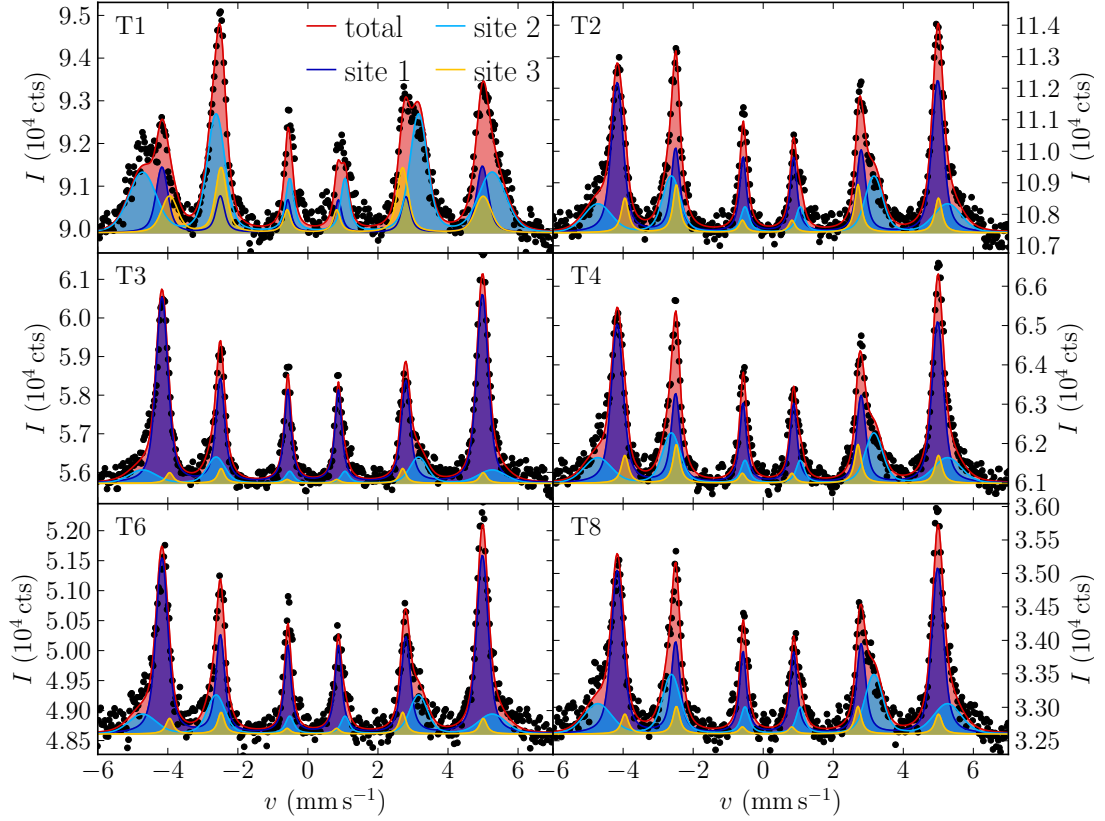


Figure 3.3.: CEMS spectra of the FePt samples. The as-prepared sample (T1) shows significant fractions of domains with different orientation. The measured samples (T2, T3, T4, T6, T8) show good ordering with a majority of domains with the c -axis oriented 45° to the incoming photons, which is the surface normal (site 1). In the other 2 sites with different hyperfine parameters the c -axis is oriented parallel to the surface.

3.1.6. Transmission electron microscopy

As mentioned above the bulk lattice constants for the intermetallic tetragonal $L1_0$ -phase of FePt are $a_1 = a_2 = a = 0.38504(8)$ nm and $a_3 = c = 0.37212(3)$ nm [Kudielka and Runow, 1976], respectively, resulting in a lattice misfit of 9% on a MgO(001) surface (0.421 nm). For the c -variant of the FePt films, where the shorter c -direction is oriented perpendicular to the surface, atomic resolution transmission electron microscopy images exist and a representative one is shown in Fig. 3.4(a).

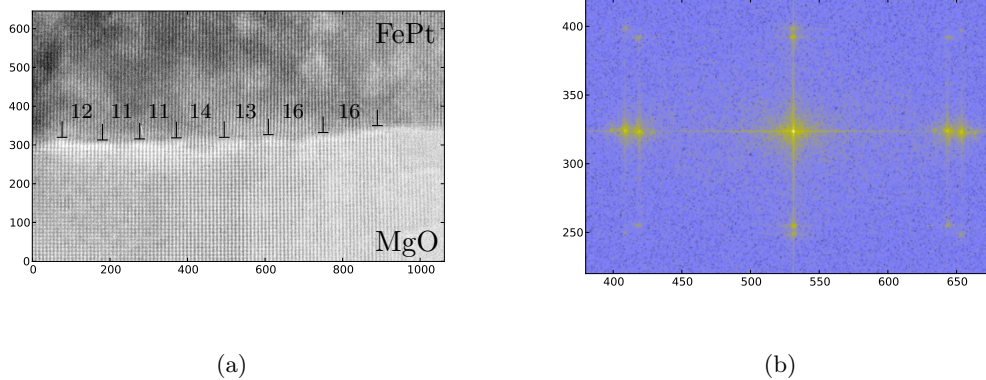


Figure 3.4.: (a) TEM picture for c -FePt² (b) Fourier analysis of the same picture clearly shows two sharp, distinct peaks, corresponding to the two different lattice constants of the substrate and the FePt film.

On the basis of these images I want to discuss the film quality and its consequences. In Fig. 3.4(a) the interface between the lighter substrate MgO and the darker FePt-film on top is shown in the $[010]$ -direction. The alternating pattern is the result of an electron beam dynamically scattered by stacks of atoms. Although the visible brighter spots may not be the atom stacks themselves, at least the periodicity can be identified as the fundamental lattice period. This level of detail is actually referred to as atomic resolution TEM.

The misfit between MgO and the a -direction of FePt is relaxed by edge dislocations (positions marked in the image) with the dislocation line oriented perpendicular the image plane. The numbers between the dislocations indicate the respective distance in

²Christian Rentenberger, Faculty of Physics, University of Vienna

lattice planes. The average distance is in good agreement with the lattice misfit of 9%. Additionally one can see that the lattice relaxes to a regular structure within a few atomic planes from the interface to the substrate. Fig. 3.4(b) shows the shifted Fourier transform of this exact TEM image. We can clearly see two separated spots for the two different lattice constants of the substrate and the film structure. For a gradual change in lattice constant one would observe only one spot for the substrate.

3.2. Nuclear resonant experiment

The main experiment, successive thermal treatment and nuclear resonant scattering, was conducted at ESRF, Grenoble. The details are described in this chapter.

3.2.1. Thermal treatment

The samples were successively annealed at a fixed temperature (653 K, 673 K, 698 K, 723 K or 743 K) in a quartz-tube furnace in vacuum better than 10^{-6} mbar.

The layout of the furnace can be described as follows: A sample is placed in a sample holder made of Ta mesh coupled to a magnet by a long thin rod. This container is slid into a quartz tube that can be evacuated down to a pressure of $p \leq 1 \times 10^{-6}$ mbar. The furnace itself consists of a resistive heating coil on an outer quartz-tube the first one can be introduced into. The coil is wrapped by Al-oxide paper for its good insulation due to high porosity. Additionally a layer of Al foil is used to reflect heat radiation and therefore minimize heat loss. The sample holder can be pulled into and out of the hot zone in vacuum condition by an external magnet. The heat transfer is solely based on radiation, thus allowing for nearly instantaneous establishment of the desired temperature due to the small heat capacity of the sample.

Prior to the experiment the diffusivity was unknown so it had to be extrapolated from data at higher temperature to make an educated guess about the length of the first annealing steps. To avoid complete homogenization initially, the time steps were chosen conservatively. For the ongoing experiment the annealing times had to be adapted successively to get measurable dilution of the nuclear resonant superstructure in the sample in a reasonable amount of time steps, i.e. $N \lesssim 10$. Between the heat treatments the samples were pulled out of the furnace to essentially freeze the diffusion. The nuclear resonant Θ - 2Θ -scan was accumulated ex-situ on the beamline at ambient

conditions. The individual annealing times for the samples actually measured are shown in Tab. 3.3.

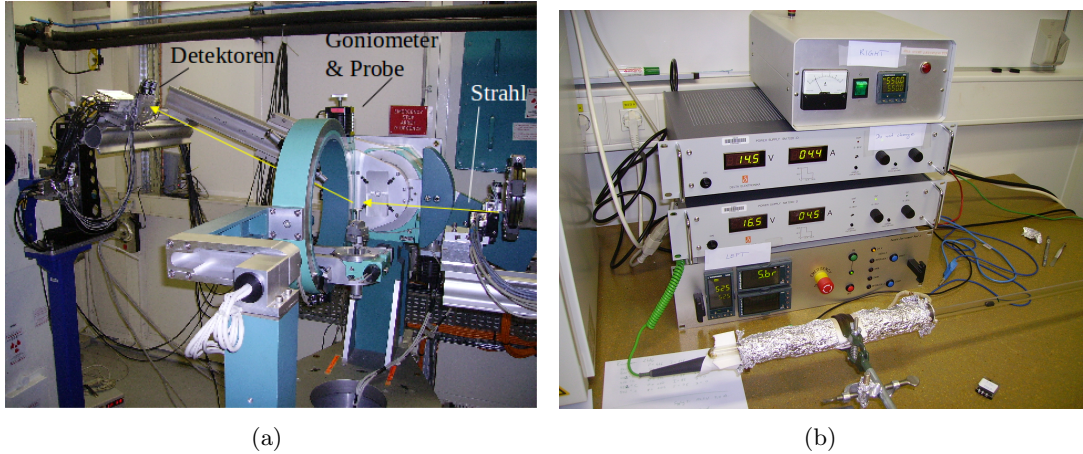


Figure 3.5.: Experimental setup: (a) goniometer at ID22N at ESRF, (b) quartz tube with resistive heating coil in shielded with Al oxide paper and Al foil.

Table 3.3.: Annealing times for the samples in the quartz tube furnace Fig 3.5(b). The anneal times represent the exact time the samples resided in the hot zone of the quartz tube in vacuum condition. The total anneal time therefore is calculated by adding the individual annealing durations .

sample	T (K)	anneal times (min)										
		1	2	3	4	5	6	7	8	9	10	
T4	653	30	45	90	180	180	180	300				
T2	673	35	15	30	20	60	60	120	120	120	210	
T3	698	30	10	30	30	30	30	30				
T6	723	7	7	7	9	15						
T8	743	5	10	5	10							

3.2.2. Electronic reflectivity

The instantaneously scattered electronic reflectivity, ignored for the actual nuclear resonant experiment, is registered in an additional detector to give additional information about the actual thickness of the prepared films. Similar to Bragg reflection the

interference between the reflection on the surface and on the surface-substrate interface gives rise to intensity undulations over the scattering angle. Quite intuitively the much larger distance between the interfering interfaces translates to undulations with smaller distances in reciprocal space. In a first approximation the overall thickness of our FePt film on the MgO substrate using $q = 4\pi \sin \theta / \lambda \approx 4\pi\theta / \lambda$ for $\theta \ll 1$ is given in Pietsch et al. [2004]

$$D \approx \frac{\lambda}{2\Delta\theta} \approx \frac{2\pi}{\Delta q} \quad (3.8)$$

with the wave length of the X-rays λ , and the undulation period angle $\Delta\theta$ and its equivalent, the period in modulus of the reciprocal vector Δq . Alternatively one can calculate the electronic reflectivity employing the formalism of Eq. (2.76). In this case the strongly energy dependent nuclear resonant part of Eq. (2.86) can be neglected, leaving only the electronic part of Eq. (2.82), to save computation time. The overall thickness of $D = 39.7(1)$ nm is quite consistent over the range of samples. Deviations from the nominal thickness are rather common using the MBE method. They are attributed to incorrect calibration correcting for a geometry factor. The total multilayer sample thickness is of minor importance anyway. The repeatability of the single layer thickness is here the essential point. For experiments involving effects that strongly depend on the thickness of the layers, e.g., quantum effects of ultra thin layers, a rate calibration via a second method has to be performed, i.e. reflectivity measurements as described above. For this reason I simply assumed a different but constant evaporation rate, so the individual thicknesses of the sublayers have been adjusted accordingly for the evaluation.

3.2.3. Nuclear reflectivity

The nuclear scattering experiment was conducted at the beamline ID22N. The description of the layout of the beamline is taken from R uffer and Chumakov [1996] and for up-to-date information from the official beamline homepage at R uffer and Chumakov [2012]. The schematic layout is shown in Fig. 3.6. The beamline is also used for other purposes than nuclear resonant scattering, therefore it is not completely optimized for this type of experiment as i.e. ID18. From right to left the beamline consists of the undulators producing the x-rays from roughly sinusoidally accelerated electrons. Additionally there is a compound refractive lens system (CRL) for collimation in the

front-end. Although the resonance width is only 4.66 neV in principle no particular monochromator is necessary, because in contrast to conventional Mössbauer spectroscopy the excellent time resolution of the synchrotron is used to select the resonant scattering events. However, to prevent detector overload and limit background intensity some effort to limit the energy range has to be made. A pre-mirror (MR) combined with a high heat load monochromator (HHLM) makes up the optics hutch (OH1) for rough monochromatization. The narrow energy bandwidth necessary is achieved by the high resolution monochromator in the second experimental hutch (EH2) completed with a sagittal focusing set-up (FM). At this beamline only the third experimental hutch (EH3) is devoted to NRS. As a detector a special Avalanche photo diode (APD) is used to measure single photons a few nanoseconds after the extremely intense electronic reflectivity of $10^9 \text{ s}^{-1} \cdot 176 \text{ ns} \approx 200$ photons per bunch (see Eq. (3.11)).

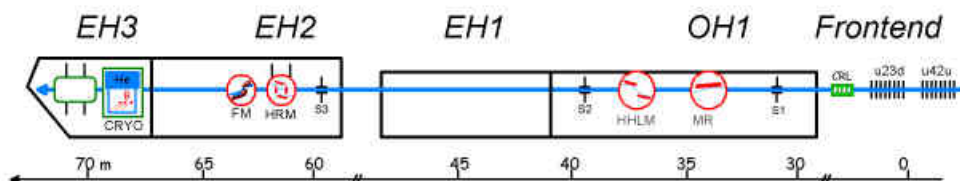


Figure 3.6.: Beamline ID22N of the nuclear resonance group at ESRF. The optics consist from right to left of compound refractive lenses (CRL), a pre-mirror (MR), a high heat load monochromator (HHLM), a high resolution monochromator (HRM) and focusing set-up (FM) [Rüffer and Chumakov, 2012].

The most important elements of the beamline are listed below.

Undulators The X-ray source comprises an undulator in vacuum of length 2 m, a period of 23 mm and a minimum gap of 6 mm, and a standard undulator segment of length 1.65 m, a period of 42 mm and a minimum gap of 16 mm. Unfortunately neither of the undulators is optimized for 14.4 keV. Due to the multi-purpose orientation this beamline puts out more than an order of magnitude lower intensity than ID18 at the ^{57}Fe resonance energy of 14.4 keV. Thus measurements at ID18 could profit from higher intensity and therefore better statistics.

Compound refractive lenses (CRL) The relatively small vertical beam size permits focussing with a fixed focal spot. The main advantage of CRLs is the simplicity in production and therefore high customisability. In general the index of refraction for X-ray can be described by $n = 1 - \delta + i\beta$ with $\delta, \beta \geq 0$. On the one hand, the smaller than unity refractive index demands focusing lenses of concave shape, and on the other hand the focussing effect of one lens is very small $\delta \ll 1$. Both conditions can be met by a series of consecutive holes in a compound rod. The focal length l_f can be easily adjusted by the radius of the holes R , but mainly by the number of holes N as

$$l_f = \frac{R}{2N\delta}. \quad (3.9)$$

The compound material should have a small atomic number, but a high density, i.e. Be, Al, to ensure high refraction but low absorption. Such a device makes it possible to have a beam size of $\sim 100 \mu\text{m}$ in the vertical direction.

Pre-mirror (MR) This horizontal deflection mirror significantly reduces the heat-load by pre-collimating and pre-monochromatizing the beam. Additionally it rejects other harmonics also reducing the load on the HHLM. Otherwise the HHLM can not be operated sufficiently stable.

High heat load monochromator (HHLM) This kind of monochromator consists of two separate Si (110) crystals on uncoupled positioning elements. The demand of a fixed exit (non-dispersive) beam is met by the first crystal mounted on a stage for horizontal translation. The purpose of the second crystal lies in defining a narrow energy resolution of $\sim 3 \text{ eV}$ at the ^{57}Fe resonance of 14.412 keV, because of its better stability due to significantly less heat load. The positioning devices are selected for high resolution (100 nrad) and stability ($1 \mu\text{rad month}^{-1}$) in angular movement. To inhibit temperature expansion the crystals are cooled by liquid N_2 , and as a consequence operated under at UHV conditions of $< 10^{-7}$ mbar.

High resolution monochromator (HRM) In our setup the monochromator consists of two “nested” channel-cut crystals in a four-bounce-nested design. Combining Si (333) as the inner crystal and Si (975) as the other one an energy resolution of 3.1 meV and a flux of $1.4 \times 10^9 \text{ s}^{-1}$ can be achieved for the resonance energy

of 14.412 keV at ID18, with a storage current of 90 mA typical for 16-bunch mode. As mentioned above in the undulator description the intensity at beamline ID22N is expected to be about one order of magnitude lower.

Avalanche photo diode (APD) In the semiconductor the incoming photons are converted to electron-hole pairs which move to opposite directions under an applied electric field. At a sufficiently high field the moving charge carriers can free additional electrons through collisions. This so called avalanche effect is utilized to pre-amplify the current, thus reducing the signal-to-noise ratio. The APD's are stacked to improve detection efficiency. The main properties interesting for nuclear resonant scattering are

- good time resolution (0.1–1 ns)
- good detection efficiency (0.4 at 14.4 keV)
- low noise rate (0.02 photons s⁻¹)
- high linear dynamic range (10⁹)
- fast recovery from high intensity pulses

Electronics The detector signal is amplified and forwarded into a constant-fraction discriminator (CFD) to find the point in time of the signal. On the one hand the output is directly used for the electronic reflectivity counter. On the other hand it is fed into a second gated CFD to just forward the delayed nuclear reflectivity into a second counter. The gate is set by the bunch-clock of the storage ring itself. This periodic signal in time is also used to stop the time-amplitude converter (TAC), which is started by the signal of the second CFD. The intermediate step is required because the TAC cannot cope with the prompt electronic signal. The time dependence of the delayed counts is analysed by a subsequent analog-digital converter (ADC) and a multi-channel analyser (MCA).

Downstream of the HRM an additional CRL system of Be was mounted. The actual parameters at the start of the experiment were a vertical beam size of 120 μm for a Be lens with $N = 16$ holes and a FWHM of 3.4 meV. The distance between the sample and the detector was about 0.65 m. The overall delayed (resonant) intensity for this setup was 2000 s⁻¹. Of course for the angle resolved measurement this value was

further reduced to about 30 s^{-1} at the total reflection angle, and even less at angles above.

The delayed nuclear reflectivity for each scattering vector q is acquired over a time window of 170 ns after the X-ray illumination, which is roughly the time between two electron bunches in the 16-bunch mode ($N_b = 16$) of the synchrotron. The bunch separation time t can be easily calculated from the electron energy $E = 6 \text{ GeV}$ and the storage ring circumference $S = 844 \text{ m}$. The velocity for electrons with $mc^2 = 511 \text{ keV} \ll E$

$$E(v) = \frac{mc^2}{\sqrt{1 - v^2/c^2}} \Rightarrow v = c\sqrt{1 - \left(\frac{mc^2}{E}\right)^2} \approx c \quad (3.10)$$

is close to the speed of light in vacuum. Therefore we get for the bunch separation time t

$$t = \frac{S}{N_b c} = 176 \text{ ns} \quad (3.11)$$

ideal for the life time $\tau_0 = 141.11 \text{ ns}$ of the first excited state of the ^{57}Fe nucleus. In comparison the rms of the bunch length of 48 ps at 16-bunch mode is neglectable. However a reflected signal of the prompt (electronic) reflectivity in the detector cable can be visible in the reflected intensity and influence the results. In consideration of this effect the intensity is integrated starting at 15 ns to avoid any disturbance by the prompt signal due to the electronic reflectivity, which is orders of magnitude more intense. The measured nuclear reflectivities for successive annealing steps are illustrated in Fig. 4.1 (top) for the sample annealed at 698 K.

RESULTS

In this chapter the processing of the experimental data of the nuclear reflectivity is explained in detail. The first section deals with the dynamical scattering approach to the evaluation. From the fitted reflectivity curves I deduce a diffusion parameter, called diffusion progress. In the subsequent section I plot the diffusion progress versus the annealing time to retrieve the actual diffusion constant. In the final step an Arrhenius-type plot is employed to extract the activation energy for the fundamental diffusion jumps. The basic results are published in Gröstlinger, Rennhofer, Leitner, Partyka-Jankowska, Sepiol, Laenens, Planckaert, and Vantomme [2012], however, a more detailed description of the theoretical, experimental and computational background is given in this thesis.

4.1. Reflectivity fits

In this section a detailed recipe for how a diffusion parameter is obtained from a series of annealing steps with subsequent reflectivity measurements is given.

The calculation of the nuclear reflectivity was done with the aid of the program package CONUSS [Sturhahn and Gerdau, 1994]. An attempt to calculate the nuclear reflectivity from scratch was discarded after some speed tests. It was clear that much optimization would have to be done to get acceptable calculation times as our routines turned out to be orders of magnitude slower. Additionally CONUSS already includes parameter distributions, which would have additionally slowed our calculation time and would have required significant adaption of the code. The code to calculate nuclear

reflectivity for the grazing incidence geometry is provided in the Sec. B.5. It should give an easy access to the fundamental elements of the calculation, because the programming language PYTHON is close to pseudo-code and thus very readable. For heavy usage, however, its speed would need to be significantly improved by outsourcing the basic routines to compiled libraries, e.g., extensions in C are easily integrated.

For comparison with the experiment first the experimental data containing the angle range, and the electronic and nuclear reflectivity is loaded. As already outlined above the electronic reflectivity was utilized to gain as much information of the sample as possible, prior to the nuclear resonant fitting procedure. This was important as the calculation of the nuclear resonant reflectivity is significantly more time consuming in the order of 1 min than the electronic one ($\ll 1$ s), so less parameters mean less calculations of the reflectivity. In particular the overall thickness and the surface roughness of the film could be already extracted from the electronic reflectivity. Additionally the angular positions appeared to be randomly shifted throughout the experiment. This can, for one, be attributed to the free manual positioning of the samples on the sample holder without any mounting or to imprecise movement of the angular stepping motor. For this reason an arbitrary angle shift parameter was introduced for the electronic fits, which should correct the experimental imprecision. Naturally this correction applies to the nuclear reflectivity as well.

The experimental data slightly below the total nuclear reflection was removed as the calculation could not reproduce the slope of the curve in that part. Although an implementation of a superimposed function which corrects for the finite sample size with respect to the vertical beam extent in grazing incidence geometry altered the slope in the right direction, it was not enough to prevent influence on the results of the minimization.

Since the calculation of the nuclear reflectivity for as much as 100 layers is very time consuming even in CONUSS, I tried to utilize the full potential of multi-core processors. Incidentally a parameter in the source code had to be changed by R. Röhlberger, one of the authors of the program, to increase a hard-coded layer limit. The only way to realize parallelization without interfering with the code of the original program package was to split the angular range in parts, and calculate the corresponding intensities by the individual processors in their own subdirectories. Although this is not the most efficient way to do this, even for a dual-core processor the calculation time was cut

to about 60%. To simplify the calculation the experimental data was reduced to a multiple of the number of the processor cores, as the last few data points practically contained no essential information.

The squared deviation of the experimental with respect to the theoretical curve is minimized via a Downhill-Simplex algorithm by Nelder and Mead [1965]. This method does not rely on finite differences. As a consequence it is very stable and requires a relatively small amount of function evaluations per minimization step. Basically for 2 parameters, thus for a 2-dimensional parameter space, one can picture a triangle moving around on a hilly landscape. By mirroring its worst point, contracting or extending in one direction or contracting as a whole the algorithm tries to find the deepest valley (global minimum). Expanding to higher dimensions is trivial but to imagine it geometrically exceeds the human mind.

The squared deviation from the theoretical to the experimental value S is minimized with respect to the parameter vector \mathbf{p} . Of course initially an experienced guess has to be provided. Through extensive test calculations reasonable starting parameters could be found that yielded a reasonable best estimator once converged. Lower \mathbf{p}_- and upper bounds \mathbf{p}_+ were provided to avoid unphysical or redundant results, e.g., negative thicknesses and times or angles below 0 and above 2π

$$\min_{\mathbf{p}_- < \mathbf{p} < \mathbf{p}_+} \frac{1}{N} \sum_{i=1}^N (f(\mathbf{p}, x_i) - y_i)^2 . \quad (4.1)$$

Note that the normalization to the actual number of data points N is important since the CONUSS software sometimes yielded invalid numbers for the resulting nuclear intensity at seemingly random scattering angles most certainly originating from numerical errors. Had this not been compensated for by that factor, certain parameter sets with the least successfully calculated reflectivities points would be strongly favoured. This is only an approximate correction as data points with higher intensities would contribute stronger, but luckily as shown in the figures of the final reflectivities these discontinuities appeared mostly in unimportant regions. The weighting was chosen to be the same in absolutes, as this configuration yielded the most reasonable fits to the experimental data.

The parameters possibly influencing the calculated nuclear reflectivity points are listed below including a short description on the actual usage.

Angle shift This parameter was introduced to correct for random overall shifts of the angular positioning and was already known from electronic reflectivity.

Nuclear intensity factor The overall intensity factor was fitted to correct for different accumulation times and a slight instability of the high resolution monochromator, changing the nuclear reflected intensity independently from the electronic one. Additionally the decrease of the electron flux in the storage ring, and subsequently the photon flux, ring is accounted for.

Double layer thickness The thickness for one double layer period calculated from the number of double layers and the overall thickness resulting from the electronic reflectivity fit.

Enriched layer thickness The thickness of the enriched layers was scaled from the double layer thickness by the original thickness ratio of $2 \text{ nm}/(2 \text{ nm}+3 \text{ nm}) = 2/5$.

Mass density The mass density of the FePt-film is calculated from the lattice parameters a and c extracted from XRD

$$\rho = \frac{Nm_{\text{atu}} \sum_i \alpha_i m_i}{a^2 c} = 13.80 \times 10^3 \text{ kg m}^{-3} \quad (4.2)$$

with the number of atoms in the unit cell $N = 4$, the atomic mass unit $m_{\text{atu}} = 1.66054 \times 10^{-24} \text{ g}$, the fractions α_i , known from Rutherford backscattering, and the relative masses m_i of the respective elements.

Beam size The approximate vertical beam extent is in our case roughly $s_b \approx 100 \mu\text{m}$.

Sample size The size of the sample ($s_s = 1 \text{ cm}$) is used in combination with the vertical beam size to calculate a geometry function g

$$g(\theta) = \min \left\{ \frac{s_s}{s_b} \cos(\pi/2 - \theta), 1 \right\} \quad (4.3)$$

correcting for the beam overshooting the sample in grazing incidence at low angles.

Diffusion progress The diffusion progress Dt is the key parameter used for the subsequent evaluation. The diffusion parameter D assumed constant for a certain annealing temperature is extracted utilizing the known annealing time t .

Roughness of the surface This parameter is also obtained from electronic reflectivity fits. It mainly smears the intensity undulations and causes faster decrease of the intensity for increasing scattering angle. For our samples I found a average value of 0.5 nm.

Time integration start Because of the orders of magnitude more intense prompt signal, the detector cannot collect the nuclear resonant events right from the start, due to overload. If we look at the resonantly reflected intensity at a certain angle, the intensity decreases roughly exponentially in time. Thus in the time-integrated intensity the part with the highest intensities is missing. Therefore this effect strongly decreases the intensity at every angle. The question now is, if it is the same factor for every angle [Andreeva et al., 2008] and what is the best-fitting value for the time between the prompt signal and the start of the nuclear intensity integration. Reasonable starting times between 0 ns and 25 ns were tested and yielded similar results for the diffusion progress Dt within the margin of error. At extreme values of the time integration start the reflectivity changed significantly but our experimental setup is situated far from that. I concluded that, at least in our case, there is no significant influence to our evaluation and chose $t_{\text{start}} = 15$ ns as this is assumed a good fit to the experimental reality. So in our case the parameter mainly decreases the overall nuclear reflected intensity.

Half-life of the ^{57}Fe isotope The half-life of the nuclear excited state also defines the width of the resonance line in the energy domain. This parameter could also be used to simulate small electric or magnetic distributions in the sample. I use the natural half-life $T_{1/2} = \tau_0 \ln 2 = 97.81$, were $\tau_0 = 141.11$ ns is the natural life time.

Weight of the site The weight of the 3 possible domains are extracted from the CEMS measurements, which have been roughly confirmed by the XRD measurements. Since I only have to distinguish between two inequivalent orientations and the normalization condition holds, a single weighting parameter w needs to be introduced. In my case I chose the weight of the canted domain with the component in a -direction.

Magnetic field modulus The modulus of the magnetic field was also taken from CEMS. The small difference in the magnetic field for the domain with the smallest

fraction to the one with equivalent orientation was neglected.

Magnetic field distribution width (see above and CEMS)

Magnetic field azimuthal (see above and CEMS)

Magnetic field polar angle (see above and CEMS)

For the calculation of the nuclear reflectivity first the sample has to be defined according to the diffusion state. The initial concentration variation is assumed perfect step-like. The minimum enrichment of ^{57}Fe is given by the natural abundance of 2%, whereas the maximum concentration is given by the enrichment in the evaporated material. The Neumann boundary condition is met by mirroring the concentration profile on one side. For the first evaluation a typical diffusion progress Dt is chosen to calculate a typical depth-dependent concentration. As mentioned in Sec. 2.1.1 the solution of the diffusion equation for this 1-dimensional problem is obtained by convolution via Fourier transform (FFT). In our case the fundamental solution is a sum of the individual basic fundamental solutions weighted by their fraction in the samples, deduced from CEMS. Since the FFT assumes a periodic function to begin with the boundary condition is met by this definition and the mirroring of the concentration earlier.

This concentration is discretized into a sufficient number of equidistant homogeneous sublayers, in our case $N = 100$. The discretization is optimized by slowly moving the interfaces to find a minimum of the squared deviation to the more fine-grained solution of the diffusion equation. As a result the interface density is higher at higher concentration gradients.

At this point parameter files for the CONUSS-software are written to calculate the nuclear reflectivity from N layers on a MgO-substrate of infinite thickness. The resulting squared deviation to the experimental data is minimized with respect to the free parameters. For this purpose for a certain parameter set the steps from above are repeated, to recap the diffused concentration profile and subsequently its nuclear reflectivity is calculated. For the final reflectivity fits the parameters set could be reduced to just the diffusion progress and the nuclear intensity factor. The minimization converged at an average of 30 simplex steps.

This procedure is repeated for every sample. The fits established in this way are drawn in Fig. 4.1, Fig. 4.2 and Fig. 4.3 for the samples annealed at 673 K, 698 K, 653 K, 723 K and 743 K, respectively. The diminishing nuclear Bragg peak clearly

corresponds to the decrease of the variation of the tracer enrichment in the sample. The higher frequency undulation stems from the overall film thickness and does not change due to isotopic diffusion. From the slight deviation of the experimental data one can conclude that there is, however, some sort of composition imperfection of the samples which could not be resolved by our model.

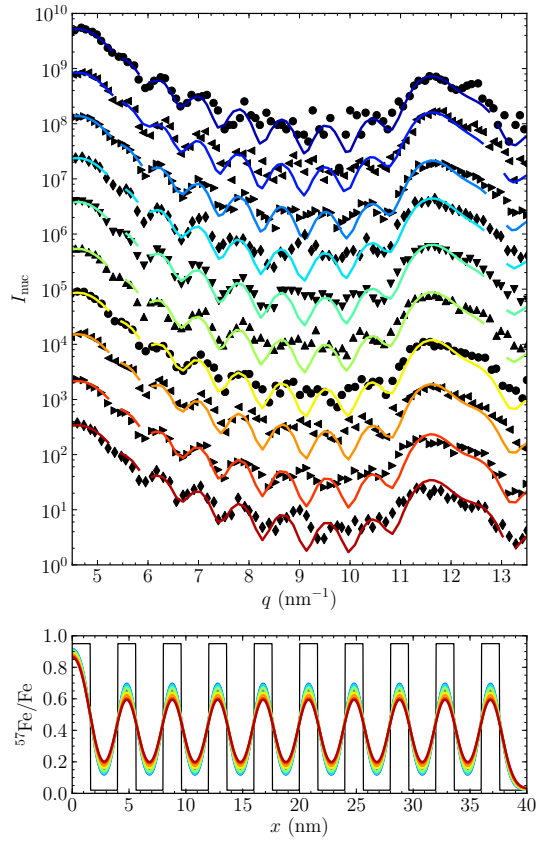


Figure 4.1.: Nuclear resonant reflectivity I_{nuc} for the $^{57}\text{FePt}/\text{FePt}$ multilayer at 678 K versus scattering vector q for increasing annealing time from top to bottom. The data was shifted for better visibility (filled black). The colored lines are the calculated dynamical nuclear reflectivities corresponding to the discretized solutions of the diffusion equation for the enrichment of ^{57}Fe in depth x of the film as seen below.

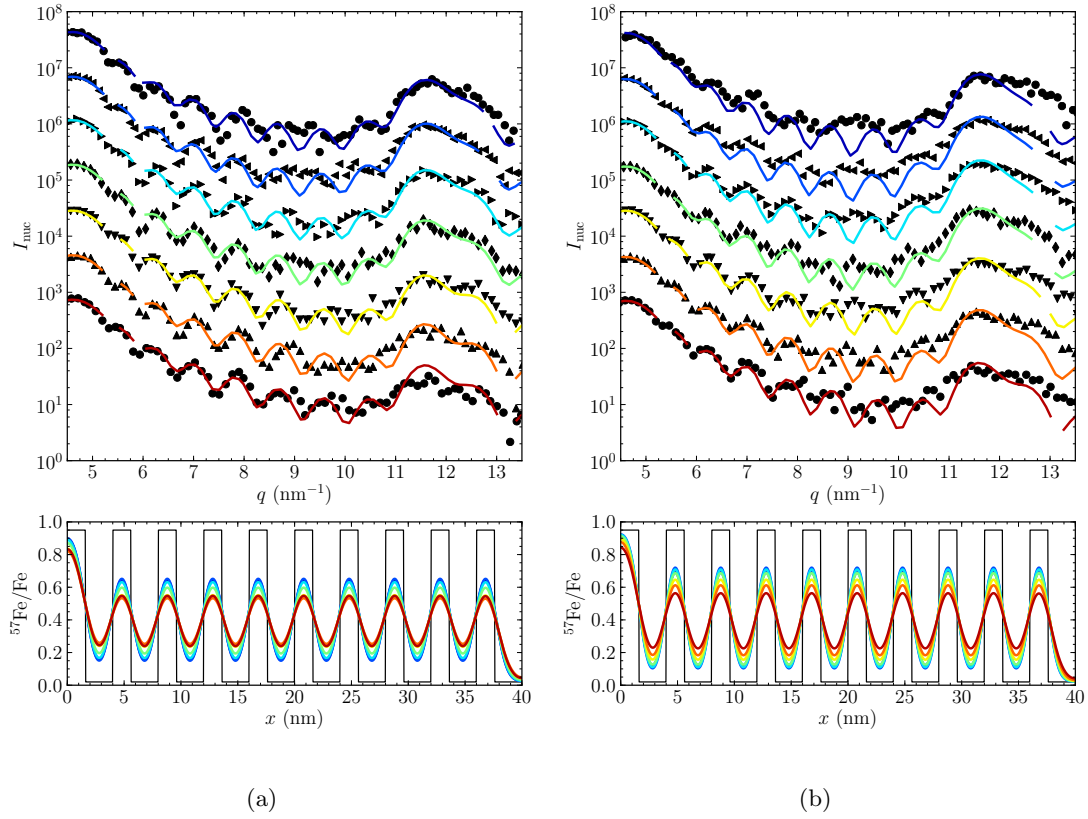


Figure 4.2.: Nuclear resonant reflectivity I_{nuc} for the $^{57}\text{FePt}/\text{FePt}$ multilayer at (a) 698 K and (b) 653 K versus scattering vector q for increasing annealing time from top to bottom. The data was shifted for better visibility (filled black). The colored lines are the calculated dynamical nuclear reflectivities corresponding to the discretized solutions of the diffusion equation for the enrichment of ^{57}Fe in depth x of the film as seen below.

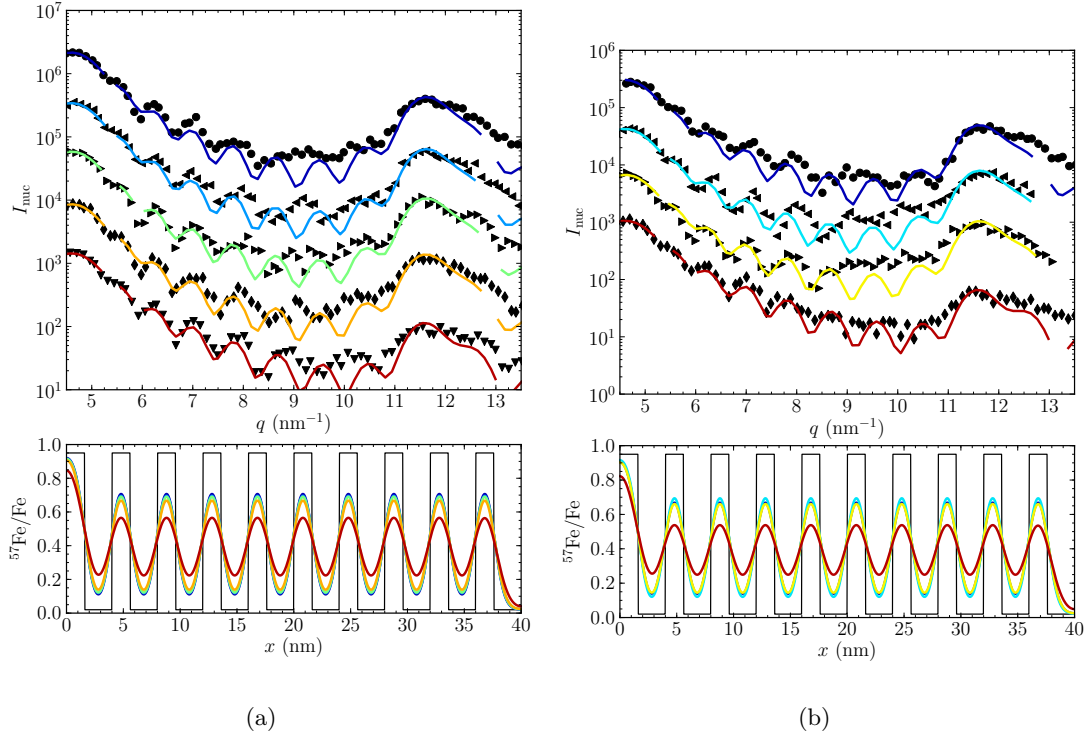


Figure 4.3.: Nuclear resonant reflectivity I_{nuc} for the $^{57}\text{FePt}/\text{FePt}$ multilayer at (a) 723 K and (b) 743 K versus scattering vector q for increasing annealing time from top to bottom. The data was shifted for better visibility (filled black). The colored lines are the calculated dynamical nuclear reflectivities corresponding to the discretized solutions of the diffusion equation for the enrichment of ^{57}Fe in depth x of the film as seen below.

4.2. Diffusion coefficients

For the extraction of the diffusion constant D from the diffusion progress resulting from the plots above the latter is plotted versus the time duration of the annealing t for a certain temperature, shown in Fig. 4.4.

For the dynamical evaluation the slope of a straight line fitted to the data in this representation is the diffusion constant D . Because of the elevated temperature and enhanced mobility in the vicinity of the surface during sample preparation, the initial composition is not perfectly step-like. The initial state of the samples should be the same as they are cut from one large homogeneous sample, therefore I require the intersection of all the fitted lines at the ordinate. In our case this joint initial diffusion progress is $Dt_0 = 0.3787 \text{ nm}^2$. In this way I gain additional information about the initial state of the sample with respect to the conventional evaluation. The resulting values for the linearly fitted diffusion constant D_{dyn} are listed in Tab. 4.1.

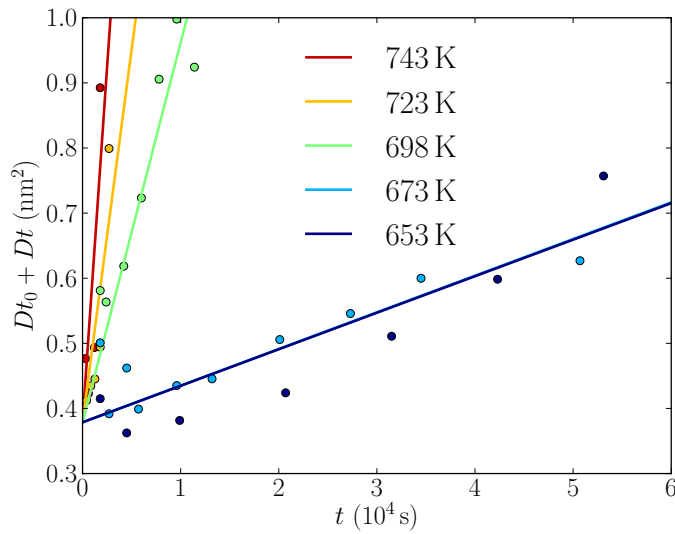


Figure 4.4.: The fitted diffusion progress Dt plotted versus the anneal time for all temperatures together with a linear fit. Hence the slope of the fitted lines provides the diffusion constant.

For comparison with the diffusion constant obtained from the kinematical approach the logarithmic relative intensities are plotted versus the annealing time t shown in

Table 4.1.: Total annealing time t and diffusion constants for kinematical D_{kin} and dynamical evaluation D_{dyn} for different annealing temperatures T . The samples are ordered by increasing temperature and the total annealing time t is the sum of the individual annealing durations of Tab. 3.3.

sample	T (K)	t (10^3 s)	D_{kin} (10^{-22} m 2 s $^{-1}$)	D_{dyn} (10^{-22} m 2 s $^{-1}$)
T4	653	53.1	0.064(10)	0.056(11)
T2	673	50.7	0.060(9)	0.056(12)
T3	698	11.4	0.505(38)	0.583(47)
T6	723	2.7	1.65(35)	1.14(23)
T8	743	1.8	2.79(80)	2.18(36)

Fig. 4.5. As we know from Sec. 2.3 the relation of the logarithmic relative intensity to the diffusion or annealing time is no longer strictly linear. The experimental data is fitted by the earlier established Eq. (2.46) employing a Levenberg-Marquardt minimization weighting the individual data points of $\ln(I/I_0)$ by the propagated squared standard deviation of $\sigma^2 = (\sigma_I/I)^2 + (\sigma_{I_0}/I_0)^2 = 1/I + 1/I_0$.

In the special case of a tetragonal structure two distinguishable orientations have to be accounted for. Therefore two spatially separated sorts of atoms diffusing in different environments with the fractions $w_1 = w$ and $w_2 = 1 - w$, respectively, and the normalization condition $0 \leq w \leq 1$, have separate solutions of the diffusion equation. However the resulting scattered intensity has to be a weighted sum of both types of domains. At this point I already presume the diffusion constant in the a direction to be much larger than the one in the previously measured c direction $D_a \gg D_c$. This is based on the geometry of the lattice where alternating planes of atoms act as diffusion barriers for the respective other kind. Eq. (2.36) can then be approximated by $D = D_a/2 + D_c/2 \approx D_a/2 \equiv D_1$, and furthermore I define $D_2 \equiv fD = D_a$. Finally I can write Eq. 2.46 in a more similar way to Eq. (2.43)

$$\begin{aligned}
 \ln \frac{I(t, q)}{I(0, q)} &= 2 \ln \left(w e^{-q^2 D t} + (1 - w) e^{-q^2 f D t} \right) \\
 &= -2q^2 D t + 2 \ln \left(w + (1 - w) e^{-q^2 (f-1) D t} \right) \\
 &= -2q^2 D t + 2 \ln \left(w + (1 - w) e^{-q^2 D t} \right), \tag{4.4}
 \end{aligned}$$

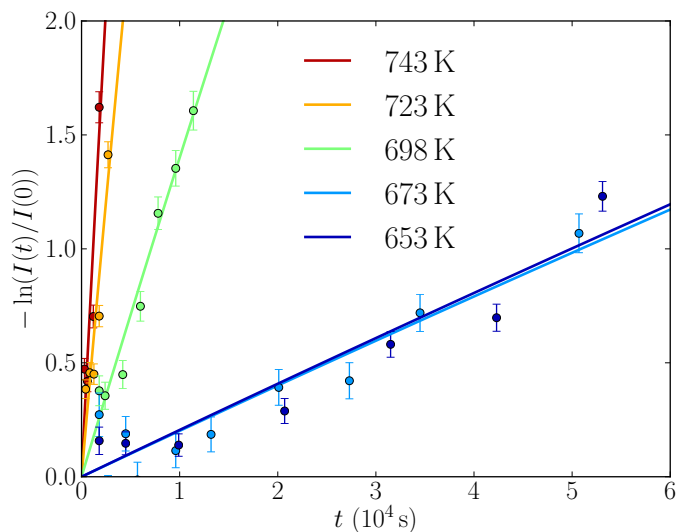


Figure 4.5.: The logarithmic relative intensity plotted versus the annealing time t . The data is fitted by the adapted kinematic relation of Eq. 4.4.

For $w \rightarrow 1$ the latter converges to the original Eq. (2.43) as it should. In the contrary for $w \rightarrow 0$ the diffusion constant of the second family of domains is dominating. For very large times $t \rightarrow \infty$ and a sufficiently small fraction of misoriented domains $1 - w \ll 1$ the correction factor becomes an additive constant.

As already mentioned Eq. (4.4) is no longer linear in time t , thus a Levenberg-Marquardt algorithm is used to extract the diffusion constants D_i . Employing the knowledge of the CEMS and XRD measurements about the fractions and orientations of the domains, the effective diffusion in the a -direction can be derived this way. The resulting diffusion constants, denoted D_{kin} , are also available in Tab. 4.1. Note that in this case the diffusion constant of the second lowest temperature is even lower than the one of the lowest temperature. This experimental inaccuracy, however, is automatically corrected in the right direction for the dynamical evaluation due to the additional information about the initial state of the samples.

4.3. Activation energy

Most thermally activated kinetic processes satisfy in a good approximation the Arrhenius relation [Arrhenius, 1889]

$$D(T) = D_0 e^{-E_a/k_B T} \quad (4.5)$$

with the Boltzmann constant k_B , the temperature T and the activation energy E_a . The prefactor D_0 is the rate of attempted reactions, in our case diffusion jumps, and the exponential factor can be viewed as the probability that the attempted reaction succeeds. For this purpose a certain potential barrier has to be overcome by the reactants, which is proportional to the activation energy. Quite naturally the reaction rate increases with increasing temperature or decreasing activation energy. Note that for this equation to be valid the activation energy has to be assumed constant. While this may be true for most relevant temperature ranges, we will see later in the discussion that the interpolation to temperatures far from the actual measurement may not necessarily agree with studies at these conditions.

Strictly speaking this is a pure empirical relation, however, there are several approaches to justify it from a microscopic theory. In the most simple picture of statistical mechanics I can argue that the fraction of reactants, fulfilling the Boltzmann distribution, with an energy above the activation energy is proportional to the Arrhenius exponential. The other main interpretations are based on collision theory [Trautz, 1916] and transition state theory [Pelzer and Wigner, 1932; Eyring, 1935].

The downside of this characteristic energy E_a is its macroscopic nature. It represents the sum over a large number of processes in a solid, maybe even consisting of several different subprocesses. Thus one cannot directly relate the activation energy to a single fundamental atomic process. However the activation energy can supply a good point of reference for the total energy necessary to complete the dominant microscopic reaction in a certain temperature range. Furthermore quite often the prefactor has an additional temperature dependence, which is, however, often neglectable in the relevant temperature range.

It is commonly established that diffusion in solids widely obeys the Arrhenius relation. So to finally find the temperature dependence of the diffusion process the diffusion constant is plotted versus the inverse temperature in Fig. 4.6. Additionally I compare the dynamical evaluation to the conventional kinematical evaluation along the same

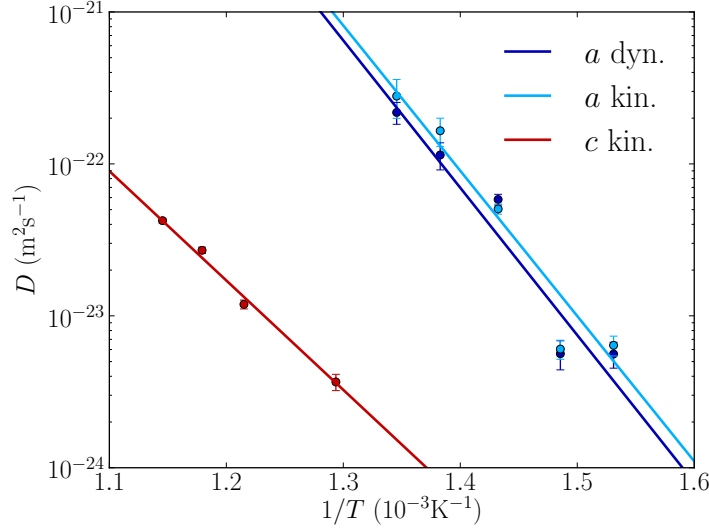


Figure 4.6.: Diffusion constant D versus inverse temperature T for c -direction [Rennhofer et al., 2006] and a -direction, evaluated by kinematical and dynamical scattering theory, respectively. The slope represents the activation energy of diffusion.

direction and the diffusivity in the perpendicular direction. The resulting activation energies (pre-factors) for the kinematical and dynamical evaluation are 1.90(23) eV ($8.4 \times 10^{-9} \text{ m}^2\text{s}^{-1}$) and 1.92(23) eV ($2.6 \times 10^{-9} \text{ m}^2\text{s}^{-1}$), respectively, are slightly higher than the activation energy in the perpendicular direction previously measured. The kinematical evaluation is in good agreement with the dynamical evaluation. The diffusion constant in a -direction is nearly two orders of magnitude faster than in c -direction. This huge difference justifies the previously taken assumption for the kinematical evaluation of the diffusion. More details about the interpretation will be given in the next chapter.

DISCUSSION

5.1. Effective formation energy

The raw formation energies of Sui et al. [2007] based on ab-initio calculations for Fe (Pt) antisites and vacancies are $\epsilon_{\text{Fe}}^{\pi} = 1.05$ eV ($\epsilon_{\text{Pt}}^{\phi} = 0.66$ eV) and $\epsilon_{\text{V}}^{\phi} = 2.58$ eV ($\epsilon_{\text{V}}^{\pi} = 3.2$ eV), respectively, where I denote the Fe- and Pt-sublattice by ϕ and π , respectively. In contrary to the valid approach of inserting the excess atom at a typical surface site, in ab-initio calculations with periodic boundary conditions this is not possible. In an elementary lattice the missing energy of the removed atom would be compensated by correcting with the difference between the energy of the relaxed lattice with the vacancy and the normalized energy of the relaxed perfect lattice. The resulting entity is then the vacancy formation energy in a canonical formalism and the concentration is of the form of $c_{\text{V}} = e^{-E_{\text{V}}/k_{\text{B}}T}$. In a structure with multiple sublattices, however, it is not possible to separate the contribution of the individual atoms in a physical meaningful sense this way, because one can only define an energy per unit cell. In this case the Gibbs free energy $G = U - TS + pV$ has to be minimized in a grand canonical formalism with respect to the numbers of the individual defects N_i

$$\partial_{N_i} (U - TS + pV - \mu_{\text{Fe}} N_{\text{Fe}} - \mu_{\text{Pt}} N_{\text{Pt}}) = 0, \quad N_i = N_{\text{V}}^{\phi}, N_{\text{V}}^{\pi}, N_{\text{Pt}}^{\phi}, N_{\text{Fe}}^{\pi}. \quad (5.1)$$

This framework allows now for atoms to be removed or added to the structure without neglecting their contribution to the total energy. Now the defect concentrations, however, have a much more complicated form. Here the concentration and the other

properties of one defect depend on the thermodynamic quantities of the other defects as well [Mayer et al., 1995; Mayer and Fähnle, 1997]. Only in the limit of total stoichiometry and thus predominant thermal defects or the off-stoichiometric case with a majority of constitutional defects the concentrations reduce to a form similar to the canonical formalism above. The respective effective formation energies are adapted to yield again an exponential relation for the defect concentrations [Meyer and Fähnle, 1999]. Otherwise all defects interact and the complexity of the problem increases significantly.

In our case clearly antisites are the preferred structural point defects as we can see from the calculated formation energies above. In a simple sense only combined defects conserving the composition of the lattice have physical meaning. The fundamental defect configurations, also depicted in Fig. 5.1, are

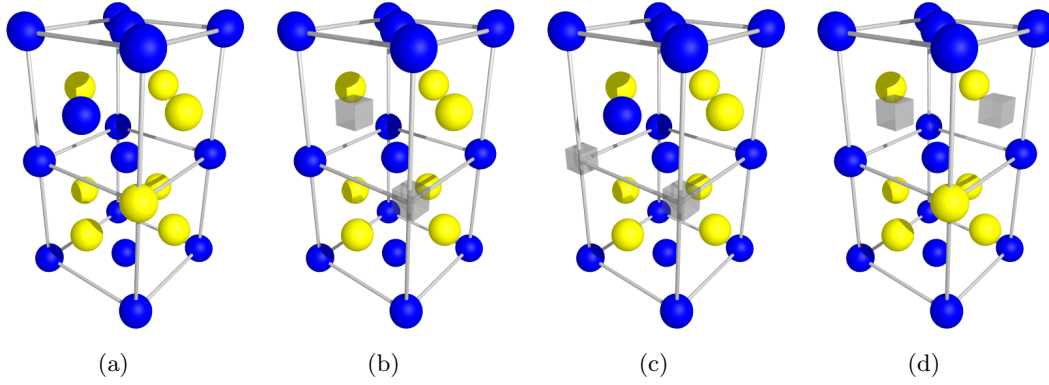


Figure 5.1.: The fundamental defects, allowing only for antisites and vacancies, are (a) antisite pair, (b) vacancy pair, (c) Fe triple defect and (d) Pt triple defect. All higher order defects are linear combinations of the ones depicted here.

$$\epsilon_{\text{Pt}}^{\phi} + \epsilon_{\text{Fe}}^{\pi} = 1.71 \text{ eV} \quad (\text{antisite pair}), \quad (5.2)$$

$$\epsilon_{\text{V}}^{\phi} + \epsilon_{\text{V}}^{\pi} = 5.78 \text{ eV} \quad (\text{Schottky defect}), \quad (5.3)$$

$$\epsilon_{\text{Fe}}^{\pi} + 2\epsilon_{\text{V}}^{\phi} = 6.21 \text{ eV} \quad (\text{Fe triple defect}), \quad (5.4)$$

$$\epsilon_{\text{Pt}}^{\phi} + 2\epsilon_{\text{V}}^{\pi} = 7.06 \text{ eV} \quad (\text{Pt triple defect}). \quad (5.5)$$

Here the energy of the undisturbed crystal, independent of its size, is set to vanish. Thus the energy of a vacancy pair increasing the crystal by a complete cell is just the

energy of the two individual vacancies. The same is true for the other defects.

In reality only 3 of those 4 equations are linear independent. Therefore there can only be 3 independent energy parameters. Since in my case I have excess Fe atoms and antisites have much lower activation energies than vacancies, Fe-antisites are chosen to be the preferred structural defect and set to $E_{\text{Fe}}^{\pi} = 0$ eV, if I assume that thermal defects can be neglected compared to the former ones. Note that in case of total stoichiometry two defects will have to be set to the same energy. Furthermore we get

$$E_{\text{Pt}}^{\phi} = \epsilon_{\text{Pt}}^{\phi} + \epsilon_{\text{Fe}}^{\pi} \quad (5.6)$$

$$E_{\text{V}}^{\phi} = \epsilon_{\text{V}}^{\phi} + \epsilon_{\text{Fe}}^{\pi}/2 \quad (5.7)$$

$$E_{\text{V}}^{\pi} = \epsilon_{\text{V}}^{\pi} - \epsilon_{\text{Fe}}^{\pi}/2 \quad (5.8)$$

These equations can also be found in Meyer and Fähnle [1999]. The resulting effective formation energies for the complementary Pt-antisite and the vacancies are, $E_{\text{Pt}}^{\phi} = 1.71$ eV, $E_{\text{V}}^{\phi} = 3.105$ eV and $E_{\text{V}}^{\pi} = 2.675$ eV. Now these new values for the formation energies will reproduce the right thermodynamics. Clearly this has to be seen as a first approximation, as for a serious investigation of the energetics all the interactions between the defects may have to be considered.

5.2. Energetics

The difference in the activation energies for the kinematical and dynamical evaluation, 1.90(23) eV and 1.92(23) eV, is negligible and well in the range of the standard deviation. Therefore I can basically confirm the results of the kinematic evaluation. Additionally, the diffusion constants are only about 20% lower for the dynamical evaluation in the range examined here. Interestingly the activation energies are in the same region as the previously measured value of 1.65(29) eV, corresponding to the perpendicular direction.

These values for the activation energy are lower compared to Fe-tracer [Nose et al., 2005; Nakajima et al., 2005] or chemical [Kushida et al., 2003] diffusion data in FePt obtained, however, at much higher temperatures. Lower activation energies may be explained by grain boundary diffusion with a high concentration of point defects [Lee et al., 2005]. Due to the probed length scales, which are barely an order of magnitude above the lattice constant, only an extremely high density of such defects would be able to influence the diffusivities measured with our method, which is in noted

contrast to the case of conventional tracer diffusion experiments. The high epitaxial quality of our samples is furthermore confirmed by the TEM images of Sec. 3.1.6 [Laenens et al., 2009] for the c -variant samples, revealing anti-phase boundaries and dislocations mainly at the interface to the substrate. Furthermore I would like to note that the dislocation lines are parallel to the substrate surface. This would mean that any enhanced diffusion paths resulting from these dislocations do not contribute to the perpendicularly measured diffusion. Additionally the activation energies of the c -variant 1.65(29) eV [Rennhofer et al., 2006] and the here investigated direction are in good agreement. So if I get a similar or even slightly higher activation energy for diffusion in our samples with different orientation I would argue that the sample quality should be comparable to what we observe here. Thus I take the high epitaxial quality demonstrated earlier as an argument also for our samples.

The rather low activation energy is also confirmed by in-situ resistometry measurements on a similar FePt isotopic multilayer by Kozubski et al. [2005]. Additionally, they observed a similar multiscale character of the activation energies in order-order transitions investigated by Monte Carlo simulations.

To recapitulate, I believe that the activation energy in our measurements on two different samples so far and in different crystallographic directions has experimentally a solid base. New tracer or interdiffusion measurements filling the huge gap in the temperature between our data and data of Nose et al. [2005] would therefore be desirable.

5.3. Anisotropy

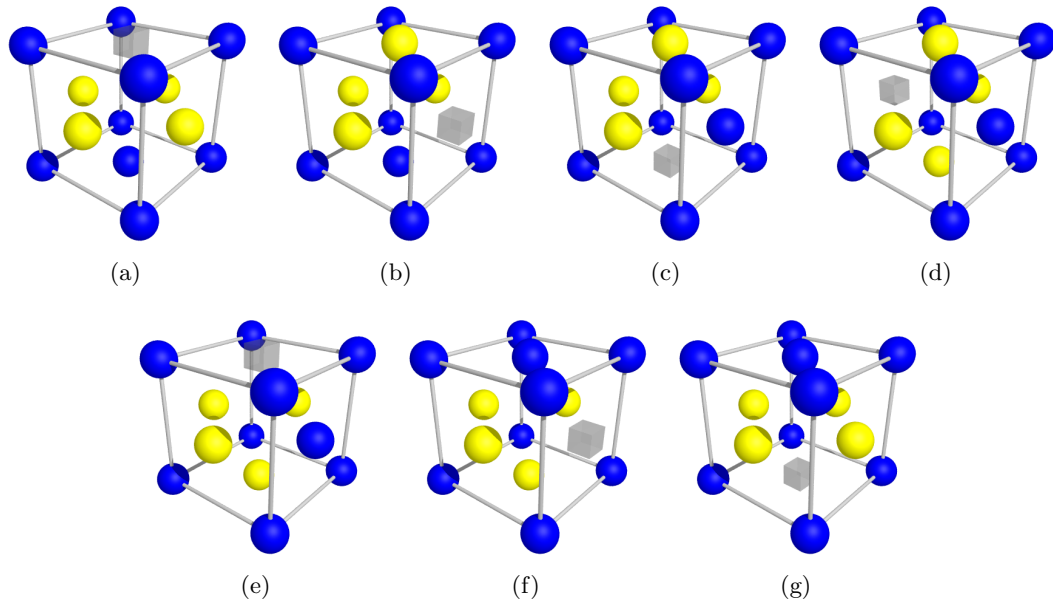
The up to two orders of magnitude enhanced Fe diffusion rate parallel to the a -plane compared to the diffusion rate along the c -axis qualitatively confirms the expectation of diffusion mainly in the Fe sublattice. However, the anisotropy is surprisingly high compared with other intermetallics of the same structure.

Anisotropic diffusion measurements are anyway very rare for $L1_0$ single crystals. Studies on $L1_0$ -FePt (0.54 atomic fraction Fe close to the fraction of 0.56 of our sample) report an anisotropy of only 1.2 to 1.7, i.e. faster iron diffusion along the a - than along the c -axis [Nose et al., 2005; Nakajima et al., 2005]. This value only slightly increases to the factor of 1.6 to 3.6 in the Pt-rich composition with 0.42 atomic fraction of Fe. According to the difference in the activation energy found there, the gap in

the diffusivities should be much higher at the significantly lower temperatures of our measurement. I attribute this to the high uncertainty of the activation energies resulting in ambiguous predictions in different thermal ranges. The anisotropy of Ti-diffusion in L1₀-TiAl is one order of magnitude [Ikeda et al., 2001; Mishin et al., 2005]. Anisotropies of impurity diffusion in TiAl [Nose et al., 2006] can be larger as well as smaller than one, which proves that activation energies play a crucial role in the case of impurities.

For perfect stoichiometry I assume that any Fe diffusion in *c*-direction will require higher energy due to the creation of Pt-antisites, therefore the energetically favoured diffusion paths are exclusively in the *a*-planes. The raw formation enthalpies from ab-initio calculations [Sui et al., 2007] for Fe (Pt) antisites and vacancies, 1.05 eV (0.66 eV) and 2.58 eV (3.2 eV), respectively, can be renormalized for structural antisites [Meyer and Fähnle, 1999] in the Fe-rich composition to the effective formation enthalpies of 0 eV (1.71 eV) and 3.105 eV (2.675 eV), respectively, to achieve the right kinetics as shown in Sec. 5.1. For diffusion in *c*-direction diffusion paths via the classical six-jump cycle [Elcock and McCombie, 1958] (see also Mehrer [2007]), visualized in Fig. 5.3, or direct jumps to a next-nearest neighbour site are both energetically disadvantageous. The very high order of the FePt phase clearly supports this view.

In our slightly off-stoichiometric Fe-rich samples a small fraction of diffusion paths of similar energetics to the *a*-planes through structural Fe-antisites exist. The vacancies could migrate through these defects without creating additional ones. Actually the vacancy formation energy on the Pt-sublattice is even lower than on Fe possibly attracting vacancies from Fe-sites. This way the very similar activation energy in both direction is comprehensible. The reason for the high anisotropy in the diffusivities, however, is in our opinion the far higher number of energetically favoured diffusion paths on the Fe's own sublattice. The lower observed activation energies could be explained by interaction of the different kinds of defects, briefly discussed in Sec. 5.1, or a lattice constant deviating from the relaxed due to the epitaxial nature of the films. Additional diffusion paths through Fe anti-sites would mainly influence the diffusion in *c*-direction which was measured on samples closer to stoichiometry. Despite their far lower numbers the good agreement of the activation energy in the different directions suggests that the diffusion in *c*-direction similarly occurs through antisites on the Pt-sublattice, nonetheless. From these considerations I expect even higher anisotropy for Pt. Overall, the presence of antisites could decrease the formation energy of vacancies

Figure 5.2.: Six-jump cycle in $L1_0$ -structure

considerably and calls for further ab-initio calculations. In general this shows that the diffusion mechanism can be strongly influenced by structural defects. It is commonly overlooked that for defect formation energies larger than 1 eV there are almost always much more constitutional than thermal defects at reasonable temperatures demanding the non-stoichiometric limit.

Another perspective of viewing diffusion over energetically favoured diffusion paths is a correlation effect for the vacancy jump as a diffusion vehicle. In the paper of Ikeda et al. [2001] the smaller diffusion coefficient of Ti in the direction parallel to the c -axis was explained in terms of the stronger correlation effect for vacancy jumps between sublattices. This claim was modified in the later paper Nakajima et al. [2005] but certainly some part of the anisotropy could also be understood by taking only vacancy correlation effects into account.

In summary anisotropy of iron diffusion in $L1_0$ -FePt is a result of energetic barriers and vacancy correlations. I can, however, not separate the relative impacts of all these factors.

5.4. Conclusion

In summary, the activation energies are very similar suggesting a vacancy-driven diffusion mechanism in both directions. In the direction perpendicular to the element-wise alternating atomic planes this mechanism is enabled by structural antisites. The high anisotropy is thus mainly attributed to the higher number of favourable diffusion paths within the said planes. Additionally I found that it is of major importance to consider the interactions between the different kind of defects.

Taking into account all these factors, we have seen that L1₀-FePt displays the highest anisotropy of the diffusion coefficient in the c - versus perpendicular to the c -axis among all L1₀-systems reported so far. The results are published in Gröstlinger et al. [2012]. However, I cannot argue with absolute certainty which factor is the most important and leave this problem as a challenge for future ab-initio calculations.

A full dynamical treatment for multilayer diffusion incorporating all the hyperfine parameters was employed to a real resonant reflectivity experiment. Within the variance the results are in good agreement to the classical evaluation method. In samples with a higher ratio of nuclear resonant absorption to photoabsorption, however, significant deviations can be seen. This problem is an interesting issue and could be an object of a distinct publication in the future.

Part II.

Atomic vibrations

CHAPTER 6

INTRODUCTION

6.1. Phonons

Atomic vibrations are determined by the properties of the surrounding electron density. The study of atomic dynamics, thus, provides an insight on the fundamental forces acting on the atomic scale. In this regard, investigations of the former provide information not only on the mechanical (elastic) properties, but also on the phase stability and the thermodynamical properties of a solid. Subsequently physical quantities like the mean force constant, the mean atomic displacement, internal energy, heat capacity or vibrational entropy can be directly deduced. The property of interest is here the dispersion relation and the phonon density of states (DOS). From a historical perspective, first only the dispersion relation was directly accessible from experiments. Here the main method has been neutron scattering, as thermal neutrons are available at high fluxes from nuclear reactors. Additionally, limited information can be gained from methods employing light scattering like Brillouin and Raman scattering, where the latter studies incoherent molecular vibrations. The problem with these methods, however, is the small modulus of the wave vector transfer $q \leq 4\pi/\lambda \approx 2 \times 10^{-2} \text{ nm}^{-1}$, where λ denotes the wavelength of an x-ray photon. Thus the dispersion relation can only be investigated in a small fraction of the Brillouin zone. The advent of synchrotron sources of high brilliance allowed for new methods, the one used in this study is described in the next section.

The goal of this work was to investigate atomic dynamics in the $L1_0$ -phase of FePt.

For the motivation, why this particular phase is of great importance, see Sec. 1.1. For the $L1_0$ -structure in general only a few investigations exist [Mehaddene et al., 2004; Pierron-Bohnes et al., 2007; Ghosh, 2009]. Recently, a comparable study of FePt with the very technique used in our investigation, attempted to measure the anisotropic DOS in nanoparticles [Tamada et al., 2010]. However, the angular distribution of orientations of the structure in the particles did not permit the separation of the directional dependence. Additionally surface vibrations may pose a non-negligible influence in such finite size structures. We believe that our results can deliver the full anisotropic DOS and shed a light on the influence of possible surface effects.

6.2. Nuclear inelastic resonant absorption

Atomic vibrations can be described as superposition of collective vibrational states of the atoms. Such a state with a defined energy and wave vector is called a phonon, a quasi-particle in the quantum picture. Single phonons can be created by targeting a solid with a particle beam of a certain energy. In creation or annihilation of these phonons, energy is transferred between the particles of the beam and the solid. This is called inelastic scattering, hence the name of the main class of methods used to investigate this physical phenomenon.

We mentioned earlier that the wavelength of x-rays, and of course thermal neutrons, is much more favourable to study phonons than that of lasers. Nevertheless the natural line width of conventional x-ray sources of about ~ 1 eV is by far too large for typical phonon energies $1 \text{ meV} < E < 100 \text{ meV}$. Thus only synchrotron sources with the aid of monochromators of sub-meV resolution can fulfill the demands of such experiments. The pulsed nature of the latter also allows for the separation of the nuclear from the electronic scattering. This way the resonance of the Mössbauer isotope ^{57}Fe can be used to only measure the DOS associated to the Fe-atoms in the lattice. A very similar setup can yield complementary information through inelastic electronic scattering. While in general the high flux of a synchrotron permits the study of very small samples, like thin films or nanoparticles, the isotope specific resonance makes it possible to even probe certain areas of the already small volumes, e.g., a certain layer in a thin film. Furthermore the samples do not even have to be of crystalline nature. It would be entirely possible to measure polycrystalline, disordered, amorphous, even liquid or gaseous phases and investigate them during structural or phase transformations.

Most importantly, this method yields the DOS $D(E)$ directly without a physical model, in contrast to the dispersion relation $E(\mathbf{q})$ from inelastic neutron scattering and all the other methods. On the other hand the dispersion relation can not be probed due to the incoherent nature of the method. So the information gained from both methods is fundamentally different. The pioneering experiments have been conducted almost simultaneously by Seto et al. [1995]; Sturhahn et al. [1995]; Chumakov et al. [1995].

THEORY

7.1. Nuclear inelastic scattering theory

This section mainly follows the approach of Kohn and Chumakov [2000]. A very fundamental treatment of the theoretical aspects of the subject is given by Sturhahn and Kohn [1999].

In the following a relation between spectral inelastic nuclear resonant absorption and the projected partial phonon density of states is established. The theoretical framework of inelastic scattering was already worked out by Singwi and Sjölander [1960] and the principles can even be found in the work of Van Hove [1954]. The energy range of the hyperfine structure of the nuclear resonance is assumed to be much smaller than typical phonon energies, thus the former can be neglected. Because the distinction of resonant atoms is experimentally not viable and in our case resonant atoms occupy equivalent sites, I only consider a single distinct resonant site. With these presumptions in mind the normalized probability of absorption W per unit energy interval and resonant atom, at the energy E is given by [Singwi and Sjölander, 1960]

$$\begin{aligned} W(E, \mathbf{k}) &= \frac{1}{2\pi} \int d\tau e^{-iE\tau - \Gamma|\tau|/2} \left\langle e^{-i\mathbf{k}\mathbf{u}(0)} e^{i\mathbf{k}\mathbf{u}(\tau)} \right\rangle_T \\ &= \frac{1}{2\pi} \int d\tau e^{-iE\tau - \Gamma|\tau|/2} e^{-M(0, \mathbf{k})} e^{M(\tau, \mathbf{k})} \end{aligned} \quad (7.1)$$

with the time t , $\tau = t/\hbar$, the natural width of the nuclear excited state Γ , the difference in energy between the incident x-ray and the resonance energy of the nuclear transition

E and the wave vector of the incident x-ray \mathbf{k} .

The brackets $\langle \rangle_T$ denotes the quantum mechanical, that is the sum over the initial states of the atoms in the lattice, and thermal average at temperature T of a spatial and temporal self-correlation function involving the atomic displacements from their equilibrium position \mathbf{u} . For a harmonic lattice the self-correlation function can be evaluated to the exponentials above where M unfolds to

$$M(\tau, \mathbf{k}) = \frac{E_R V}{k^2} \sum_{\mathbf{q}, j} \frac{|\mathbf{k} \cdot \mathbf{e}_j(\mathbf{q})|^2}{\hbar \omega_j(\mathbf{q})} \left((n_j(\mathbf{q}) + 1) e^{i\hbar \omega_j(\mathbf{q}) \tau} + n_j(\mathbf{q}) e^{-i\hbar \omega_j(\mathbf{q}) \tau} \right) \quad (7.2)$$

with the modulus of the wave vector $k \equiv |\mathbf{k}|$ and the mass and recoil energy of the nucleus denoted as m and $E_R = \hbar^2 k^2 / 2m$, respectively, the volume per unit cell V , the phonon dispersion relation of branch j , $\omega_j(\mathbf{q})$ and the polarization vector of the vibrations \mathbf{e}_j . The occupation of states is given by the Bose-Einstein distribution function

$$n_j(\mathbf{q}) = \frac{1}{e^{\beta \hbar \omega_j(\mathbf{q})} - 1} \quad (7.3)$$

with $\beta \equiv 1/k_B T$. The first factor of the integrand in W turns out to be the angle-dependent Lamb-Mössbauer factor $f_{\text{LM}}(\mathbf{k}) = e^{-M(0, \mathbf{k})}$. The second exponential factor can be expanded into n -phonon creation or annihilation contributions

$$W(E, \mathbf{k}) = f_{\text{LM}}(\mathbf{k}) S(E, \mathbf{k}) = f_{\text{LM}}(\mathbf{k}) \sum_{n=0}^{\infty} S_n(E, \mathbf{k}), \quad (7.4)$$

where the term of zeroth-order represents elastic nuclear absorption

$$S_0(E) = \frac{1}{2\pi} \int d\tau e^{-iE\tau - \Gamma|\tau|/2} = \frac{1}{2\pi} \frac{\Gamma}{E^2 + \Gamma^2/4} = \delta_{\Gamma}(E). \quad (7.5)$$

For Γ much smaller than typical phonon energies I set $\lim_{\Gamma \rightarrow 0} \delta_{\Gamma}(E) = \delta(E)$. Furthermore the first order term is

$$\begin{aligned} S_1(E) &= \frac{E_R V}{k^2} \sum_{\mathbf{q}, j} \frac{|\mathbf{k} \cdot \mathbf{e}_j(\mathbf{q})|^2}{\hbar \omega_j(\mathbf{q})} \left((n_j(\mathbf{q}) + 1) \delta(E - \hbar \omega_j(\mathbf{q})) + n_j(\mathbf{q}) \delta(E + \hbar \omega_j(\mathbf{q})) \right) \\ &= \frac{E_R V}{k^2} \sum_{\mathbf{q}, j} \frac{|\mathbf{k} \cdot \mathbf{e}_j(\mathbf{q})|^2}{E(1 - e^{-\beta E})} \left(\delta(E - \hbar \omega_j(\mathbf{q})) + \delta(E + \hbar \omega_j(\mathbf{q})) \right) \end{aligned}$$

$$= \frac{E_R D_p(|E|, \mathbf{k})}{E(1 - e^{-\beta E})}, \quad (7.6)$$

where for the second line the Bose-Einstein distribution of Eq. (7.3) was inserted. The so defined function D_p is called the projected phonon density of states (PDOS) and reads

$$D_p(E, \mathbf{k}) = \frac{V}{(2\pi)^3 k^2} \sum_j \int d\mathbf{q}^3 |\mathbf{k} \cdot \mathbf{e}_j(\mathbf{q})|^2 \delta(E - \hbar\omega_j(\mathbf{q})). \quad (7.7)$$

In case of a cubic Bravais lattice or a polycrystalline solid with only resonant atoms this function simplifies to the phonon density of states D (DOS)

$$D(E) = \frac{V}{3(2\pi)^3} \sum_j \int d\mathbf{q}^3 \delta(E - \hbar\omega_j(\mathbf{q})). \quad (7.8)$$

From here on I neglect the linewidth Γ in the exponential, as the relativ hyperfine energies (\sim neV) are much smaller than the typical phonon energies (\sim meV). The higher order terms are subsequently

$$S_n(E, \mathbf{k}) = \frac{1}{2\pi n!} \int d\tau e^{-iE\tau} M(\tau, \mathbf{k}) M(\tau, \mathbf{k})^{n-1} \quad (7.9)$$

and with the aid of the convolution theorem we get the recursive solution

$$S_n(E, \mathbf{k}) = \frac{1}{n} \int dE' S_1(E', \mathbf{k}) S_{n-1}(E - E', \mathbf{k}). \quad (7.10)$$

7.2. Phonon density from experiment

The experimental spectra of nuclear inelastic resonant absorption always include contributions from instantaneous multi-phonon creation or annihilation. In fact the fraction of the n -phonon contribution can be estimated by

$$\int dE S_n(E, \mathbf{k}) = \frac{1}{n!} (-\ln f_{\text{LM}}(\mathbf{k}))^n \quad (7.11)$$

with the Lamb-Mössbauer factor f_{LM} . Ideally a Lamb-Mössbauer factor close to unity would guarantee relatively few multi-phonon events.

Nevertheless a method to separate the single-phonon from the multi-phonon contributions is required, as the former is in a close relationship to the partial PDOS. The

Fourier transform of Eq. (7.10) results in a simple recursive formula

$$\tilde{S}_n(t, \mathbf{k}) = \frac{1}{n} \tilde{S}_{n-1}(t, \mathbf{k}) \tilde{S}_1(t, \mathbf{k}) \quad (7.12)$$

with the closed solution

$$\tilde{S}_n(t, \mathbf{k}) = \frac{1}{n!} \tilde{S}_1(t, \mathbf{k})^n. \quad (7.13)$$

In the equations above and in the rest of this section the Fourier transform \mathcal{F} of an operator A is denoted by $\tilde{A} \equiv \mathcal{F}A$. Subsequently for the total of all the n -phonon contributions we have

$$\tilde{S}(t, \mathbf{k}) = f_{\text{LM}}(\mathbf{k}) e^{\tilde{S}_1(t, \mathbf{k})}. \quad (7.14)$$

This permits the extraction of the one-phonon contribution as follows

$$S_1(E, \mathbf{k}) = \int dt e^{-iEt} \ln \frac{\tilde{S}(t, \mathbf{k})}{f_{\text{LM}}(\mathbf{k})}. \quad (7.15)$$

Taking the experimental resolution function R into account, that is mainly the monochromator function measured from energy resolved elastic forward scattering,

$$I'(E, \mathbf{k}) = \int dE' R(E - E') (aS(E', \mathbf{k}) - bf_{\text{LM}}\delta(E')), \quad (7.16)$$

the one-phonon contribution now reads

$$S_1(E, \mathbf{k}) = \int dt e^{-iEt} \ln \left(1 + \frac{\tilde{I}'(t, \mathbf{k})}{af_{\text{LM}}(\mathbf{k})\tilde{R}(t)} \right). \quad (7.17)$$

This recipe to extract the one-phonon contribution from the time dependent intensity I' of deexcitation after the pulsed excitation by the synchrotron beam, where the elastic nuclear absorption peak in the center is removed, is called the Fourier-Log decomposition. The constants a and b are necessary to correct for saturation of the detection system at the intense resonance. A detailed description of the intricacies of the extraction procedure can be found in Kohn and Chumakov [2000].

7.3. Anisotropic density of states

In the anisotropic case Eq. 7.7 for the partial phonon density of states has to be modified to the quadratic form [Sturhahn and Kohn, 1999; Röhlsberger, 2004]

$$D_p(E, \mathbf{k}) = \sum_{\mu, \nu} k_\mu T_{\mu\nu}(E) k_\nu, \quad (7.18)$$

$$T_{\mu\nu}(E) = \frac{1}{(2\pi)^3} \frac{V}{Nk^2} \sum_{m=1}^N \sum_j \int d\mathbf{q}^3 \delta(E - \hbar\omega_j(\mathbf{q})) (\mathbf{e}_{j,m})_\mu (\mathbf{e}_{j,m})_\nu^* \quad (7.19)$$

with the volume of the unit cell V , the number of resonant atoms in the unit cell N . This form is directly related to the fundamental structure of the physics in the solid, that is the Hamiltonian for a harmonic lattice in the center of mass system [Sturhahn and Kohn, 1999]

$$H = \sum_{n,\mu} \frac{1}{2m_n} p_{n,\mu}^2 + \frac{1}{2} \sum_{m,n} \sum_{\mu,\nu} u_{m,\mu} D_{mn,\mu\nu} u_{n,\nu} \quad (7.20)$$

with the force constant tensor \mathbf{D} and the atomic displacement vectors \mathbf{u} and m and n running over all the atoms in the ensemble.

So for a Cartesian coordinate system coinciding with the lattice similar to Fig. 2.1 with the angle of incidence even below the total reflection the wave vector of the incident wave can be expressed by

$$\mathbf{k} = \frac{1}{\sqrt{2}} \begin{bmatrix} 1 \\ 0 \\ 1 \end{bmatrix}. \quad (7.21)$$

In such a basis the tensor describing the PDOS is diagonal, and the actual measured components are

$$D_p(E) = \frac{1}{2} (T_{11}(E) + T_{33}(E)). \quad (7.22)$$

This relation and the separate measurement of T_{11} is used to decompose contributions from different directions in the lattice.

EXPERIMENT

8.1. Samples

The lack of bulk single-crystalline samples of good quality forces one to look for alternative methods to investigate atomic vibrations in $L1_0$ -FePt. Nevertheless, through epitaxial deposition of films on suitable substrates certain orientations of the lattice are favoured, thus enabling the preparation of single-crystalline films. Previous studies showed the feasibility of FePt-films grown by molecular beam epitaxy (MBE) on MgO substrates [Farrow et al., 1996; Laenens et al., 2009].

In fact the samples are very similar to the ones used for the diffusion studies described in Sec. 3.1. This time the films are enriched by the resonant ^{57}Fe -isotope over the whole depth, in contrast to the periodic enrichment for the study of diffusive smearing of the isotopic superstructure. The slightly smaller thickness of 30 nm, however, does not cause any qualitative difference of the overall properties. The actual thickness after preparation determined by x-ray reflectometry was 27 nm with a roughness of < 0.3 nm and 1 nm for the film on MgO(100) and MgO(110), respectively. The long-range-order parameter was calculated to 0.9 and 0.85, respectively, which suggests fairly good ordering.

As was mentioned above the applied method yields the DOS projected onto the axis of the incoming photon beam. Thus to probe the anisotropy in a tetragonal structure at least one of the measured directions has to have a non-vanishing component in the direction of the distinct c -axis, or vice versa. So besides the sample on MgO(100) with

the c -axis, and therefore the magnetization, normal to the surface, films with one of the a -axes canted out of the surface by 45° have been prepared on MgO(110). For a more detailed description of the orientation see Sec. 7.3 and Laenens et al. [2007]. To ensure consistency from the point of view of preparation the samples have been grown simultaneously on a single sample stage by co-evaporation of ^{57}Fe (effusion cell) and Pt (electron-bombardment heating). The partial film growth rates have been adjusted to 0.0027 nm s^{-1} and 0.0035 nm s^{-1} for ^{57}Fe and Pt, respectively. During preparation the sample was kept at a constant temperature of 500°C .

X-ray diffraction on the one hand confirmed the orientation of the lattice and on the other permitted insight on the lattice constants of $a = 0.385 \text{ nm}$ and $c = 0.371 \text{ nm}$ for both samples. These values compare very well with the literature on bulk samples [Kudielka and Runow, 1976] suggesting a relaxed lattice for the most part of the sample, considerable better than in Laenens et al. [2007]. The orientation of the distinct axis, and thus the magnetization axis, was additionally checked by conversion electron Mössbauer spectroscopy (CEMS) analogous to Sec. 3.1. The magnetization axis has been perpendicular and 45° canted to the sample surface for FePt(100) and FePt(110), respectively, as expected. Rutherford backscattering suggests a fairly stoichiometric sample at a composition of $\text{Fe}_{0.49}\text{Pt}_{0.51}$ with a slight excess of Pt.

8.2. Nuclear resonant experiment

The high photon flux and spectral density of modern synchrotron facilities and the resonant nature of the interaction in nuclear resonant scattering renders nuclear inelastic resonant absorption (NIRA) a viable approach to investigate samples of very small dimensions, like nanoparticles or in our case nanofilms. Again the pulsed time structure is used to separate the nuclear from the more intense electronic scattering amplitude. The following details on the experimental setup are taken mainly from Chumakov and Sturhahn [1999].

The monochromatization of the beam is achieved via a high-heat-load and a high-resolution monochromator. In the latter a high-order reflection guarantees a narrow spectral width of $\sim \text{meV}$ and permits energy modulation through a large angular energy dispersion.

Two detectors are used to measure the scattered x-rays, namely Avalanche photo diodes (APD), for details see Sec. 3.2. The first detector is placed directly above the

sample stage and counts the incoherent inelastic events of nuclear resonant scattering. Basically there exist three possible decay paths for this technique

- i. nuclear resonant fluorescence,
- ii. conversion electrons emission and
- iii. atomic fluorescence

For ^{57}Fe the contribution of the first option is neglectable due to its small partial internal conversion coefficient. Furthermore the decay by internal conversion results in an unoccupied inner shell state, which in turn promotes an outer shell electron to fill that gap with the subsequent emittance of a photon, the third possibility of above. In our case the latter was utilized to determine the spectral dependence of the nuclear absorption yield, but alternatively conversion electrons could be used to promote surface sensitivity.

To measure the experimental resolution function R of Eq. (7.16) the coherent elastic nuclear intensity is measured in forward direction with the detector far from the sample to avoid incoherent contributions. Due to small instabilities of the monochromators the elastic nuclear peak is measured throughout the experiment.

The nuclear inelastic resonance absorption measurement was conducted at ID18 of ESRF in Grenoble, optimized for nuclear resonant experiments, in 16 bunch mode. The spectral step size was chosen to be 0.2 meV for a monochromator resolution of 0.8 meV. The sample were simply placed below a detector, sensitive to electronic fluorescence, so the actual measurements was carried out at room-temperature under ambient conditions. The incident angle was adjusted to $0.26^\circ = 4.5$ mrad, below the angle of total reflection. Therefore we can expect high surface sensitivity, as the upper nanometer of the FePt-film is responsible for more than 25% of the signal. The summed up NIRA spectra are shown in Fig. 8.1. The yellow data represents the film with the c -axis normal to the sample surface, whereas the other two data sets mark the scans for the 45° canted sample, taken in the two perpendicular in-plane directions along the crystalline axes [100] and [110]. For the former sample an additional scan with the sample rotated 45° about the surface normal was recorded, which showed the same energy dependence, as it should. Of the latter two spectra the one in the [100]-direction resembles that of the sample with the c -axis perpendicular to the surface, as this measurment direction also has no component in the c -direction. The remaining

data resulted from the experiment with the incoming wave vector in the [011] direction of the lattice, thus effectively representing the mixed DOS of $\frac{1}{2}(T_{22} + T_{33})$.

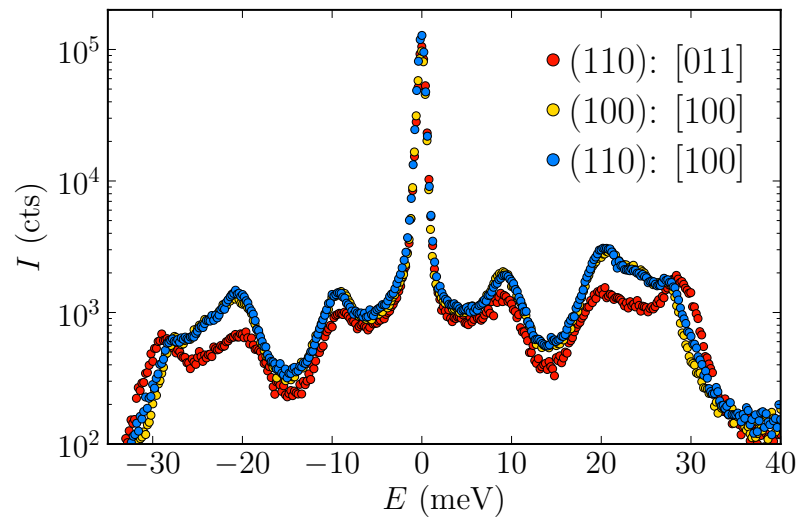


Figure 8.1.: The summed NIRA spectra for Fe in FePt of the film on MgO(100) and two in-plane perpendicular directions of the film on MgO(110).

RESULTS

9.1. Phonon density of states

The following results are published in Couet, Sternik, Laenens, Siegel, Parlinski, Planckaert, Gröstlinger, Chumakov, Ruffer, Sepiol, Temst, and Vantomme [2010], where S. Couet, N. Planckaert and myself were responsible for the nuclear inelastic measurement. The DOS-software [Kohn and Chumakov, 2000] was used to extract the projected partial density of states. The basic method implemented in the program is described in Sec. 7.2. To iterate this is only the part of the vibrational modes associated with the Fe-atoms in the FePt-alloy. The geometric relation to separate the PDOS measured on the 45° canted structure of FePt on MgO(110) is described by Eq. (7.22). The component of the DOS in c -direction can then be computed from the mixed DOS $T_{[011]}$ by

$$T_{33} = 2T_{[011]} - T_{11}, \quad T_{22} = T_{11}. \quad (9.1)$$

Fig. 9.1 illustrates the combined and separated PDOS. Data points below 1.5 meV should not be trusted as for the removal of the elastic peak the data was interpolated in this range. What is immediately noticed is the much smaller density of low-energy vibrational modes in c -direction. The overwhelming majority of states is concentrated around a vibrational energy of about 29 meV. The associated elastic and thermodynamic properties calculated from the spectra are listed in Tab. 9.1. The largest variations in the different directions can be found for the mean of the force constant and the sound velocity, which is plausible as these should be directional

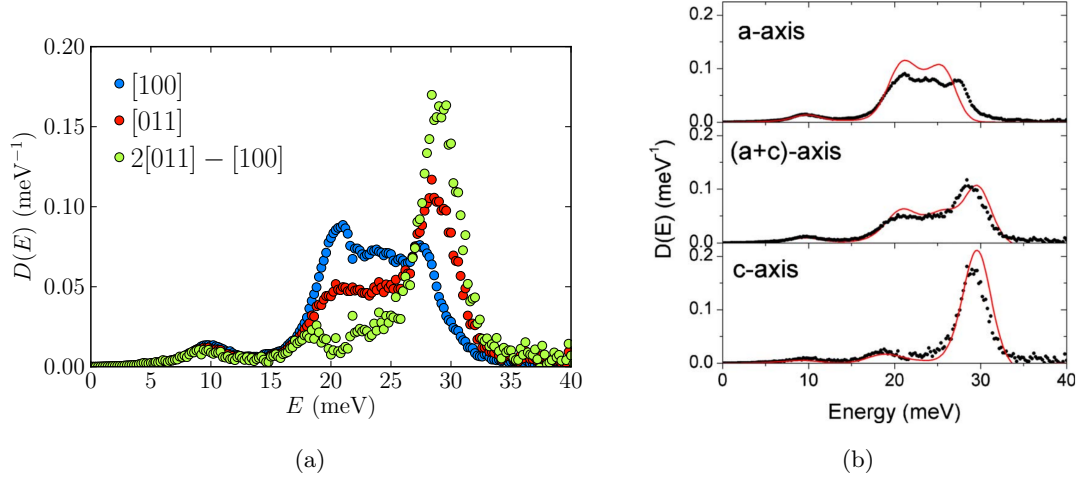


Figure 9.1.: (a) The PDOS for Fe in FePt for different directions in the crystal. (b) The experimental data is compared to ab-initio calculations smeared by a normal distribution accounting for the experimental resolution [Couet et al., 2010].

properties. Furthermore they can give a qualitative insight for finding suitable models for Monte-Carlo simulations of diffusion. However, to connect the data to the intrinsic physical properties first-principles calculations have to be in agreement.

Table 9.1.: Physical quantities calculated from the measured PDOS in different crystalline directions.

Physical quantity	a	$a + c$	c
specific heat (k_B/atom)	2.78(1)	2.76(1)	2.73(1)
vibrational entropy (k_B/atom)	3.52(1)	3.31(1)	3.12(1)
mean atomic displacement (10^{-3} nm)	7.5(1)	7.3(1)	7.2(1)
mean force constant (10^2 N m $^{-1}$)	1.296(4)	1.439(4)	1.592(4)
mean sound velocity (10^3 m s $^{-1}$)	2.214(20)	2.101(20)	2.016(20)

9.2. Ab-initio calculations

First-principles calculations of lattice dynamics were conducted by M. Sternik¹ to relate the measured data to intrinsic physical properties. The supercell with periodic boundary conditions was constructed of $4 \times 4 \times 3$ unit cells containing a total of 96 atoms. For the crystal relaxation and the calculation of Hellmann-Feynman forces the VASP software [Kresse and Furthmüller, 1996] was utilized. To be specific spin-polarized total-energy density functional formulation with general-gradient approximation was used for the exchange-correlation functionals. The Hellmann-Feynman forces for small atomic displacements from the equilibrium position are subsequently used to compute the phonon dispersion relation [Parlinski et al., 1997]. This involves the diagonalization of the dynamical matrix for a large set of wave vectors. Subsequently the PDOS was obtained for the given experimental configurations. The optimized lattice parameters $a = 0.386$ nm and $c = 0.377$ nm agree very well to the experimentally found bulk values. The experimental resolution function (0.8 meV) and the finite lifetime of the phonons was implemented by convolving the theoretical PDOS with a normal distribution of width $\sigma_{\text{FWHM}} = 6$ meV. As shown in Fig. 9.2(a) the PDOS from ab-initio calculations for a fully relaxed bulk crystal is shifted to lower energies compared to the experimental findings. However, the lattice constants obtained experimentally from x-ray diffraction deviate significantly from the theoretical values in one direction, i.e. $c_{\text{exp}} = 0.371$ nm $<$ 0.377 nm. Thus adapted ab-initio calculations with a predefined strained structure according to the experimental lattice constants were performed. In this configuration the first major peak in the resulting PDOS agrees very well with the experimental data (see Fig. 9.2). The features are very similar except the cutoff at lower energies. The final fits to the data in the different directions are shown in Fig. 9.1(b). Note that the uniaxial strain shifts the PDOS in all directions. Therefore the PDOS is very sensitive to elastic strain represented by changes in the lattice spacing.

9.3. Surface modes

As mentioned earlier the grazing-incidence geometry even below total reflection renders the experiment prone to surface effects. Thus the measured PDOS could to a significant degree be originating from a disturbed PDOS of the first few layers, where

¹Institute of Nuclear Physics, Polish Academy of Sciences, Kraków, Poland

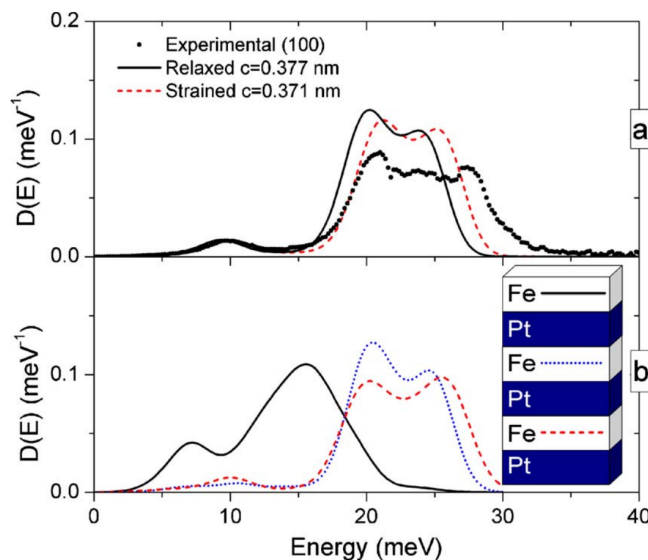


Figure 9.2.: Ab-initio calculations of Fe-PDOS in FePt and experimental data for (a) a relaxed bulk lattice in a -direction compared to the strained lattice in a thin film sample and (b) depth dependent PDOS calculations, where the one of the first layer differs considerable from the bulk one [Couet et al., 2010].

the interatomic forces are asymmetric. For that reason further ab-initio calculations for 3 atomic bilayers of Fe/Pt with free surfaces above and below the film have been performed. Of the resulting spectra (see Fig. 9.2(b)) only the Fe-layer directly at the surface shows a completely different PDOS, whereas the layers immediately below behave fairly bulk-like. Since the top layer should make up roughly 10% of the measured signal, the lack of additional low-energy modes in the measured spectra suggests the surface to be Pt-terminated. This view is supported by surface-energy studies on FePt and CoPt [Dannenberg et al., 2009].

Similar to a study of metallic Fe on W(110) bulk-like behaviour is assumed as soon as the second layer. In general even very thin films should show vibrational modes close to bulk samples. Furthermore, even the PDOS of FePt-nanoparticles should be similar to the infinite case, as long as they are Pt-terminated. A recent study [Tamada et al., 2010] employing the same technique on such nanoparticles of an estimated size of 5 nm reports on a qualitatively very similar anisotropic PDOS. On a closer look, however, we can find these additional low-energy modes accounted to Fe-surface layers.

CHAPTER 10

CONCLUSION

A comprehensive study about the phonon density of states and in particular its anisotropy in FePt thin films is presented. While we find several low-energy modes in the a -direction, in the c -direction the vibrational modes are concentrated on the upper end at 29 meV. The general form of the PDOS observed here, should, in our opinion, be qualitatively valid for intermetallic alloys of the $L1_0$ structure. The experimental data is in good agreement with ab-initio calculations, if the lattice strain in the film induced by the substrate is incorporated by a smaller cell in c -direction.

To exclude strong surface contributions favoured in the grazing-incident geometry, further ab-initio calculations found a surface-induced deviation of the PDOS only in the first Fe layer. However, these additional modes are not present in the experimental data, suggesting a Pt-terminated film. The results are in relatively good agreement with a study on FePt-nanoparticles investigated with the same technique. The small but significant contribution of low-energy modes may point to Fe-terminated particles, nevertheless this calls for closer investigation. In conclusion, the presented information should give a general idea of anisotropic properties of atomic vibrations for the class of $L1_0$ alloys in bulk but also in thin films and to a certain extent in nanoparticles.

NUCLEAR RESONANT SCATTERING

A.1. Lippmann-Schwinger equation and Born approximation

Let us consider a time-independent scattering problem with the energy eigenstate $|\phi\rangle$ of the free field Hamiltonian $\mathbf{H}_0 \Rightarrow \mathbf{H}_0|\phi\rangle = E|\phi\rangle$. Now I introduce a scattering operator \mathbf{M} describing a weak perturbation to \mathbf{H}_0 that does not change the energy but only the state of the field

$$(\mathbf{H}_0 + \mathbf{M})|\psi\rangle = E|\psi\rangle. \quad (\text{A.1})$$

A solution can be found using the Lippmann-Schwinger equation with an infinitesimal ϵ to remove the singularity of $(E - \mathbf{H}_0)^{-1}$

$$|\psi\rangle = |\phi\rangle + \frac{1}{E - \mathbf{H}_0 + i\epsilon} \mathbf{M}|\psi\rangle. \quad (\text{A.2})$$

In the space representation with all the possible eigenstates $\mathbf{H}_0|\mathbf{k}\rangle = E_{\mathbf{k}}|\mathbf{k}\rangle$ I may transform this to

$$\begin{aligned} \langle \mathbf{x}|\psi\rangle &= \langle \mathbf{x}|\phi\rangle + \langle \mathbf{x}|\frac{1}{E - \mathbf{H}_0 + i\epsilon} \mathbf{M}|\psi\rangle \\ &= \langle \mathbf{x}|\phi\rangle + \int d^3k \langle \mathbf{x}|\mathbf{k}\rangle \langle \mathbf{k}|\frac{1}{E - \mathbf{H}_0 + i\epsilon} \mathbf{M}|\psi\rangle \end{aligned}$$

$$\begin{aligned}
&= \langle \mathbf{x} | \phi \rangle + \int d^3k \langle \mathbf{x} | \mathbf{k} \rangle \frac{1}{E - E_{\mathbf{k}} + i\epsilon} \langle \mathbf{k} | \mathbf{M} | \psi \rangle \\
&= \langle \mathbf{x} | \phi \rangle + \int d^3k \langle \mathbf{x} | \mathbf{k} \rangle \frac{1}{E - E_{\mathbf{k}} + i\epsilon} \int d^3k' \langle \mathbf{k} | \mathbf{M} | \mathbf{k}' \rangle \langle \mathbf{k}' | \psi \rangle. \quad (\text{A.3})
\end{aligned}$$

For the first order Born approximation one replaces the resulting state of the field with the incident state on the right-hand side $|\psi\rangle \rightarrow |\phi\rangle$

$$\langle \mathbf{x} | \psi \rangle = \langle \mathbf{x} | \phi \rangle + \int d^3k \langle \mathbf{x} | \mathbf{k} \rangle \frac{1}{E - E_{\mathbf{k}} + i\epsilon} \int d^3k' \langle \mathbf{k} | \mathbf{M} | \mathbf{k}' \rangle \langle \mathbf{k}' | \phi \rangle, \quad (\text{A.4})$$

which is equivalent to the first order term of the Born expansion. The wave representation of the above

$$\mathbf{A}(\mathbf{x}) = \mathbf{A}_0(\mathbf{x}) + \frac{1}{(2\pi)^3} \int d^3k e^{i\mathbf{k}\cdot\mathbf{x}} \frac{1}{E - E_{\mathbf{k}} + i\epsilon} \int d^3k' \mathbf{M}(\mathbf{k}, \mathbf{k}') \tilde{\mathbf{A}}_0(\mathbf{k}'). \quad (\text{A.5})$$

resembles the initial equation of the dynamical scattering theory except for an additional energy transfer between the photons and the nuclei. Since this transfer is reversed on emission the outer structure of these equations is similar.

A.2. Algebraic structure of dynamical scattering

In this section the algebraic structure of the dynamical scattering will be developed according to Röhlsberger [1999, 2004]. This is done by firstly introducing an arbitrary scattering operator $\hat{\mathbf{M}}$ describing the sum of all scattering events originating from a wave with frequency ω' and wave vector \mathbf{k}' ending up in a wave with frequency ω and wave vector \mathbf{k} . In the first order Born approximation for a thin scatterer the resulting field can be calculated from

$$\tilde{\mathbf{A}}(\omega, \mathbf{k}) = -\frac{c}{(2\pi)^4} P_\gamma(\omega, \mathbf{k}) \int d\omega' d^3k' \hat{\mathbf{M}}(\omega, \mathbf{k}, \omega', \mathbf{k}') \tilde{\mathbf{A}}_0(\omega', \mathbf{k}') \quad (\text{A.6})$$

with the photon propagator P_γ

$$P_\gamma(\omega, \mathbf{k}) = -\frac{4\pi c}{\omega^2 - k^2 c^2 + i\epsilon}. \quad (\text{A.7})$$

From right to left this reads as the incident wave $\tilde{\mathbf{A}}_0$ scattered by the scattering operator $\hat{\mathbf{M}}$ and integrated over all possible incident waves. The propagation of the resulting field is then described by the so called photon propagation operator P_γ . Due to polarization dependence the scattering operator $\hat{\mathbf{M}}$ and the wave amplitudes are 2-dimensional matrices and vectors, respectively, represented in a convenient polarization basis. For different atomic subgroups j the scattering operator for elastic scattering $\omega' = \omega$ consists of a geometrical phase factor identified as the structure function S_j and the atomic scattering amplitude \mathbf{M}_j

$$\hat{\mathbf{M}}(\omega, \mathbf{k}, \omega', \mathbf{k}') = \delta(\omega - \omega') \sum_j S_j(\mathbf{k} - \mathbf{k}') \mathbf{M}_j(\omega, \mathbf{k}, \omega', \mathbf{k}'). \quad (\text{A.8})$$

The structure function S_j as a function of the scattering vector $\mathbf{q} = \mathbf{k} - \mathbf{k}'$ contains all the information about the atomic arrangement as it is the Fourier transform of the atomic number density ρ_j

$$S_j(\mathbf{q}) = \int_V dx^3 e^{i\mathbf{q}\cdot\mathbf{x}} \rho_j(\mathbf{x}). \quad (\text{A.9})$$

Let us now calculate the structure function for a thin homogeneous film of thickness d infinite in the (x, y) -plane, for which the first order Born approximation still holds

$$S_j(\mathbf{q}) = \rho_j \int_{-\infty}^{\infty} dx dy e^{i\mathbf{q}_{xy}\cdot\mathbf{x}} \int_0^d dz e^{iq_z z} = (2\pi)^2 \delta^2(\mathbf{q}_{xy}) \frac{e^{iq_z d} - 1}{iq_z} \rho_j \quad (\text{A.10})$$

with the in-plane scattering vector \mathbf{q}_{xy} . The scattering operator then reads

$$\hat{\mathbf{M}}(\omega, \mathbf{k}, \omega', \mathbf{k}') = (2\pi)^2 \delta(\omega - \omega') \delta^2(\mathbf{q}_{xy}) \frac{e^{iq_z d} - 1}{iq_z} \sum_j \rho_j \mathbf{M}_j(\omega, \mathbf{k}, \omega', \mathbf{k}'). \quad (\text{A.11})$$

Assuming a plane wave for the incident beam $\tilde{\mathbf{A}}_0(\omega', \mathbf{k}') = (2\pi)^4 \delta(\omega' - \omega_0) \delta^3(\mathbf{k}' - \mathbf{k}_0) \mathbf{A}_0$ we can put all together and immediately execute the integration over the δ -functions

for the scattered field

$$\tilde{\mathbf{A}}(\omega, \mathbf{k}) = -(2\pi)^2 c P_\gamma(\omega, \mathbf{k}) \delta(\omega - \omega_0) \delta^2(\mathbf{q}_{xy}) \frac{e^{iq_z d} - 1}{iq_z} \sum_j \rho_j \mathbf{M}_j(\omega, \mathbf{k}, \omega_0, \mathbf{k}_0) \mathbf{A}_0. \quad (\text{A.12})$$

Finally a Fourier transform $1/(2\pi)^4 \int d\omega dk^3 e^{i(\mathbf{k}\cdot\mathbf{r}-\omega t)} \tilde{\mathbf{A}}(\omega, \mathbf{k})$ yields the corresponding amplitude in time t and space \mathbf{x} . Again the integration over the δ -functions leaves us with

$$\mathbf{A}(t, \mathbf{x}) = \frac{1}{i\pi} e^{i(\mathbf{k}_{0xy}\cdot\mathbf{x}-\omega_0 t)} \int dk_z \frac{e^{ik_z z} (e^{i(k_z - k_{0z})d} - 1)}{(k_{0z}^2 - k_z^2 + i\epsilon/c^2)(k_z - k_{0z})} \sum_j \rho_j \mathbf{M}_j(k_z, k_{0z}) \mathbf{A}_0, \quad (\text{A.13})$$

where I have dropped the dependence of the atomic scattering amplitude \mathbf{M}_j on k_{0x} and k_{0y} for now. To solve the integral one has to calculate the residues of the function

$$f(k_z) = \lim_{\epsilon \rightarrow 0} \int dk_z \frac{e^{ik_z z} (e^{i(k_z - k_{0z})d} - 1)}{(k_{0z\epsilon} - k_z)(k_{0z\epsilon} + k_z)(k_z - k_{0z})} \sum_j \rho_j \mathbf{M}_j(k_z, k_{0z}) \mathbf{A}_0 \quad (\text{A.14})$$

with $k_{0z\epsilon} \equiv \sqrt{k_{0z}^2 + i\epsilon/c^2}$ and subtract the contribution of the integration over an arc of radius R in the positive and negative complex half plane, respectively. Fortunately the integrand is bounded for every k_z on that arc and vanishes for $R \rightarrow 0$. Therefore the solution consists solely of the residues resulting in

$$\begin{aligned} \text{Res}(f, k_{0z}) &= 0 \\ \text{Res}(f, k_{0z\epsilon}) &= \frac{ide^{ik_{0z}z}}{2k_{0z}} \sum_j \rho_j \mathbf{M}_j(k_{0z}, k_{0z}) \mathbf{A}_0 \\ \text{Res}(f, -k_{0z\epsilon}) &= -\frac{e^{-ik_{0z}z} (e^{-2ik_{0z}d} - 1)}{4k_{0z}^2} \sum_j \rho_j \mathbf{M}_j(-k_{0z}, k_{0z}) \mathbf{A}_0. \end{aligned} \quad (\text{A.15})$$

Below the plane for $z \geq 0$ including the incident wave of $\mathbf{A}_0 e^{i(\mathbf{k}_+\cdot\mathbf{x}-\omega_0 t)}$ and the wave vector $\mathbf{k}_+ = [k_{0x}, k_{0y}, k_{0z}]$ we get for the field amplitudes

$$\begin{aligned} \mathbf{A}_+(t, \mathbf{x}) &= e^{i(\mathbf{k}_+\cdot\mathbf{x}-\omega_0 t)} \left(\mathbf{1} + \frac{1}{i\pi} 2\pi i \frac{id}{2k_{+z}} \sum_j \rho_j \mathbf{M}_j(\mathbf{k}_+, \mathbf{k}_+) \right) \mathbf{A}_0 \\ &= e^{i(\mathbf{k}_+\cdot\mathbf{x}-\omega_0 t)} (\mathbf{1} + id\mathbf{f}_{++}) \mathbf{A}_0, \end{aligned} \quad (\text{A.16})$$

where

$$\mathbf{f}_{++} \equiv \frac{1}{k_{+z}} \sum_j \rho_j \mathbf{M}_j(\mathbf{k}_+, \mathbf{k}_+). \quad (\text{A.17})$$

Above the plane for $z < 0$ and the wave vector $\mathbf{k}_- = [k_{0x}, k_{0y}, -k_{0z}]$ the field amplitude evaluates to

$$\begin{aligned} \mathbf{A}_-(t, \mathbf{x}) &= -e^{i(\mathbf{k}_- \cdot \mathbf{x} - \omega_0 t)} \frac{1}{i\pi} 2\pi i \frac{e^{2ik_{-z}d} - 1}{4k_{-z}^2} \sum_j \rho_j \mathbf{M}_j(\mathbf{k}_-, \mathbf{k}_+) \mathbf{A}_0 \\ &= -e^{i(\mathbf{k}_- \cdot \mathbf{x} - \omega_0 t)} id \mathbf{f}_{-+} \mathbf{A}_0, \end{aligned} \quad (\text{A.18})$$

where

$$\mathbf{f}_{-+} \equiv \frac{1}{k_{-z}} \frac{e^{2ik_{-z}d} - 1}{2ik_{-z}d} \sum_j \rho_j \mathbf{M}_j(\mathbf{k}_-, \mathbf{k}_+). \quad (\text{A.19})$$

Disregarding the phase factor $e^{ik_{0xy} \cdot \mathbf{x}}$ the resulting amplitude in $\mathbf{A}_+(z+d)$ and $\mathbf{A}_-(z-d)$ of waves $\mathbf{A}_+(z)$ and $\mathbf{A}_-(z)$ incident upon the layer at z is as shown in Fig. A.1

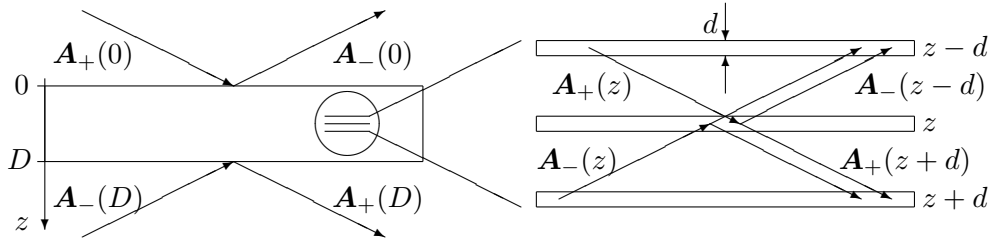


Figure A.1.: The layers on the right-hand side are infinitesimal sublayers of a homogeneous layer. In this system the resulting field for the layers at $z+d$ and $z-d$, respectively, originating from incident beams $\mathbf{A}_+(z)$ and $\mathbf{A}_-(z)$ is illustrated.

$$\begin{aligned} \mathbf{A}_+(z+d) &= e^{ik_{+z}d} ((\mathbf{1} + id\mathbf{f}_{++})\mathbf{A}_+(z) + id\mathbf{f}_{+-}\mathbf{A}_-(z)) \\ \mathbf{A}_-(z-d) &= e^{-ik_{-z}d} ((\mathbf{1} - id\mathbf{f}_{--})\mathbf{A}_-(z) - id\mathbf{f}_{-+}\mathbf{A}_+(z)). \end{aligned} \quad (\text{A.20})$$

In the limit of a infinitesimal layer $d \rightarrow 0 \Rightarrow k_{0z}d \ll 1$ I may expand the remaining exponential

$$\lim_{d \rightarrow 0} \frac{\mathbf{A}_+(z+d) - \mathbf{A}_+(z)}{d} = i((\mathbf{f}_{++} + \mathbf{k}_{+z})\mathbf{A}_+(z) + \mathbf{f}_{+-}\mathbf{A}_-(z))$$

$$\lim_{d \rightarrow 0} \frac{\mathbf{A}_-(z) - \mathbf{A}_-(z-d)}{d} = i(\mathbf{f}_{-+}\mathbf{A}_+(z) + (\mathbf{f}_{--} + \mathbf{k}_{-z})\mathbf{A}_-(z)) \quad (\text{A.21})$$

with $\mathbf{k}_{+z} = -\mathbf{k}_{-z} = k_{0z}\mathbf{1}$. Finally we arrive at the matrix representation of the field variation with depth z

$$\partial_z \mathbf{A}(z) = i\mathbf{F}\mathbf{A}(z), \quad (\text{A.22})$$

with \mathbf{A} the combined field amplitude for transmission \mathbf{A}_+ and reflection \mathbf{A}_- and the propagation matrix \mathbf{F} as

$$\mathbf{F} \equiv \begin{bmatrix} \mathbf{f}_{++} + \mathbf{k}_{+z} & \mathbf{f}_{+-} \\ \mathbf{f}_{-+} & \mathbf{f}_{--} + \mathbf{k}_{-z} \end{bmatrix}, \quad \mathbf{A} \equiv \begin{bmatrix} \mathbf{A}_+ \\ \mathbf{A}_- \end{bmatrix}. \quad (\text{A.23})$$

The components of the matrix \mathbf{F} and the vector \mathbf{A} are themselves 2-dimensional to account for polarization dependence.

A.3. Matrix exponential

For a square real or complex matrix \mathbf{F} the matrix exponential is defined by

$$e^{\mathbf{F}} \equiv \sum_{n=0}^{\infty} \frac{1}{n!} \mathbf{F}^n \quad (\text{A.24})$$

with the properties

- i. $e^{\mathbf{0}} = \mathbf{1}$
- ii. $e^{a\mathbf{X}}e^{b\mathbf{X}} = e^{(a+b)\mathbf{X}}$
- iii. $e^{\mathbf{X}}e^{-\mathbf{X}} = \mathbf{1}$
- iv. if \mathbf{Y}^{-1} exists $\Rightarrow e^{\mathbf{Y}\mathbf{X}\mathbf{Y}^{-1}} = \mathbf{Y}e^{\mathbf{X}}\mathbf{Y}^{-1}$
- v. if $[\mathbf{X}, \mathbf{Y}] = 0 \Rightarrow e^{\mathbf{X}}e^{\mathbf{Y}} = e^{\mathbf{Y}}e^{\mathbf{X}} = e^{\mathbf{X}+\mathbf{Y}}$
- vi. if $[\mathbf{X}, [\mathbf{X}, \mathbf{Y}]] = 0$ and $[\mathbf{Y}, [\mathbf{X}, \mathbf{Y}]] = 0 \Rightarrow e^{t(\mathbf{X}+\mathbf{Y})} = e^{t\mathbf{X}}e^{t\mathbf{Y}}e^{t^2[\mathbf{X}, \mathbf{Y}]/2}$.

If the matrix \mathbf{F} can be transformed into the diagonal form \mathbf{F}_D , then the columns of the transformation matrix \mathbf{S} are the eigenvectors of \mathbf{F} and the eigenvalues f_i are the diagonal elements of \mathbf{F}_D

$$\mathbf{F} = \mathbf{S}\mathbf{F}_D\mathbf{S}^{-1}. \quad (\text{A.25})$$

In this form we see that

$$e^{\mathbf{F}} = \sum_n \frac{1}{n!} \mathbf{F}^n = \sum_n \frac{1}{n!} (\mathbf{S} \mathbf{F}_D \mathbf{S}^{-1})^n = \mathbf{S} \left(\sum_n \frac{1}{n!} \mathbf{F}_D^n \right) \mathbf{S}^{-1} = \mathbf{S} e^{\mathbf{F}_D} \mathbf{S}^{-1} \quad (\text{A.26})$$

where $(\mathbf{F}_D \mathbf{F}_D)_{ij} = \sum_k f_i \delta_{ik} f_k \delta_{kj} = f_i^2 \delta_{ij}$ and $(\mathbf{F}_D^n)_{ij} = f_i^n \delta_{ij}$. The matrix exponential of a diagonal matrix is then just $(e^{\mathbf{F}_D})_{ij} = e^{f_i} \delta_{ij}$, and therefore the matrix exponential of an arbitrary diagonalizable matrix is the back-transform of a diagonal matrix of exponentials of the eigenvalues.

CODE EXAMPLES

The following code examples are tested to work with PYTHON 2.6.5. The compiler and the main libraries are open source and freeware to ensure maximum flexibility. The library NUMPY is the most established numerical computation package for PYTHON including standard functions and linear algebra facilities. The library MATPLOTLIB is the standard in the PYTHON-universe for publication quality plotting comparable to GNUPLOT and an interface similar to MATLAB. A large collection of scientific tools, e.g., fitting routines, forms the package SCIPY. There is also the package SYMPY for simple analytical computations, although still in development phase it can handle most basic analytical problems, e.g., differentiation, integration, solving and simplifying equations.

If one is deterred by the fact that every function has to be imported by itself, I would like to point out the following commands

```
from package import *  
import package
```

where the second command additionally keeps the namespace separated. Although this is not the recommended way, because valuable resources are wasted, it can however increase the speed in prototyping code.

B.1. Symmetry considerations

The following function calculates the diffusion current in a certain direction. For a tetragonal crystal the physical properties should be invariant to certain symmetry

elements, e.g., the rotation about $\pi/2$ around the e_3 axis. Employing this function one finds that for this statement to be true, one requires $D_1 = D_2$.

```

from sympy import symbols, Matrix, simplify, cos, sin, pi
from sympy import pprint as pr

def rotate_diff(angle, axis=3):
    """
    calculating diffusion current
    -----
    angle: rotation angle
    axis: axis number for rotation
    """
    R1 = lambda t: Matrix([ [1,      0,      0], # rotation axis 1
                           [0, cos(t), -sin(t)],
                           [0, sin(t),  cos(t)]]
    R2 = lambda t: Matrix([ [cos(t), 0, sin(t)], # rotation axis 2
                           [ 0, 1, 0],
                           [-sin(t), 0, cos(t)]]
    R3 = lambda t: Matrix([ [cos(t), -sin(t), 0], # rotation axis 3
                           [sin(t),  cos(t), 0],
                           [ 0,      0, 1]])

    RR = [R1, R2, R3] # list of rotation matrix functions
    R = RR[axis - 1](angle) # actual rotation matrix
    pr(R) # print rotation matrix
    C1, C2, C3 = symbols('C1, C2, C3') # symbolic variables
    J1, J2, J3 = symbols('J1, J2, J3') # symbolic variables
    D1, D2, D3 = symbols('D1, D2, D3') # symbolic variables
    C = Matrix([[C1], [C2], [C3]]) # concentration gradient vector
    J = Matrix([[J1], [J2], [J3]]) # measurement direction
    D = Matrix([[D1, 0, 0], [0, D2, 0], [0, 0, D3]]) # diffusivity matrix
    pr(D) # print diffusion matrix
    pr((J.T * D * C)[0]) # diffusion flux unrotated
    pr(simplify(((R * J).T * D * (R * C))[0])) # measurement rotated
    pr(simplify((J.T * (R.T * D * R) * C)[0])) # crystal rotated

rotate_diff(pi / 2)

```

B.2. Convolution via Fourier transform

The convolution of the initial condition and the fundamental solution is done via a Fourier transform. Note that in our case I have two distinctable orientations, thus I have two fundamental solutions with different diffusion constants.

```

from numpy import arange, exp
from numpy import sum as sumn
from numpy.fft import fft, ifft, fftshift

def diffconv(x, f, Dt, w):
    """
    calculate the convolution of inital condition and fundamental solution
    -----
    x: range in real space
    f: initial function
    Dt: diffusion progress
    w: weight of the first domain
    """
    x = (x[1] - x[0]) * arange(- 1.0 * len(x) / 2, 1.0 * len(x) / 2)
    x = fftshift(x) # shift to correctly multiply with fundamental
    g1 = exp(- x ** 2 / (4 * 0.5 * Dt)) # fundamental solution for ac-direction
    g2 = exp(- x ** 2 / (4 * Dt)) # fundamental solution for a-direction
    g = w * g1 + (1 - w) * g2 # sum of weighted fundamental solutions
    g = g / sumn(g) # normalizing
    return (ifft(fft(f) * fft(g))).real # convolution via Fourier transform

```

B.3. Simplex minimization

A Nelder-Mead simplex algorithm is used to fit the calculated nuclear reflectivity to the experimental data. In comparison to other minimizations, e.g., Levenberg-Marquardt, it does not rely on differentials, which can be tricky for numerical evaluation if the surface in the solution space is very rough due to experimental date with bad statistics. This implementation allows for a boolean vector to specify, which parameters to fit, and additionally for intervals the parameters are restricted to.

```

from numpy import array, argsort, zeros, tile, mean, sqrt
from numpy import sum as sumn

```

```

from numpy import max as maxn
from numpy import min as minn
from numpy import all as alln

def set_lim(p, l):
    """reset simplex to allowed ranges"""
    a = p < l[:, 0]
    b = p > l[:, 1]
    p[a] = l[a, 0]
    p[b] = l[b, 1]
    return p

def init_simplex(p0, dp, fit):
    """initialize simplex for given ranges"""
    n = sum(fit)
    x = zeros((n, n + 1))
    x[:, 0] = p0[fit]
    for i in range(n):
        x[:, i + 1] = x[:, i] + dp[fit][i] \
            * array([1.0 if j == i else 0.0 for j in range(n)])
    c = mean(x, 1)
    x += tile(p0[fit] - c, (n + 1, 1)).T
    p = tile(p0, (n + 1, 1)).T
    p[fit, :] = x
    return p

def nelmead(fun, p0, dp, fit, lim, eps, *args):
    """
    nelder-mead algorithm to minimize function
    -----
    fun: function to minimize of the form fun(p0, a1, a2, a3, ...)
    p0: initial parameters
    dp: initial parameter spread
    fit: boolean vector which parameter is fitted
    lim: (:,2)-dim array for limits of parameters
    eps: upper limit for final parameter spread
    """
    n = sum(fit)

```

```

a = [1.0, 2.0, 0.5]
p = init_simplex(p0, dp, fit, n)
for i in range(len(p[0, :])):
    p[:, i] = set_lim(p[:, i], lim)
f = array([fun(p[:, i], *args) for i in range(n + 1)])
it = 0
while True:
    for i, l in enumerate(p[array(fit), :].T):
        print(' '.join(['{0:f}'.format(l[j]) for j in range(n)] \
            + ['-> {0:f}'.format(f[i])]))
    s = argsort(f) # sorting the simplex values from best to worst
    c = 1.0 / n * sumn(p[:, s[-1]], 1) # central point
    r = c + a[0] * (c - p[:, s[-1]]) # reflected point
    r = set_lim(r, lim)
    fr = fun(r, *args)
    if f[s[0]] <= fr < f[s[-2]]:
        p[:, s[-1]] = r # worst point reflected
        f[s[-1]] = fr
    elif fr < f[s[0]]:
        e = c + a[1] * (r - c) # extended reflected point
        e = set_lim(e, lim)
        fe = fun(e, *args)
        if fe < fr:
            p[:, s[-1]] = e # worst point extended reflected
            f[s[-1]] = fe
        else:
            p[:, s[-1]] = r # worst point reflected (w.o. extension)
            f[s[-1]] = fr
    else:
        if fr >= f[s[-1]]:
            k = c + a[2] * (p[:, s[-1]] - c) # contract worst point
        else:
            k = c + a[2] * (r - c) # contract reflected point
        k = set_lim(k, lim)
        fk = fun(k, *args)
        if fk < f[s[-1]]:
            p[:, s[-1]] = k # contract worst/reflected point
            f[s[-1]] = fk
        else:
            for i in range(n + 1):
                p[:, i] = a[2] * (p[:, i] + p[:, s[0]]) # contract simplex

```

```

        f[i] = fun(p[:, i], *args)
    it += 1
    av = summ(p, 1) / (n + 1)
    ss = summ(abs(maxn(p, 1) - minn(p, 1)) / abs(av)) / n
    if ss < eps: break
print('-> convergence after {0:d} iterations'.format(it))
return mean(p, 1)

```

B.4. Clebsch-Gordan coefficients

Numerical recipe to calculate arbitrary Clebsch-Gordan coefficients following the calculations in Rose [1957].

```

from numpy import array, matrix, arange, prod, sqrt
from math import factorial as fac

def cg(j, m):
    """
    clebsch-gordan coefficient for combination of two spin systems
    -----
    j: array of spin modulus of first, second and combined system
    m: array of projected spin of first, second and combined system
    """
    j = array(j)
    m = array(m)
    C = 0.0
    if abs(m[0] + m[1] - m[2]) > 0: return C
    if j[0] + j[1] < j[2] or j[2] < abs(j[0] - j[1]): return C
    for k in range(3):
        if abs(m[k]) > j[k]: return C
    A = matrix([[1, 1, -1], [1, -1, 1], [-1, 1, 1]])
    p = sqrt((2 * j[2] + 1) * prod(fac(A * matrix(j).T)) * prod(fac(j + m)) \
        * prod(fac(j - m)) / fac(sum(j) + 1))
    vmax = array([j[0] + j[1] - j[2], j[0] - m[0], j[1] + m[1]])
    vmin = array([j[1] - j[2] - m[0], j[0] - j[2] + m[1], 0])
    for v in arange(max(vmin), min(vmax) + 1):
        C += (-1) ** v / (prod(fac(vmax - v)) * prod(fac(v - vmin)))
    return p * C

```

B.5. Nuclear resonant reflectivity

In this section a minimal example for the calculation of the nuclear reflectivity in grazing incidence geometry is given. In the first file `main.py` the propagation matrices and subsequently the scattered intensities are calculated for every incident angle.

```

from numpy import array, matrix, hstack, zeros, eye, diag
from numpy import exp, pi, complex
from numpy.linalg import eig
from numpy import sum as sumn
from matplotlib.pyplot import semilogy, savefig
from multiprocessing import Process, Queue
from progressbar import ProgressBar
from eleceref import elec
from nucleref import nucl
from const import k0
from par import EE, Np, NA, ang, figname
from layer import lays, rho0

NE = len(EE)
keye = matrix(k0 * eye(2))
Cf0 = 2 * pi / k0
F = matrix(zeros((4,4)), dtype=complex)

def cref(a, E, nuc=False):
    eF = matrix(eye(4))           # starting matrix for iteration
    k = a * keye                 # diagonal matrix for k vector
    Cf = Cf0 / a                 # prefactor of scattering amplitude
    for ly in lays:              # iterate over layers
        Euv = elec(ly[0])        # electronic scattering amplitude
        if nuc:                  # if nuclear resonant scattering
            Nuv = nucl(E, a)     # nuclear scattering amplitude
            Muv = Euv + ly[2] * rho0 * Nuv    # total scattering amplitude
        else:
            Muv = Euv
    f = Cf * Muv
    # write propagation matrix
    F[:2, :2] = f + k
    F[:2, 2:] = f

```



```

    F[2:, :2] = - f
    F[2:, 2:] = - f - k
    # calculate eigenvalues and eigenstates
    EV, ES = eig(F)
    # propagate to next layer through matrix exponential
    eF = ES * diag(exp(1j * EV * ly[1])) * ES.I * eF
# reflected part of amplitude
return - eF[2:, 2:].I * eF[2:, :2]

def totref(a):
    refn = zeros(NE)
    for j, E in enumerate(EE):           # iterate over energies
        refe = cref(a, E)                # electronic reflectivity
        ref = cref(a, E, nuc=True)       # total reflectivity
        A = ref - refe                   # nuclear reflectivity
        refn[j] = abs(A[0, 0])**2 + abs(A[1, 0])**2 # intensity from scattering matrix
    return sumn(refn)                   # sum over energy spectrum

def reflectivity(q, ang):
    N = len(ang)
    ref = zeros(N)
    pbar = ProgressBar().start()       # create progress bar
    for i, a in enumerate(ang):         # iterate over scattering angles
        pbar.update(100.0 / N * i)      # update progress bar
        ref[i] = totref(a)              # calculate total reflectivity over all energies
    pbar.finish()
    q.put(ref)                          # return data in queue

def refmulproc(ang, Np):
    dN = len(ang) / Np                 # angle steps per proc
    q = []                              # queue list
    p = []                              # process list
    for i in range(Np):
        q.append(Queue())                # create queue
        # create process for part of the angle range
        p.append(Process(target=reflectivity, \
            args=(q[-1], ang[dN * i:dN * (i + 1)])))
    p[-1].start()                       # start process

```

```

    ref = [q[i].get() for i in range(Np)] # get return values from queues
    return hstack((r for r in ref))      # stack the reflectivity parts

if __name__ == '__main__':
    ref = refmulproc(ang, Np)           # calculate reflectivity
    semilogy(ang, ref, 'r-', lw=2)     # plot semilogarithmic
    savefig(filename)                  # save plot

```

The file `layer.py` defines the multilayer sample.

```

from numpy import array

rho0 = 4.0 / (3.87 ** 2 * 3.77) * 1E30 # m-3 # density of material
# layer parameters: refraction index [d, b], thickness (m), enrichment
lays = [
    [[1.09E-5, 1.38E-6], 1.40E-9, 0.40], # 1
    [[1.09E-5, 1.38E-6], 2.58E-9, 0.02],
    [[1.09E-5, 1.38E-6], 1.40E-9, 0.40], # 2
    [[1.09E-5, 1.38E-6], 2.58E-9, 0.02],
    [[1.09E-5, 1.38E-6], 1.40E-9, 0.40], # 3
    [[1.09E-5, 1.38E-6], 2.58E-9, 0.02],
    [[1.09E-5, 1.38E-6], 1.40E-9, 0.40], # 4
    [[1.09E-5, 1.38E-6], 2.58E-9, 0.02],
    [[1.09E-5, 1.38E-6], 1.40E-9, 0.40], # 5
    [[1.09E-5, 1.38E-6], 2.58E-9, 0.02],
    [[1.09E-5, 1.38E-6], 1.40E-9, 0.40], # 6
    [[1.09E-5, 1.38E-6], 2.58E-9, 0.02],
    [[1.09E-5, 1.38E-6], 1.40E-9, 0.40], # 7
    [[1.09E-5, 1.38E-6], 2.58E-9, 0.02],
    [[1.09E-5, 1.38E-6], 1.40E-9, 0.40], # 8
    [[1.09E-5, 1.38E-6], 2.58E-9, 0.02],
    [[1.09E-5, 1.38E-6], 1.40E-9, 0.40], # 9
    [[1.09E-5, 1.38E-6], 2.58E-9, 0.02],
    [[1.09E-5, 1.38E-6], 1.40E-9, 0.40], # 10
    [[1.09E-5, 1.38E-6], 2.58E-9, 0.02]]

```

The file `eleceref.py` contains the calculation of the electronic scattering amplitude in the constant energy approximation.

```

from numpy import eye, pi
from const import k0

```

```
# calculate the electronic scattering matrix
def elec(db):
    return k0 ** 2 / (2 * pi) * (-db[0] + 1j * db[1]) * eye(2)
```

The file `nuclref.py` contains the routines to calculate the nuclear resonant scattering amplitude in the grazing incidence approximation.

```
from numpy import array, matrix, arange, dot, cos, sin, pi
from numpy import sum as summ
from const import G0
from nucpar import Ig, Ie, L, Cnuc, Ege
from cg import cg as cgc

II = [Ig, L, Ie]
CG = array([[cgc(II, [m, M, m + M]) \
            for M in arange(-L, L + 1)] for m in arange(-Ig, Ig + 1)])
s = array([1.0, 0.0, 0.0]) # sigma polariz. vector
B = array([0.0, 0.0, 1.0]) # magnetic field direction
d_sB = dot(s, B)
C_n = 3.0 / (16 * pi)

# calculate energie dependent part of nuclear scattering matrix
def FLM(w, M):
    return Cnuc * G0 * summ([CG[m, M + L] ** 2 \
        / (2 * (Ege[m + Ig, M + Ie] - w) - 1j * G0) \
        for m in arange(2 * Ig + 1)])

# calculate the nuclear scattering matrix
def nucl(w, a):
    Fp = FLM(w, +1)
    Fm = FLM(w, -1)
    F0pm = 2 * FLM(w, 0) - Fp - Fm
    ca = cos(a)
    sa = sin(a)
    k = array([0.0, ca, sa]) # incoming wave vector
    p = array([0.0, sa, ca]) # pi polarization vector
    d_pB = dot(p, B)
    d_kB = dot(k, B)
```

```

return C_n * matrix([ \
    [Fp + Fm + d_pB ** 2 * F0pm, \
     -1j * d_kB * (Fp - Fm) - d_sB * d_pB * F0pm], \
    [1j * d_kB * (Fp - Fm) - d_sB * d_pB * F0pm, \
     Fp + Fm + d_sB ** 2 * F0pm]])

```

The file `nucpar.py` defines the parameters relevant for the calculation of the nuclear resonant part of the scattering amplitude.

```

from numpy import array, arange, pi
from const import lam, E0

Ig = 0.5           # spin ground state
Ie = 1.5           # spin excited state
L = 1.0           # spin transition
mu = 3.153E-8 # eV T-1 # magnetic moment
mug = 0.091 * mu  # rel. magn. moment ground state
mue = -0.153 * mu # rel. magn. moment excited state
B = 30.0 # T      # magnetic hyperfine field
fLM = 0.8         # Lamb Moessbauer factor
alpha = 0.8       # internal conversion factor
# prop. matrix pre-factor
Cnuc = 4 * pi * lam * fLM / (2 * Ig + 1) / (1 + alpha)
# calculate transition energies
Ege = array([[E0 - (mue * (g + m) / Ie - mug * g / Ig) * B \
             for m in arange(- L, L + 1)] for g in arange(- Ig, Ig + 1)])

```

The file `par.py` sets mainly the energy range of the resonance and the angular range of the refraction.

```

from numpy import linspace
from const import E0, G0

NE = 70           # number of natural linewidths from the center
N = 1000         # number of energy steps between range of above
# energy range around nuclear resonance
EE = linspace(E0 - NE * G0, E0 + NE * G0, N)
Np = 2           # number of processors
NA = 100         # number of angle steps
ang = linspace(2.0E-3, 1.5E-2, NA) # grazing angle range

```

```
figname = 'plot.pdf'           # name of plot file
```

The file `const.py` contains the fundamental physical constants involved.

```
from numpy import pi

hbar = 6.582E-16 # eV s      # planck constant
c = 3.00E8 # m s-1        # speed of light in vacuum
E0 = 1.44E4 # eV          # energy of photons
G0 = 4.66E-9 # eV         # natural linewidth of 57Fe
k0 = E0 / (hbar * c) # m-1  # wave vector in
lam = 2 * pi / k0 # m      # wave length of photons
```

ACKNOWLEDGEMENTS

First and foremost I would like to thank the supervisor of my thesis, B. Sepiol, for giving me the opportunity to deepen my insight in solid state physics and its methods, and further guiding me through a PhD thesis after already mentoring my diploma thesis. A good part of the physical basics and the experimental techniques I learned from him. The rest of my experimental experience can be attributed to E. Partyka-Jankowska, who also introduced me to the magic, that is preparing nanofilms.

Regarding the acknowledgements of M. Leitner's thesis I want to state that the debt is more than paid, and that I like train rides but my limit is at about twelve hours and four transfers. His deep understanding of mathematics and physics was a great help in the course of my study.

The preparation and the initial characterization of the samples for the diffusion study have been done by B. Laenens. I want to thank M. Rennhofer for establishing the experimental basis of the method in our group. The team for the diffusion measurement consisted of M. Rennhofer, B. Laenens, N. Planckaert, E. Partyka-Jankowska, R. Reitingier and myself. Of the beamline staff at the ESRF I would like to mention S. Stankov for the great support in the experiment.

For the phonon study the samples were prepared by S. Couet. The latter, N. Planckaert and myself did the measurement at the ESRF. The respective ab initio calculations have been realised by M. Sternik.

G. Vogl was the one who got me interested in the field of solid state physics with his unbroken enthusiasm. The collegial environment he created in the group with the almost mandatory group lunch and the general discussions flourishing around it made it a real pleasure to work at the university.

In the first year I had the privilege to inherit the final year of an assistant position at the university. The main part of my thesis, however, was funded by the Austrian Science Fund (FWF) contract P20767-N20 and P20713-N20.

Last but definitely not least I would like to thank my parents, who never doubted my choice to study what interested me let alone the outcome of it, and the many other persons accompanying me in these years.

BIBLIOGRAPHY

- M. A. Andreeva, N. G. Monina, and S. Stankov, Influence of dynamic effects in nuclear resonant Bragg scattering on the accuracy of determination of self-diffusion coefficient in $^{56}\text{Fe}/^{57}\text{Fe}$ periodic multilayers, *Moscow Univ. Phys. Bull.* **63**, 132 (2008).
- S. Arrhenius, Über die Reaktionsgeschwindigkeit bei der Inversion von Rohrzucker durch Säuren, *Zeitschrift für physikalische Chemie* **4**, 226 (1889).
- B. W. Batterman and H. Cole, Dynamical diffraction of x-rays by perfect crystals, *Rev. Mod. Phys.* **36**, 681 (1964).
- M. Blume and O. Kistner, Resonant absorption in the presence of Faraday rotation, *Phys. Rev.* **171**, 417 (1968).
- C. Brombacher, C. Schubert, M. Daniel, A. Liebig, G. Beddies, T. Schumann, W. Skopura, J. Donges, S. Häberlein, and M. Albrecht, Chemical ordering of FePt films using millisecond flash-lamp annealing, *J. Appl. Phys.* **111**, 023902 (2012).
- A. Chumakov, R. Rüffer, H. Grünsteudel, G. Grübel, J. Metge, O. Leupold, and H. Goodwin, Energy dependence of nuclear recoil measured with incoherent nuclear scattering of synchrotron radiation, *Europhys. Lett.* **30**, 427 (1995).
- A. Chumakov and W. Sturhahn, Experimental aspects of inelastic nuclear resonance scattering, *Hyperfine Interact.* **123/124**, 781 (1999).
- S. Couet, M. Sternik, B. Laenens, A. Siegel, K. Parlinski, N. Planckaert, F. Gröstlinger, A. Chumakov, R. Rüffer, B. Sepiol, K. Temst, and A. Vantomme, Anisotropic lattice dynamics of FePt L1₀ thin films, *Phys. Rev. B* **82**, 094109 (2010).

- J. Crank and P. Nicholson, A practical method for numerical evaluation of solutions of partial differential equations of the heat-conduction type, *Math. Proc. Cambridge* **43**, 50 (1947).
- A. Dannenberg, M. Gruner, A. Hucht, and P. Entel, Surface energies of stoichiometric FePt and CoPt alloys and their implications for nanoparticle morphologies, *Phys. Rev. B* **80**, 245438 (2009).
- C. Darwin, The theory of x-ray reflexion, *Phil. Mag.* **27**, 315 (1914a).
- C. Darwin, The theory of x-ray reflexion. Part II, *Phil. Mag.* **27**, 675 (1914b).
- J. DuMond and J. P. Youtz, An x-ray method of determining rates of diffusion in the solid state, *J. Appl. Phys.* **11**, 357 (1940).
- D. Dunne and C. Wayman, The effect of Austenite ordering on the Martensite transformation in Fe-Pt alloys near the composition Fe₃Pt: I. Morphology and transformation characteristics, *Metall. Mater. Trans. B* **4**, 137 (1973a).
- D. Dunne and C. Wayman, The effect of Austenite ordering on the Martensite transformation in Fe-Pt alloys near the composition Fe₃Pt: II. Crystallography and general features, *Metall. Mater. Trans. B* **4**, 147 (1973b).
- E. W. Elcock and C. W. McCombie, Vacancy diffusion in binary ordered alloys, *Phys. Rev.* **109**, 605 (1958).
- P. Ewald, Zur Begründung der Kristalloptik, *Ann. Physik* **354**, 1 (1916a).
- P. Ewald, Zur Begründung der Kristalloptik, *Ann. Physik* **354**, 117 (1916b).
- P. Ewald, Zur Begründung der Kristalloptik, *Ann. Physik* **359**, 519 (1917).
- H. Eyring, The activated complex in chemical reactions, *J. Chem. Phys.* **3**, 107 (1935).
- R. Farrow, D. Weller, R. Marks, M. Toney, A. Cebollada, and G. Harp, Control of the axis of chemical ordering and magnetic anisotropy in epitaxial FePt films, *J. Appl. Phys.* **79**, 5967 (1996).
- H. Fischer and H. Kaul, *Mathematik für Physiker: Gewöhnliche und partielle Differentialgleichungen, mathematische Grundlagen der Quantenmechanik*, volume 2 (Teubner Verlag, Wiesbaden, 2007), 3. edition.

- S. Ghosh, Calculation of phonon spectrum and elastic constants of FePd intermetallics: Performance of LDA and GGA, *Intermetallics* **17**, 708 (2009).
- J. Gróh and G. von Hevesy, Die Selbstdiffusion in festem Blei, *Ann. Physik* **65**, 216 (1921).
- F. Gröstlinger, M. Rennhofer, M. Leitner, E. Partyka-Jankowska, B. Sepiol, B. Laenens, N. Planckaert, and A. Vantomme, Anisotropic diffusion in FePt thin films, *Phys. Rev. B* **85**, 134302 (2012).
- A. Gupta, M. Gupta, S. Chakravarty, R. Ruffer, H.-C. Wille, and O. Leupold, Fe diffusion in amorphous and nanocrystalline alloys studied using nuclear resonance reflectivity, *Phys. Rev. B* **72**, 014207 (2005).
- M. Gupta, A. Gupta, J. Stahn, M. Horisberger, T. Gutberlet, and P. Allenspach, Iron self-diffusion in amorphous FeZr/⁵⁷FeZr multilayers measured by neutron reflectometry, *Phys. Rev. B* **70**, 184206 (2004).
- J. Hannon, N. Hung, G. Trammell, E. Gerdau, M. Mueller, R. Ruffer, and H. Winkler, Grazing-incidence antireflection films. I. Basic theory, *Phys. Rev. B* **32**, 5068 (1985a).
- J. Hannon and G. Trammell, Mössbauer diffraction. I. Quantum theory of gamma-ray and x-ray optics., *Phys. Rev.* **169**, 315 (1968).
- J. Hannon and G. Trammell, Mössbauer diffraction. II. Dynamical theory of Mössbauer optics, *Phys. Rev.* **186**, 306 (1969).
- J. Hannon, G. Trammell, M. Mueller, E. Gerdau, R. Ruffer, and H. Winkler, Grazing-incidence antireflection films. III. General theory for pure nuclear reflections, *Phys. Rev. B* **32**, 6363 (1985b).
- J. Honolka, T. Lee, K. Kuhnke, A. Enders, R. Skomski, S. Bornemann, S. Mankovsky, J. Minár, J. Staunton, H. Ebert, M. Hessler, K. Fauth, G. Schütz, A. Buchsbaum, M. Schmid, P. Varga, and K. Kern, Magnetism of FePt surface alloys, *Phys. Rev. Lett.* **102**, 067207 (2009).
- T. Ikeda, H. Kadowaki, and H. Nakajima, Diffusion of ⁴⁴Ti and ⁶³Ni in TiAl single crystal, *Acta Mater.* **49**, 3475 (2001).

- M. Kim, S. Shin, and K. Kang, Ordering of island-like FePt L1₀ thin films, *Appl. Phys. Lett.* **80**, 3802 (2002).
- V. Kohn and A. Chumakov, DOS: Evaluation of phonon density of states from nuclear resonant inelastic absorption, *Hyperfine Interact.* **125**, 205 (2000).
- R. Kozubski, M. Kozłowski, K. Zapala, V. Pierron-Bohnes, W. Pfeiler, M. Rennhofer, B. Sepiol, and G. Vogl, Atomic migration on ordering and diffusion in bulk and nanostructured FePt intermetallic, *J. Phase Equilib. Diffus.* **26**, 482 (2005).
- G. Kresse and J. Furthmüller, Efficiency of ab-initio total energy calculations for metals and semiconductors using a plane-wave basis set, *Comput. Mater. Sci.* **6**, 15 (1996).
- O. Kubaschewski, *Iron - Binary phase diagrams* (Springer-Verlag, Berlin, 1982).
- H. Kudielka and P. Runow, Einflüsse der Temperatur auf Symmetrie, Ordnungs- und Schwingungszustand des FePt-Gitters, *Z. Metallknd.* **67**, 699 (1976).
- A. Kushida, K. Tanaka, and H. Numakura, Chemical diffusion in L1₀-ordered FePt, *Mater. Trans.* **44**, 59 (2003).
- B. Laenens, F. M. Almeida, N. Planckaert, K. Temst, J. Meersschant, A. Vantomme, C. Rentenberger, M. Rennhofer, and B. Sepiol, Interplay between structural and magnetic properties of L1₀-FePt(001) thin films directly grown on MgO (001), *J. Appl. Phys.* **105**, 073913 (2009).
- B. Laenens, F. M. Almeida, A. Vantomme, and J. Meersschant, Determination of the direction of the *c*-axis of L1₀ FePt thin films with the Mössbauer spectroscopy, *Acta Phys. Pol. A* **112**, 1313 (2007).
- C.-G. Lee, R. Nakamura, T. Shimozaki, and T. Okino, Interdiffusion in Fe/Pt bulk diffusion couples, *Defect Diffus. Forum* **237–240**, 426 (2005).
- M. Leitner, B. Sepiol, L. Stadler, B. Pfau, and G. Vogl, Atomic diffusion studied with coherent x-rays, *Nat. Mater.* **8**, 717 (2009).
- T. Massalski, *Binary alloy phase diagrams* (American society for metals, 1986).
- J. Mayer, C. Elsässer, and M. Fähnle, Concentrations of atomic defects in B2–Fe_xAl_{1–x}, *Phys. Stat. Sol.* **191**, 283 (1995).

- J. Mayer and M. Fähnle, On the meaning of effective formation energies, entropies and volumes for atomic defects in ordered compounds, *Acta Mater.* **45**, 2207 (1997).
- T. Mehaddene, E. Kentzinger, B. Hennion, K. Tanaka, H. Numakura, A. Marty, V. Parasote, M. Cadeville, M. Zemirli, and V. Pierron-Bohnes, Lattice dynamics and migration enthalpies in CoPt₃ and FePd, *Phys. Rev. B* **69**, 024304 (2004).
- H. Mehrer, *Diffusion in solids: Fundamentals, methods, materials, diffusion-controlled processes*, Springer series in solid state science (Springer, Berlin, 2007).
- D. G. Merkel, S. Sajti, C. Fetzer, J. Major, R. Ruffer, A. Rhm, S. Stankov, F. Tanczikó, and L. Bottyán, Isotope-periodic multilayer method for short self-diffusion paths – a comparative neutron and synchrotron Mössbauer reflectometric study of FePd alloys, *J. Phys.: Conf. Ser.* **211**, 012029 (2010).
- B. Meyer and M. Fähnle, Atomic defects in ordered compound B2-NiAl: A combination of ab initio electron theory and statistical mechanics, *Phys. Rev. B* **59**, 6072 (1999).
- Y. Mishin, I. V. Belova, and G. E. Murch, Atomistic modeling of diffusion in the TiAl compound, *Defect Diffus. Forum* **237–240**, 271 (2005).
- H. Nakajima, Y. Nose, N. Terashita, T. Ikeda, and H. Numakura, Diffusion in L1₀-type single crystal TiAl and FePt intermetallic compounds, *Defect Diffus. Forum* **237–240**, 7 (2005).
- J. Nelder and R. Mead, A simplex method for function minimization, *Comput. J.* **7**, 308 (1965).
- Y. Nose, T. Ikeda, H. Nakajima, and H. Numakura, Tracer diffusion of Fe and Pd in FePt and FePt₃, *Defect Diffus. Forum* **237–240**, 450 (2005).
- Y. Nose, N. Terashita, T. Ikeda, and H. Nakajima, Impurity diffusion in γ -TiAl single crystals, *Acta Mater.* **54**, 2511 (2006).
- J. Nye, *Physical properties of crystals* (Oxford University Press, London, 1957).
- K. Parlinski, Z. Li, and Y. Kawazoe, First-principles determination of the soft mode in cubic ZrO₂, *Phys. Rev. Lett.* **78**, 4063 (1997).

- H. Pelzer and E. Wigner, Über die Geschwindigkeitskonstante von Austauschreaktionen, *Z. Phys. Chem., B* **15**, 445 (1932).
- J. Philibert, *Atom movements: Diffusion and mass transport in solids*, Monographies de physique (Ed. de Physique, Les Ulis Cedex, 1991).
- V. Pierron-Bohnes, R. Montsouka, C. Goyhenex, T. Mehaddene, L. Messad, H. Bouzar, H. Numakura, K. Tanaka, and B. Hennion, Atomic migration in bulk and thin film L1₀ alloys: Experiments and molecular dynamics simulations, *Defect Diffus. Forum* **263**, 41 (2007).
- U. Pietsch, V. Holý, and T. Baumbach, *High-resolution x-ray scattering*, Springer series in solid state science (Springer, New York, 2004), 2. edition.
- W. Press, S. Teukolsky, W. Vetterling, and B. Flannery, *Numerical recipes in C* (Cambridge University Press, New York, 1992), 2. edition.
- D. G. Rancourt and J. Y. Ping, Voigt-based methods for arbitrary-shape static hyperfine parameter distributions in Mössbauer spectroscopy, *Nucl. Instr. Meth.* **B58**, 85 (1991).
- M. Rennhofer, B. Sepiol, M. Sladeczek, D. Kmiec, S. Stankov, G. Vogl, M. Kozłowski, R. Kozubski, A. Vantomme, J. Meerssaut, R. Rüffer, and A. Gupta, Self-diffusion of iron in L1₀-ordered FePt thin films, *Phys. Rev. B* **74**, 104301 (2006).
- R. Röhlberger, Theory of x-ray grazing incidence reflection in the presence of nuclear resonance excitation, *Hyperfine Interact.* **123/124**, 301 (1999).
- R. Röhlberger, *Nuclear condensed matter physics with synchrotron radiation: Basic principles, methodology and applications*, Springer tracts in modern physics (Springer, Berlin Heidelberg, 2004).
- M. Rose, *Elementary theory of angular momentum* (John Wiley & Sons, Inc., New York, 1957).
- R. Rüffer and A. Chumakov, ESRF – Nuclear resonance beamline – Beamline layout and performance, http://www.esrf.eu/UsersAndScience/Experiments/DynExtrCond/ID18/beamline_layout (2012), accessed: 18/01/2012.

- R. Ruffer and A. I. Chumakov, Nuclear resonance beamline at ESRF, *Hyperfine Interact.* **97/98**, 589 (1996).
- G. Sauerbrey, Verwendung von Schwingquarzen zur Wägung dünner Schichten und zur Mikrowägung, *Zeitschrift für Physik* **155**, 206 (1959).
- T. Seki, T. Shima, K. Takanashi, Y. Takahashi, E. Matsubara, Y. K. Takahashi, and K. Hono, Influence of the buffer layers on magnetic properties of FePt (001) films sputter-deposited at reduced temperature, *J. Appl. Phys.* **96**, 1127 (2004).
- M. Seto, Y. Yoda, S. Kikuta, X. Zhang, and M. Ando, Observation of nuclear resonant scattering accompanied by phonon excitation using synchrotron radiation, *Phys. Rev. Lett.* **74**, 3828 (1995).
- T. Shinjo and W. Keune, Mössbauer-effect studies of multilayers and interfaces, *J. Magn. Magn. Mater.* **200**, 598 (1999).
- K. Singwi and A. Sjölander, Resonance absorption of nuclear gamma-rays and the dynamics of atomic motions, *Phys. Rev.* **120**, 1093 (1960).
- J. B. Staunton, S. Ostanin, S. S. A. Razee, B. Gyorffy, L. Szunyogh, B. Ginatempo, and E. Bruno, Long-range chemical order effects upon the magnetic anisotropy of FePt alloys from an ab initio electronic structure theory, *J. Phys.: Condens. Matter* **16**, 5623 (2004).
- B. Stipe, T. Strand, C. Poon, H. Balamane, T. Boone, J. Katine, J.-L. Li, V. Rawat, H. Nemoto, A. Hirotsumi, O. Hellwig, R. Ruiz, E. Dobisz, D. Kercher, N. Robertson, T. Albrecht, and B. Terris, Magnetic recording at 1.5 Pbit m^{-2} using an integrated plasmonic antenna, *Nat. Photon.* **4**, 484 (2010).
- W. Sturhahn and E. Gerdau, Evaluation of time-differential measurements of nuclear-resonance scattering of x-rays, *Phys. Rev. B* **49**, 9285 (1994).
- W. Sturhahn and V. Kohn, Theoretical aspects of incoherent nuclear resonant scattering, *Hyperfine Interact.* **123/124**, 367 (1999).
- W. Sturhahn, T. Toellner, E. Alp, X. Zhang, M. Ando, Y. Yoda, S. Kikuta, M. Seto, C. Kimball, and B. Dabrowski, Phonon density of states measured by inelastic nuclear resonant scattering, *Phys. Rev. Lett.* **74**, 3832 (1995).

- D. Suess, S. Eder, J. Lee, R. Dittrich, J. Fidler, J. Harrell, T. Schrefl, G. Hrkac, M. Schabes, N. Supper, and A. Berger, Reliability of Sharrocks equation for exchange spring bilayers, *Phys. Rev. B* **75**, 174430 (2007).
- Y. Sui, Z. Chen, X. Shu, and T. Wang, Point defects in L1₀ phase FePt alloy: A first principle study, *Mater. Sci. F.* **561–565**, 1923 (2007).
- K. Sumiyama, M. Shinga, M. Morioka, and Y. Nakamura, Characteristic magnetovolume effects in Invar type Fe-Pt alloys, *J. Phys. F: Metal Phys.* **9**, 1665 (1979).
- S. Sun, C. B. Murray, D. Weller, L. Folks, and A. Moser, Monodisperse FePt nanoparticles and ferromagnetic FePt nanocrystal superlattices, *Science* **287**, 1989 (2000).
- Y. K. Takahashi, K. Hono, T. Shima, and K. Takanashi, Microstructure and magnetic properties of FePt thin films epitaxially grown on MgO (001) substrates, *J. Magn. Magn. Mater.* **267**, 248 (2003).
- Y. Tamada, R. Masuda, A. Togo, S. Yamamoto, Y. Yoda, I. Tanaka, M. Seto, S. Nasu, and T. Ono, Anisotropic phonon density of states in FePt nanoparticles with L1₀ structure, *Phys. Rev. B* **81**, 132302 (2010).
- B. D. Terris and T. Thomson, Nanofabricated and self-assembled magnetic structures as data storage media, *J. Phys. D: Appl. Phys.* **38**, R199 (2005).
- M. Trautz, Evaluation of Arrhenius frequency factor (A) by simple collision theory, *Chemistry* **96** (1916).
- L. Van Hove, Correlations in space and time and Born approximation scattering in systems of interacting particles, *Phys. Rev.* **95**, 249 (1954).
- M. von Laue, *Röntgenstrahlinterferenzen* (Akad. Verl.-Ges., Frankfurt am Main, 1960), 3. edition.
- H. Wegener, *Der Mößbauer Effekt und seine Anwendungen in Physik und Chemie*, BI-Hochschultaschenbücher (Bibliograph. Inst., Mannheim, 1965).
- D. Weller, A. Moser, L. Folks, M. E. Best, W. Lee, M. F. Toney, M. Schwickert, J. U. Thiele, and M. F. Doerner, High K_u materials approach to 100 Gbits/in², *IEEE Trans. Magn.* **36**, 10 (2000).

M. L. Yan, Y. F. Xu, and D. J. Sellmyer, Nanostructure and magnetic properties of highly (001) oriented L1₀ (Fe₄₉Pt₅₁)_{1-x}Cu_x films, *J. Appl. Phys.* **99**, 08G903 (2006).

curriculum vitae

Personal information

name Friedrich Gröstlinger
date of birth 1982/05/10
place of birth Ried im Innkreis
nationality Austria

Education

2009–2012 **doctoral studies of physics**, University of Vienna, Vienna.
2008/11 **Master in natural sciences**, *CEMS investigation of the phase transition of metastable FeSi thin films*, University of Vienna, Vienna.
2002–2008 **studies of physics**, University of Vienna, Vienna.
2001–2002 **military service**, *technical pioneer*, PiB 2, Salzburg.
1996–2001 **mechanical engineering and engineering economics**, HTBLA Vöcklabruck, Vöcklabruck.

Language skills

german **mother tongue**
english **fluent**

Software skills

operating system	Linux, Microsoft Windows	office	LaTeX, Open Office, Microsoft Office
programming	Python, Fortran90, C, Bash	visualization	Matplotlib, Gnuplot
mathematic	Numpy, Sympy, Matlab, Mathematica	graphic	Gimp, Inkscape, Infranview

Special skills

technical set up of a ultra-high vacuum system to prepare and characterize nanolayers
experimental 6 weeklong stays at the European synchrotron radiation facility ESRF, Grenoble, France

Teaching

2009W–2011S practical course in solid state physics: advanced materials
2010W exercise course to solid state physics I

Presentations

- 2011/09 **talk**, *Diffusion in FePt thin films*, International conference on the applications of the Mössbauer effect ICAME, Kobe, Japan.
- 2011/07 **talk**, *Diffusion in FePt isotopic multilayers*, 8th international conference on diffusion in materials DIMAT, Dijon, France.
- 2010/09 **poster**, *Diffusion in FePt isotopic multilayers*, 60. Jahrestagung der österreichischen physikalischen Gesellschaft, Salzburg, Austria.
- 2010/01 **talk**, *Diffusion*, Physics open 2010, Vienna, Austria.

Publications

- F. Gröstlinger, M. Rennhofer, M. Leitner, E. Partyka-Jankowska, B. Sepiol, B. Laenens, N. Planckaert, and A. Vantomme, Anisotropic diffusion in FePt thin films, *Phys. Rev. B* **85**, 134302 (2012).
- S. Couet, M. Sternik, B. Laenens, A. Siegel, K. Parlinski, N. Planckaert, F. Gröstlinger, A. Chumakov, R. Ruffer, B. Sepiol, K. Temst, and A. Vantomme, Anisotropic lattice dynamics of FePt L1₀ thin films, *Phys. Rev. B* **82**, 094109 (2010).